RADIATION-HARD SILICON PHOTONICS FOR FUTURE HIGH ENERGY PHYSICS EXPERIMENTS

Marcel Zeiler

B.Sc., M.Sc.

Thesis submitted in fulfillment of the requirements for the
award of Doctor of Philosophy (Ph.D.)
to the

Dublin City University
Faculty of Engineering and Computing
School of Electronic Engineering

Internal Supervisor: Prof. Liam Barry
External Supervisor: Dr. Jan Troska (CERN)

June 2017

Declaration

I hereby certify that this material, which I now submit for assessment on the programme of study leading to the award of Doctor of Philosophy is entirely my own work, and that I have exercised reasonable care to ensure that the work is original, and does not to the best of my knowledge breach any law of copyright, and has not been taken from the work of others save and to the extent that such work has been cited and acknowledged within the text of my work.

Signed:

ID No.:

Date:

The research for this work was partially conducted within the Intel-CERN-European Doctorate-Industrial-Program (ICE-DIP).
ICE-DIP is a European Industrial Doctorate project funded by the European Commission's 7th Framework programme Marie Curie Actions under grant PITN-GA-2012-316596.

Contents

List of Figures

List of Tables

List of Abbreviations

ALICE A Large Ion Collider Experiment

ATLAS A Toroidal LHC ApparatuS

BER Bit-Error-Rate

BOX Buried Oxide

CERN European Organization for Nuclear Research

CMOS Complementary Metal-Oxide-Semiconductor

CMS Compact Muon Solenoid

COTS Commercial Off-The-Shelf

CW Continuous-Wave

DFB Distributed Feedback

EAM Electro Absorption Modulator

ehps Electron-hole pairs

FSR Free Spectral Range

Ge Germanium

GeSi Germanium-on-Silicon

HEP High Energy Physics

IC Integrated Circuit

IV Current-voltage

Kerma Kinetic Energy Released in Matter

LHC Large Hadron Collider

LHCb Large Hadron Collider beauty (experiment)

MMI Multi-Mode Interference (coupler)

MPW Multi-Project Wafer

MZI Mach-Zehnder Interferometer

MZM Mach-Zehnder Modulator

NIEL Non-Ionizing Energy Loss

OMA Optical Modulation Amplitude

OSA Optical Spectrum Analyzer

PCB Printed Circuit Board

PD Photodiode

PDE Plasma Dispersion Effect

PKA Primary Knock-on Atom

PRBS Pseudorandom Binary Sequence

RF Radio-Frequency

Rx Receiver

SEE Single Event Effect

Si Silicon

SiO_2 Silicon dioxide (oxide)

SiPh Silicon Photonics

SLED Superluminescent Light Emitting Diode

SOI Silicon-On-Insulator

SRH Shockley-Read-Hall

SRIM Stopping and Range of Ions in Matter

TE Transversal electric

TID	Total Ionizing Dose
TM	Transversal magnetic
TRx	Transceiver
Tx	Transmitter
VCSEL	Vertical-Cavity-Surface-Emitting-Laser
VL	Versatile Link
VL+	Versatile Link Plus
WDM	Wavelength Division Multiplexing

Abstract

Marcel Zeiler, Radiation-hard Silicon Photonics for Future High Energy Physics Experiments

Collisions of proton beams in the Large Hadron Collider at CERN produce very high radiation levels in the innermost parts of the particle detectors and enormous amounts of measurement data. Thousands of radiation-hard optical links based on directly-modulated laser diodes are thus installed in the particle detectors to transmit the measurement data to the processing electronics. The radiation levels in the innermost regions of future particle detectors will be much higher than they are now. Alternative solutions to laser-based radiation-hard optical links have to be found since the performance of laser diodes decreases beyond the operation margin of the system when irradiated to sufficiently high radiation levels. Silicon Photonics (SiPh) is currently being investigated as a promising alternative technology. First tests have indeed shown that SiPh Mach-Zehnder modulators (MZMs) are relatively insensitive to a high neutron fluence. However, they showed a strong degradation when exposed to ionizing radiation. A SiPh test chip that includes MZMs with varied design parameters was designed and fabricated at imec to identify parameters that improve the resistance of MZMs to ionizing radiation. The performance of the various MZMs was tested before, during and after irradiation with x-rays. An MZM design that can withstand ionizing radiation levels 5× higher than the initially tested devices was identified. Eye diagrams of these MZMs showed no significant difference after irradiation compared to reference samples. A model for the Optical Modulation Amplitude (OMA) of MZMs was developed to determine the radiation levels up to which SiPh-based optical links would work reliably. The analysis showed that a sufficiently large OMA could be sustained up to higher radiation levels than the upcoming Versatile Link system was designed. At the same time, the electrical power consumption of the proposed system was estimated to be similar.

Introduction

Motivation

Why does matter dominate over antimatter? What are the fundamental particles that make up the universe as we observe it today? Researchers have been trying to answer such fundamental questions about our universe and its constituent matter ever since ancient Greek times. Some of these questions could be answered by recreating conditions similar to those in the moments after the Big Bang. For this reason, the European Organization for Nuclear Research (CERN) operates the Large Hadron Collider (LHC) particle accelerator and hosts several High Energy Physics (HEP) experiments. The LHC is the world's largest and most sophisticated technical installation. It was built to accelerate charged particles to a speed close to the speed of light and make them collide. These collisions take place in the center of HEP experiments that consist of a large particle detector, with millions of individual sensors to detect the collisions, and the required electronics to process the measurement data. The recorded data from the sensors allows the researchers to reconstruct the collisions and helps them in making a step towards answering the questions above.

Detecting the particle collisions with millions of sensors generates an enormous amount of raw measurement data. For instance, each HEP experiment created about 40 Tb/s of raw measurement data during LHC's Run 1 between 2009 and 2013 [1]. To put this number into perspective, it is more than 5700× the amount of incoming data Facebook had in 2014 [2]. The only economic and energy-efficient way of handling such large amounts of data is to have tens of thousands of fiber optic links installed in the HEP experiments. These links are the backbone of the experiments' read-out system and provide the bandwidth necessary to send the measurement data from the particle sensors to the backend electronics for further processing.

The optical transceivers (TRx) at the end of the link that is installed in the HEP experiments are exposed to a very harsh environment. Superconducting magnets used to bend the accelerated charged particles along their intended trajectory create magnetic fields up to several Tesla. This is about one hundred thousand times stronger than the magnetic field of the earth. Since these superconducting magnets have to be cooled down to the temperature of liquid Helium, there is a large temperature gradient ranging from $-269\,^{\circ}\mathrm{C}$ at the center of the experiments to room temperature at its outer perimeter. In addition, the decay products of the particle collisions create extreme radiation levels near the particle collision points. This radiation has typically the strongest impact on device reliability and causes Commercial Off-The-Shelf (COTS) optical TRx, that have not been made for such extreme environments, to stop working quickly. Consequently, only specially designed or qualified parts that are able to withstand these harsh conditions can be used inside HEP experiments.

The current- and next generation of optical TRx that will be deployed in the experiments are based on directly modulated Vertical-Cavity-Surface-Emitting-Lasers (VCSELs). These will be used to read-out the particle sensors in most regions of the experiments throughout 2025 and beyond. It is foreseeable, however, that the radiation levels close to the particle collision point in future experiments will be too high for VCSELs to withstand. A new technology for optical TRx that can resist the predicted radiation levels and transmit the measurement data reliably from the inside of such future particle detectors to the processing electronics will therefore be required.

This thesis will investigate the suitability and feasibility of applying Silicon Photonics transmitters as an alternative to VCSEL-based TRx in HEP experiments. Silicon Photonics (SiPh) technology has been chosen because it holds great promise for commercial applications in data communications and because Silicon (Si) is a very good material for particle sensors that need to resist very high radiation levels. Initial tests of SiPh Mach-Zehnder Modulators (MZMs) have shown that these devices can be irradiated with a neutron fluence (neutrons per cm^2 impinging on device) high enough for future HEP experiments without showing significant degradation. Unfortunately, the same devices degraded and stopped working when exposed to ionizing radiation at levels below those expected in future HEP experiments.

The focus of this research is to determine whether the design of SiPh MZMs can be modified so that the devices can withstand higher levels of ionizing radiation. A radiation-hardness against a Total Ionizing Dose (TID) of at least $1\,\mathrm{MGy}$ (absorbed radiation energy per mass, $1\,\mathrm{Gy} = 1\,\mathrm{J/kg}$) should be reached to allow the installation of SiPh TRx in the innermost parts of future HEP experiments (≈ 10 cm from beam pipe) that could otherwise not be equipped with radiation-hard optical links.

In order to build upon the available SiPh technology and keep overall costs down, modifications to the MZM design should be implemented in a way that the device will still be compatible with a standard SiPh process. At the same time, the modulation-performance of MZMs with increased radiation-hardness has to be high enough that an actual system based on CERN's requirements can be built.

Aside from HEP, the outcomes of this research could also be of interest to other applications where data has to be sent from or to regions with extreme radiation levels. For instance, radiation-hard SiPh could be used to read out sensor data from the inside of fusion or fission reactors or in nuclear medicine. Furthermore, applications in aerospace could also benefit from radiation-tolerant SiPh, e. g. when data needs to be sent within satellites or rovers.

Contributions

The main contributions of this work are the following:

Simulation and design of the first SiPh chip dedicated for radiation-hardness evaluations for applications at CERN.

A SiPh test chip accommodating several custom- and pre-designed MZMs as well as various other test structures was designed. The MZMs have different design parameters that allow the identification of the parameters that affect the radiation-hardness of these devices. The performance of the custom-designed MZMs was simulated before the devices were implemented into a mask layout. The test chip was fabricated in a Multi-Project Wafer run and was measured to be fully functional before radiation exposure.

X-ray irradiation tests with SiPh chips under different conditions.

Several chips were irradiated with x-rays. Tests were conducted with un-biased and reverse-biased samples during irradiation at room temperature and with un-biased samples at −30 °C. The phase shifts of the individual MZMs were determined as a function of x-ray dose to assess when it dropped below a critical value. An MZM design that is able to withstand the minimum defined TID requirement of 1 MGy was identified.

Development of a system-level model for radiation-hard SiPh optical links.

The dynamic performance of irradiated MZMs that withstood high TID levels was compared to un-irradiated samples. It was shown that irradiated MZMs with the highest radiation-hardness show no significant degradation in measured eye diagrams. An analytical model for the Optical Modulation Amplitude (OMA) as a function of TID was developed. Based on the specifications as defined for the Versatile Link system that will be installed in 2018, the model showed that a SiPh-based optical link could be operated up to 1.7 MGy. The optical power budget and electrical power consumption of such a link were compared to the specifications of the Versatile Link system. The results indicate that SiPh-based optical links can be more radiation-hard than TRx for the Versatile Link while having a similar power consumption.

Publications

Parts of these contributions have been published.

Journals

M. Zeiler, S. Detraz, L. Olantera, G. Pezzullo, S. Seif El Nasr-Storey, C. Sigaud, C. Soos, J. Troska, and F. Vasey, “Design of Si-Photonic structures to evaluate their radiation hardness dependence on design parameters”, in *Journal of Instrumentation*, vol. 11, 2016.

M. Zeiler, S. Detraz, L. Olantera, C. Sigaud, C. Soos, J. Troska, and F. Vasey, “A system-level model for high-speed, radiation-hard optical links in HEP experiments based on silicon Mach-Zehnder modulators”, in *Journal of Instrumentation*, vol. 11, 2016.

M. Zeiler, S. Seif El Nasr-Storey, S. Detraz, A. Kraxner, L. Olantera, C. Scarcella, C. Sigaud, C. Soos, J. Troska and F. Vasey, “Radiation Damage in Silicon Photonic Mach-Zehnder Modulators and Photodiodes”, in *IEEE Transactions on Nuclear Science (submitted for publication)*, May 2017.

Conferences Presentation

M. Zeiler, S. Detraz, L. Olantera, S. Seif El Nasr-Storey, C. Sigaud, C. Soos, J. Troska, and F. Vasey, “Radiation hardness evaluation and phase shift enhancement through ionizing radiation in silicon Mach-Zehnder modulators”, in *Radiation Effects on Components and Systems (RADECS)*, 2016.

M. Zeiler, S. Detraz, L. Olantera, C. Sigaud, C. Soos, J. Troska, and F. Vasey, “Comparison of the Radiation Hardness of Silicon Mach-Zehnder Modulators for Different DC Bias Voltages”, in *IEEE Nuclear Science Symposium/Medical Imaging Conference (NSS/MIC)*, 2016.

Contributions to further publications related to this thesis

S. Seif El Nasr-Storey, F. Boeuf, C. Baudot, S. Detraz, J. M. Fedeli, D. Marris-Morini, L. Olantera, G. Pezzullo, C. Sigaud, C. Soos, J. Troska, F. Vasey, L. Vivien, M. Zeiler, and M. Ziebell, “Silicon Photonics for High Energy Physics Data Transmission Applications”, in *IEEE 11th International Conference on Group IV Photonics (GFP)*, 2014, pp. 1 - 2.

S. Seif El Nasr-Storey, S. Detraz, L. Olantera, G. Pezzullo, C. Sigaud, C. Soos, J. Troska, F. Vasey, and M. Zeiler, “Neutron and X-ray Irradiation of Silicon Based Mach-Zehnder Modulators”, *Journal of Instrumentation*, vol. 10, 2015.

S. Seif El Nasr-Storey, F. Boeuf, C. Baudot, S. Detraz, J. M. Fedeli, D. Marris-Morini, L. Olantera, G. Pezzullo, C. Sigaud, C. Soos, J. Troska, F. Vasey, L. Vivien, M. Zeiler, and M. Ziebell, “Effect of radiation on a Mach-Zehnder interferometer silicon modulator for HL-LHC data transmission applications”, *IEEE Transactions on Nuclear Science*, vol. 62, no. 6, pp. 2971 - 2978, 2015.

S. Seif El Nasr-Storey, F. Boeuf, C. Baudot, S. Detraz, J. M. Fedeli, D. Marris-Morini, L. Olantera, G. Pezzullo, C. Sigaud, C. Soos, J. Troska, F. Vasey, L. Vivien, M. Zeiler, and M. Ziebell, “Modeling TID Effects in Mach-Zehnder Interferometer Silicon Modulator for HL-LHC data Transmission Applications”, *IEEE Transactions on Nuclear Science*, vol. 62, no. 6, pp. 2971 - 2978, 2015.

Thesis Structure

This thesis is divided into seven chapters with the following emphases.

Chapter 1 introduces the LHC and HEP experiments at CERN. The basics of particle detectors with the various sub-detectors and the architecture of the optical links are explained. The planned upgrades for the LHC, the resulting increase in radiation levels and what this entails for the optical TRx are highlighted. The reason why SiPh was chosen for investigation and the benefits this technology might bring to radiation-hard optical links for HEP applications are presented.

The basics of SiPh are outlined in Chapter 2. The focus lies on MZMs and their underlying building blocks, optical waveguides and phase shifters. The latest developments for lasers and photodiodes in SiPh are briefly addressed as these components will also be needed for a full optical TRx.

Chapter 3 focuses on the fundamentals of radiation-matter interactions, particularly for silicon-based devices. Displacement damage induced through non-ionizing energy loss of high energy particles and TID damage created by ionizing radiation are explained. The changes to the material properties stemming from such damage are discussed.

The simulation and design work for the SiPh chip is described in Chapter 4. The simulation procedure and the results are presented and the implementation of the findings into a mask layout is included. A comparison of simulated and measured pre-irradiation phase shits of the MZMs on the fabricated chip is given.

The outcomes from the various irradiation tests are examined in Chapter 5. The different setups and conditions used for the tests are described. The results of the phase shift measurements of the MZMs with different design parameters as a function of TID are presented. Results from simulations performed to understand the radiation-induced device degradation are shown.

The system-level model for radiation-hard optical links based on SiPh MZMs is developed in Chapter 6. Eye diagram measurements of irradiated MZMs are demonstrated and measured OMAs are compared to calculations made with the model. The power consumption and optical power budget of this system proposal are compared with those for the optical links that will be installed in the HEP experiments after 2018.

A conclusion of the work is drawn and an outlook on possible future work to emerge from this research is set out in Chapter 7.

1 High energy physics experiments and optical links at CERN

The LHC was constructed to accelerate charged particles, particularly protons and lead ions, and make them collide. Analyzing these collisions allows researchers to test the Standard Model of particle physics and the theories beyond it. The collisions are detected in one of the four major HEP experiments at CERN: ALICE (A Large Ion Collider Experiment), ATLAS (A Toroidal LHC ApparatuS), CMS (Compact Muon Solenoid) and LHCb (Large Hadron Collider beauty). This chapter outlines the basic configurations of the HEP experiments at the LHC and describes the optical links installed between the particle detectors and the processing electronics. The challenge of radiation exposure of those links for imminent and future systems is described based on the CMS experiment.

1.1 The Large Hadron Collider

The LHC is the world's biggest circular particle accelerator with a diameter of 26.659 km. A schematic of the LHC tunnel complex, the four major HEP experiments and their location underneath the Franco-Swiss border is depicted in Fig. 1.1. The LHC was constructed to produce particle collisions at the highest energy levels to date. The energy density and temperature emerging from these collisions are similar to those immediately after the Big Bang.

In order to reach such high energy levels, the particles in the LHC need to have a speed close to the speed of light. This can be achieved by using Radio-Frequency (RF) cavities to accelerate two proton beams to an energy of 7 TeV each. This corresponds to a particle speed of 99.9999991 % the speed of light. The two beams circulate in the form of bunches of around 10^{10} particles clockwise and counterclockwise in two adjacent beam pipes in the LHC tunnel. They are focused into the beam pipe and guided along their trajectory by strong magnetic fields. The beam pipes

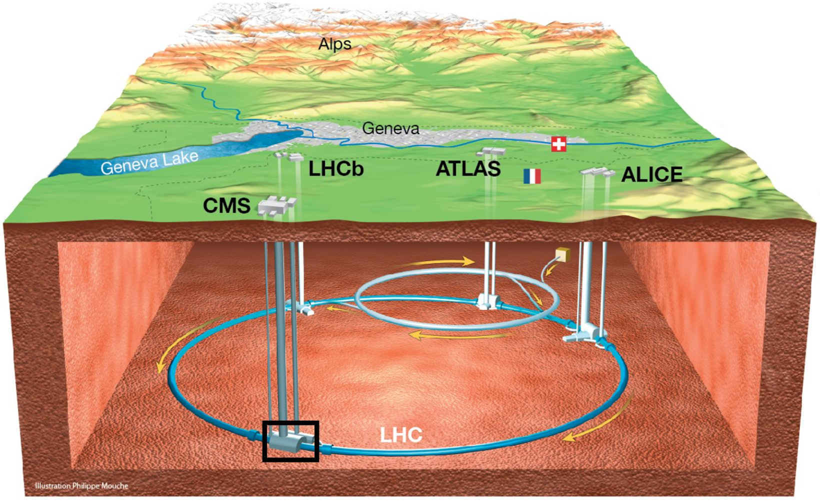

Figure 1.1: Schematic of the LHC tunnel complex and the major experiments located on the accelerator ring, from [3]. Details of the CMS experiment (black rectangle) are shown in Fig. 1.2 and 1.3.

cross and the trajectories of the beams overlap at four distinct particle collision points where the bunches collide every 25 ns.

The particle collision points are centered in four building-size particle detectors located on the LHC ring. They were designed to record the collisions of the particle bunches with millions of individual sensors arranged around the particle collision center to detect the collision products. Each sensor can be regarded as a camera taking a picture of the particle collisions. An entire collision event can later be reconstructed by combining all the pictures taken at the same time. A sophisticated installation of various sub-detectors has been developed for this purpose. Fig. 1.2 shows a cross-section of the CMS experiment with the main sub-detectors. These sub-detectors are: the silicon tracking sensors, the electromagnetic and hadronic calorimeters and the muon chambers. The silicon tracking sensors are employed to determine the position and momenta of traversing charged particles. They extend radially up to 1 m from the particle collision point. Electromagnetic and hadron calorimeters are installed to measure the energy of e. g. electrons/photons and neutrons/protons, respectively. These detectors range from $1 - 2$ m from the center of the installation. At the outermost part, $4 - 7$ m from the particle collision point, chambers are located to identify muons and measure their momenta. The exact particle collisions can be reconstructed by analyzing the data from all of the approximately 75 million sensors located in the CMS detector.

Each bunch crossing produces a number of collisions dependent on the beam settings.

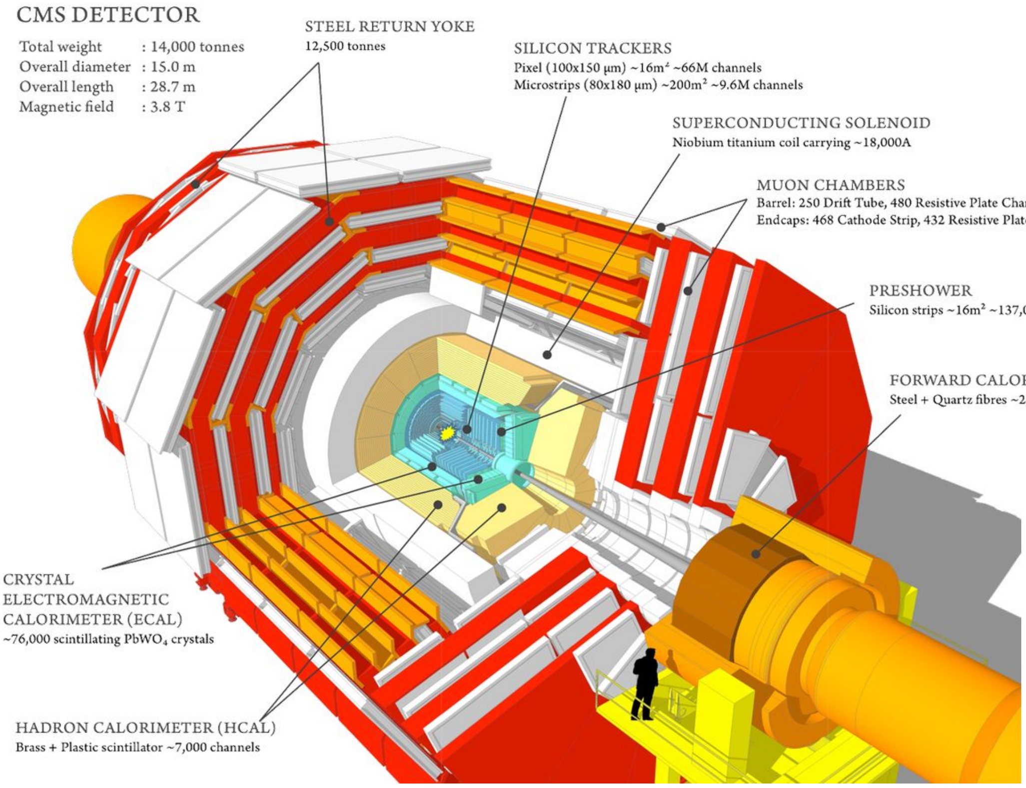

Figure 1.2: Schematic of the CMS experiment and its sub-detectors, from [4]. The particle collision point (marked in yellow) is in the very center of the installation.

The entirety of collisions per bunch crossing are called an "event". Since the data of each event has a size of about 1 MB and the particle bunches cross the particle collision points at a rate of 40 MHz, the amount of raw measurement data created per experiment is in the order of 40 Tb/s [5]. This is too much data to be processed and stored in real-time. Data filtering is therefore done to select the data that is to be processed further and eventually stored and that which is to be discarded. The filter decisions are made based on measured energy and momentum values of a given dataset. Only if both values are above values specific to the current measurement purpose, the data of these events is kept. Data not meeting the filter conditions are discarded.

1.2 Optical links for the LHC

The filtering process itself is performed by the back-end electronics located in the counting room outside the experimental cavern (Fig. 1.3). In this arrangement, the particle detector and front-end control electronics are located in the experimental cavern, while the back-end electronics in the counting room are protected from

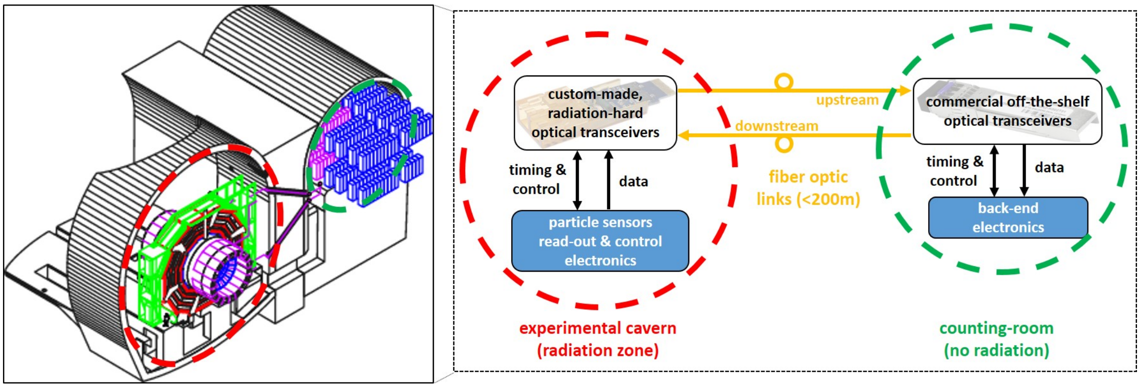

Figure 1.3: Illustration of the two caverns in the CMS experiment accommodating the particle detectors in the experimental cavern (red) and back-end electronics in the counting room (green). The front-end electronics in the radiation zone are connected to the back-end electronics through short fiber optic links.

radiation. To interface front-end and back-end electronics, tens of thousands of fiber optic links shorter than 200 m are installed between the experimental cavern and the counting room. They are used to send timing and control signals from the back-end to the front-end (downstream) and measurement data in the opposite direction (upstream). Despite the short transmission distance, optical links are preferred to electrical links because they typically provide higher bit rates, they consume less power and there is no interference between neighboring channels. Moreover, the material budget close to the innermost detector regions is already very strict. Extra material inside the detector can lead to scattering of the decay particles with this material and deflect their trajectories. Extra volume and mass that is not absolutely required has to be avoided as this would decrease the precision of the vertex measurements. Thin fiber optic links are thus advantageous over more bulky electrical cables.

Two different types of optical TRx are used at either end of the optical links. COTS devices are used in the counting room where there is no radiation. On the other side, custom-made radiation-hard optical TRx are employed in the radiation zone. Custom-made parts are required for this installation because the extreme radiation levels in the experiment would rapidly degrade COTS devices that are not qualified for such environments. This is due to damage created in these devices when collision-products like neutrons, protons, electrons or photons impinge on them [6]. The damage accumulates over time and the devices eventually stop working. A failed device cannot simply be exchanged with a new one as the very compact installation prohibits easy access to the innermost regions of the particle detectors once they are assembled. Device reliability is hence essential as potentially interesting physics data could otherwise no longer be sent from within the experiment to the back-end electronics and were lost. Given the rareness of the events sought, data loss has to be avoided as each successfully recorded event is important for statistical analysis.

Each component inside the experiment needs to be able to withstand the radiation levels expected at the location where it is installed. The closer the installation is to the particle collision point or the beam pipe, the higher the local particle flux and therefore the radiation levels the components need to withstand. Sending data from the innermost detector channels through optical links is consequently challenging. Only specially designed and qualified components can be considered for installation in order to ensure the full operation of the entire detector read-out system.

Custom-made optical TRx for the upcoming LHC upgrade in 2019-2020 were developed in the Versatile Link (VL) project [7, 8]. Those components are based on VCSELs and are currently in series production [9]. The requirements for these devices are strict. They need to have minimal size and mass in order to fit into the foreseen (sub-)detector installation. They cannot be affected by strong magnetic fields (4 T) and therefore metals and magnetic materials should be avoided in the package. They also have to withstand a 1 MeV neutron equivalent fluence (see Sec. 3.1) of $5 \cdot 10^{14}\,\mathrm{n/cm^2}$ and a TID of 10 kGy [10] while supporting a bi-directional bit rate of 4.8 Gb/s.

The Optical fibers themselves can be affected by radiation-induced attenuation, i.e. their losses increase due to the creation of color centers when exposed to ionizing radiation. This increase, however, is more pronounced at shorter wavelength [6] and when long distances of the optical fibers are exposed to radiation [11]. It can hence be neglected up into the MGy-range for the short optical links installed in the HEP experiments at CERN.

1.3 Optical Links for the HL-LHC and beyond

The current LHC schedule already includes another upgrade after that of 2019-2020 (Fig. 1.4). Between 2024-2026, the LHC will be upgraded to the High-Luminosity LHC (HL-LHC). As shown in Fig. 1.4, the energy of the beams will not be changed from the current design value. Instead, the beam luminosity, i.e. the number of protons per bunch, provided to the experiments will be increased by $5-7\times$. More particles per beam implies that more collisions will occur during each bunch crossing, paving the way to explore unprecedented high-energy physics. As a consequence, the TRx will have to handle larger amounts of measurement data and even higher

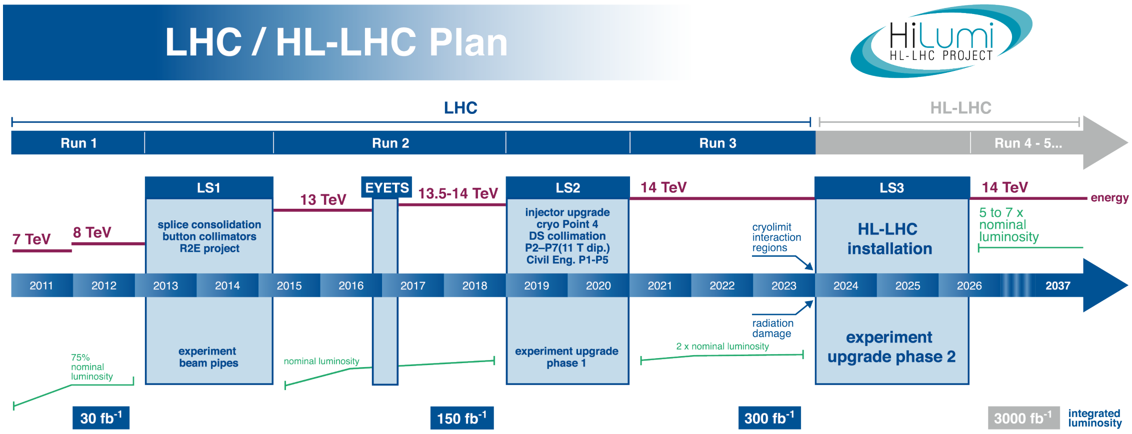

Figure 1.4: The schedule of the LHC/HL-LHC until 2026 and beyond, from [12].

radiation levels than today.

The radiation levels in the CMS detector in the HL-LHC were predicted with simulations [13] and are plotted in Fig. 1.5. The radiation levels are specified for a 10 year operational lifetime as the detector system, including the optical TRx, is not replaceable once it is assembled. Components installed in the experiments therefore have to be able to withstand the accumulated radiation levels over this period. The maximum radiation levels very close to the particle collision point and beam pipe can reach a 1 MeV neutron equivalent fluence of $5 \cdot 10^{16}\,\mathrm{n/cm^2}$ and a TID of 6 MGy. These levels are approximately 10× higher than what the components for the Versatile Link project are made to withstand [14]. As the innermost pixel trackers are only about 4 cm from the beam pipe, the local radiation levels are too high for VL devices to be used to optically read-out data from the pixel trackers and send it to the back-end electronics.

In addition to the higher radiation levels in HL-LHC experiments, future optical TRx also need to provide a bit rate of at least 10 Gb/s [15] to cope with the larger amount of measurement data that will be generated. Research on components addressing this requirement and the need for a higher radiation-hardness is currently ongoing in the Versatile Link Plus (VL+) project [16, 17]. VL+ optical TRx will also be based on VCSELs and are designed to be the workhorse for optical links for most of the detector regions in HL-LHC. They will have a higher bit rate, lower profile height and up to four individual channels compared to their single-channel VL precursors. However, tests have already shown that the extreme radiation levels very close to the particle collision points result in VCSELs degrading too fast [18] to be considered for installation in the innermost detector regions. Therefore, VL+ components will be designed to withstand a neutron fluence of $6 \cdot 10^{15}\,\mathrm{n/cm^2}$ and a TID of 500 kGy [16].

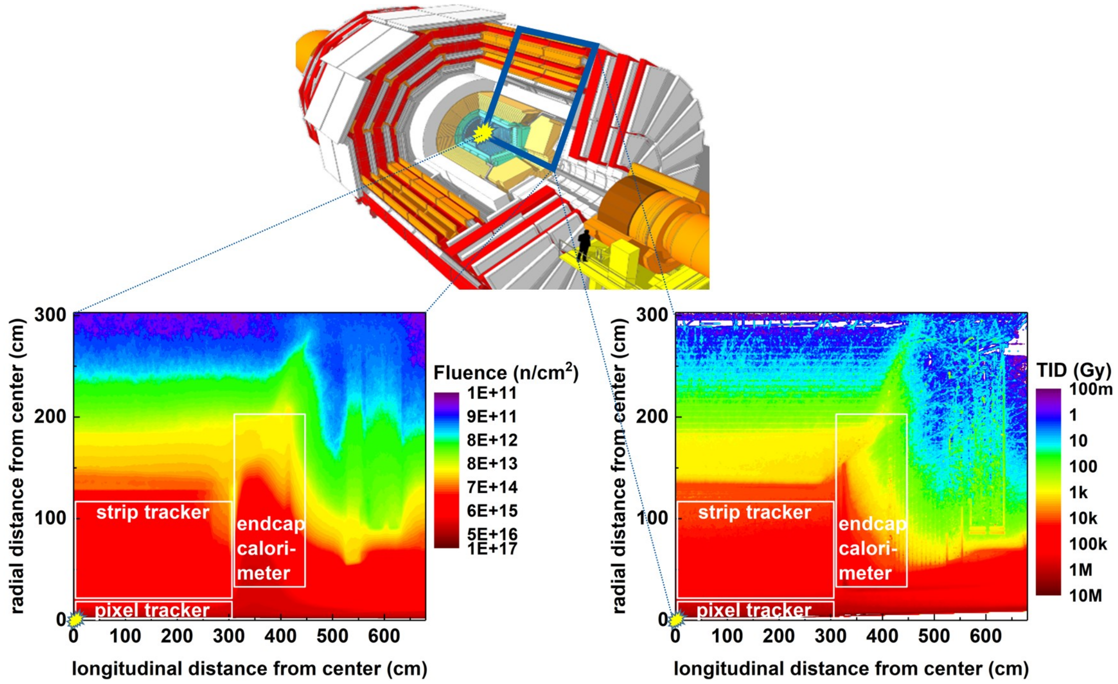

Figure 1.5: Cross-sectional radiation maps showing the 1 MeV neutron equivalent fluence in silicon (left) and TID (right) predicted for the CMS detector in the HL-LHC over a 10 year operational lifetime. The simulated radiation data was taken from [13]. Due to CMS's cylindrical architecture around the beam pipe and symmetry with respect to the particle collision point, the expected radiation levels in other parts of the detector can be mirrored to this map.

These values are high enough to allow the installation of VL+ TRx in most regions of an HEP experiment, i.e. the closest distance they can be installed from the beam pipe is about $20-80$ cm. Otherwise, the neutron fluence will be too high. As indicated in Fig. 1.6, the high neutron fluence occurring in the pixel tracker and the lower part of the endcap calorimeter consequently leaves a region inside the CMS experiment where no VCSEL-based optical links can be installed. Ionizing radiation is less critical for VCSELs as insulating material, susceptible to damage from this kind of radiation (see Sec. 3.2), is far away from the active zone of these devices.

Bridging a distance of just a few centimeters to a region where optical links can be installed with electrical links could be a solution to this problem. However, due to the aforementioned drawbacks that electrical links bring with them, optical links are strongly favored.

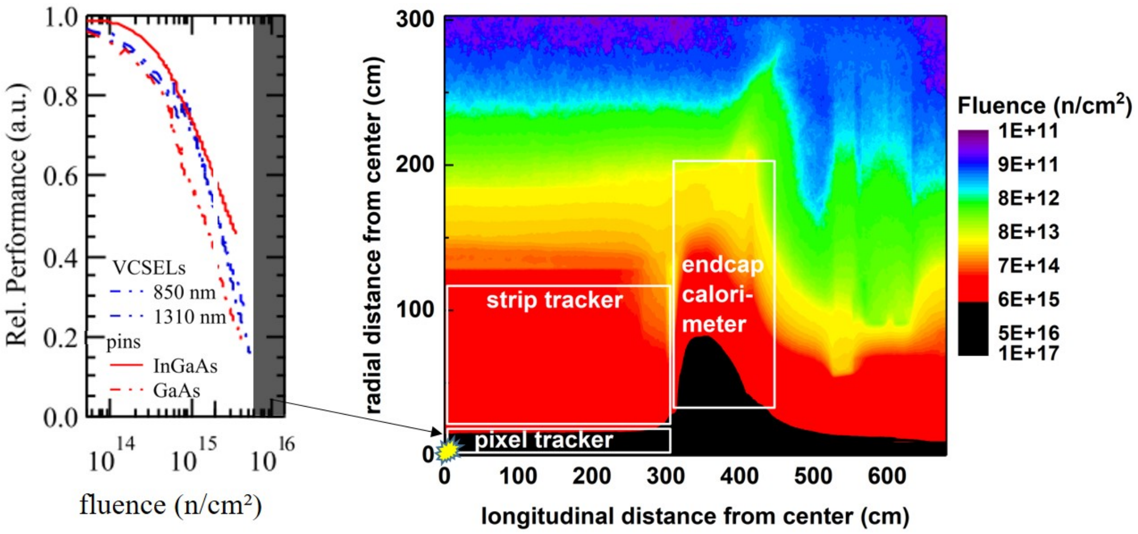

Figure 1.6: Relative degradation of VCSELs and pin-photodiodes as a function of neutron fluence (left) and resulting exclusion region, marked in black, for VCSELs in the CMS detector of HL-LHC (right). The plot on the left was taken from [19]. The relative performances for VCSELs and photodiodes are the slope efficiency and responsivity, respectively.

1.4 Silicon photonics as alternative to VCSEL-based optical links

SiPh is currently being investigated as alternative technology for optical TRx placed close to the particle collision points where VCSEL-based components cannot be installed. SiPh was chosen because silicon has proven to be a reliable and very radiation-hard material for particle detectors [20–24]. For the same reason, SiPh is of great interest to the HEP community. Moreover, due to its compatibility with Complementary Metal-Oxide-Semiconductor (CMOS) electronics [25,26] and thanks to the possibility of high density integration [27, 28], chips with increased functionality and reduced power consumption [29–31] and footprint can be envisioned.

The most important characteristic for HEP applications will be the device's resistance to radiation. Setting the device structure aside, a radiation-hardness for SiPh devices similar to that of silicon pixel sensors [32–35] – in the order of 10^{15} – 10^{16} n/cm^2 – can be expected. Such a high radiation-hardness for optical TRx would allow them to be operated in regions where VCSELs cannot. Integrating them with their driving electronics and possibly even the silicon particle sensors themselves could pave the way to highly integrated read-out modules with potentially lower power consumption and reduced mass and dimensions than currently exist.

The demand for higher bit rate optical TRx can also be addressed with SiPh. SiPh transmitters (Tx) with bit rates higher than the required 10 Gb/s have already been widely demonstrated [36–41]. This has often been achieved with a relatively low power consumption of a few pJ/bit [42, 43]. A low power consumption is also favorable for HEP experiments since the innermost detector regions need to be cooled and a low power dissipation of the optical TRx would reduce the requirements for the cooling system. Nevertheless, the power consumption of SiPh-based TRx would most likely be higher than for VCSEL-based TRx [44] but comparable to electrical links [45].

Further advantages of SiPh Tx over VCSELs would be the additional degree of freedom for the placement of the light source. SiPh Tx are typically fed by an external continuous-wave (CW) laser as opposed to VCSELs that lase themselves. This laser can be placed away from the Tx chip in a region with lower radiation levels. Radiation-induced laser degradation can therefore be reduced and optical links with optimized resistance against radiation can be designed.

The aggregation of several channels into a single optical fiber through Wavelength Division Multiplexing (WDM) [46] can also be done in SiPh while it would be considerably more challenging with VCSELs. WDM would allow an increase in bandwidth of the optical link system without the need to install more optical fibers. First studies of applying WDM in SiPh for HEP applications have already been demonstrated [47].

Due to these benefits, initial tests of SiPh Tx in radiation environments have been carried out. The tests showed very promising results for SiPh MZMs based on a conventional design from Université Paris-Sud [48]. The tested samples showed an insensitivity to radiation-induced phase shift changes up to a 20 MeV neutron fluence high enough for applications in HL-LHC [49, 50]. However, the phase shift of identical devices degraded significantly before HL-LHC levels were reached when irradiated with x-rays [19, 51, 52]. The measured phase shifts from both irradiation tests are plotted in Fig. 1.7. An exclusion region where these samples cannot be installed in the CMS detector of HL-LHC is shown in the same figure. The exclusion region ensues from a failure dose that is defined at the dose where the phase shift falls to below 50 % of the pre-irradiation value.

Even though the tested MZMs exhibit a sufficient resistance against a high neutron fluence, it is still not possible to deploy such devices in the innermost detector regions because of their swift degradation when exposed to ionizing radiation. Reading-out the pixel trackers optically will consequently also not be possible with MZMs based on such a conventional design. Additional research is required to assess whether

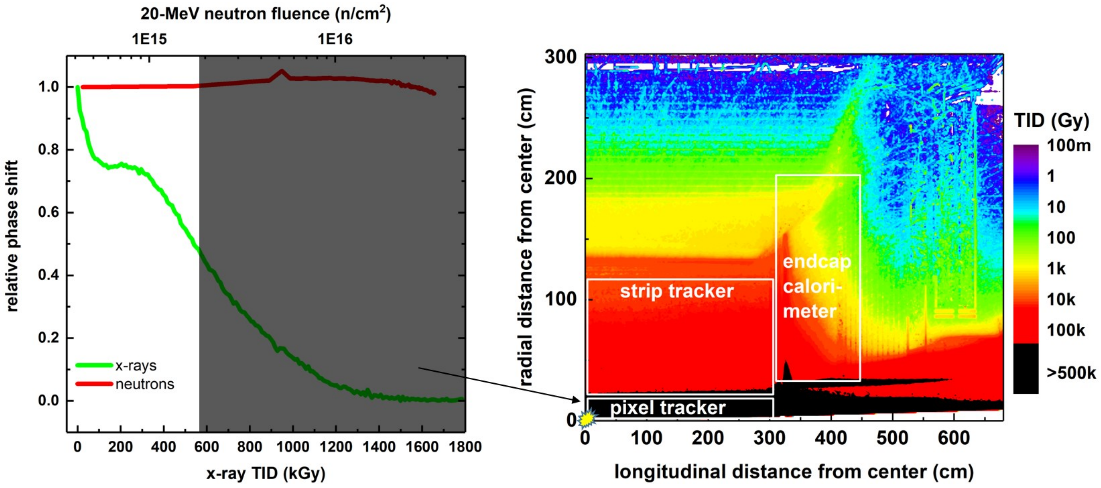

Figure 1.7: Degradation of SiPh MZM based on a conventional design [48] as a function of neutron fluence and TID (left) and resulting exclusion region, marked in black, in the CMS detector of HL-LHC (right).

SiPh MZMs can be designed to show an improved radiation-hardness.

1.5 Summary

The particle collisions in the LHC result in extreme radiation levels and create enormous amounts of measurement data. Radiation-hard optical links are used to send these data from within the HEP experiments to the outside processing electronics. VCSELs are typically used for the transmitting side in these links. An alternative technology will be needed for the innermost regions in future HEP experiments because VCSELs will not be able to withstand the predicted radiation levels close to the particle collision point. SiPh is investigated to determine whether this technology can be deployed in these innermost detector regions. First tests showed promising results with SiPh MZMs being insensitive to irradiation with neutrons. However, the devices strongly degraded when irradiated with x-rays, resulting in a need for additional research into design optimization with respect to radiation hardness.

2 Basics of silicon photonics

The possibility of integrating SiPh devices with electronics and manufacturing them in CMOS-compatible foundries led to widespread research interest in this field over the last decades, both from academia [53–57] and industry [58–63]. Most SiPh device research addressed optical communications but bio-sensing [64–67] and metrology [68, 69] applications have also been studied.

This chapter outlines the basics of SiPh required to follow the work presented later in this thesis. Lasers and photodiodes in SiPh are briefly introduced. SiPh modulators are explained in more detail as they have been the focus of this research. Further details about the various devices and SiPh in general can be found in textbooks [70–74].

2.1 Waveguides

The basic building block of all SiPh devices is an optical waveguide. These are the equivalent of optical fibers in integrated optics and their purpose is to route light through a chip. Total internal reflection is the fundamental principle that guides light in these waveguides. If light in an optically dense medium with refractive index n_1 is reflected and transmitted at an interface to an optically thinner medium with refractive index n_2, the angle of incidence α and the angle of transmission β are related through Snell's law,

$$n_1 \sin\alpha = n_2 \sin\beta. \tag{2.1}$$

This relation is illustrated in Fig. 2.1. When the angle of incidence becomes greater than the critical angle for total internal reflection,

$$\alpha_C = \arcsin\frac{n_2}{n_1}, \tag{2.2}$$

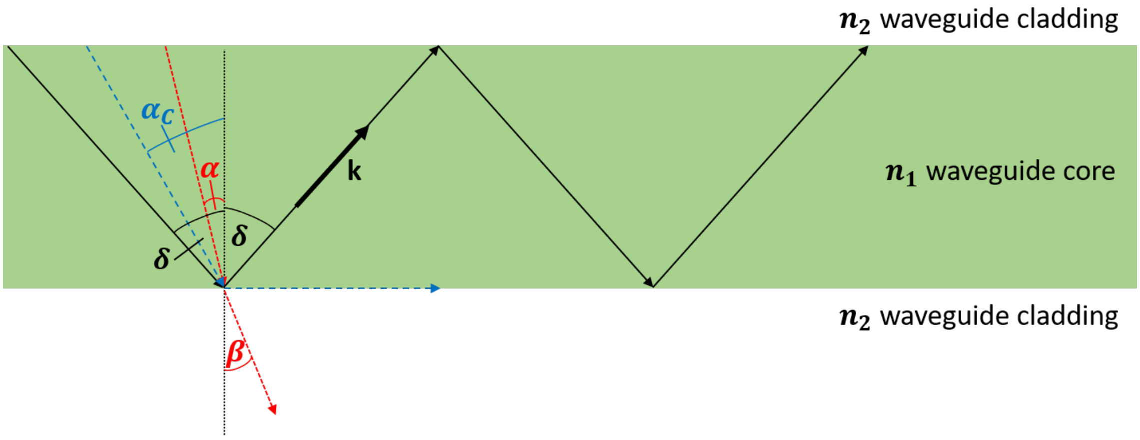

Figure 2.1: Principle of total internal reflection in a waveguide when $n_1 > n_2$. $\boldsymbol{k}$ is the wavevector of light in the waveguide. If the angle of incidence is below the critical angle (red), normal reflection and transmission occurs. At the critical angle (blue), the light is reflected at 90 ° to the interface. For larger angles, the light is guided inside the waveguide (black).

100 % of the light intensity is reflected back at the interface. This effect can thus be employed to confine light in an optically dense material, the waveguide, surrounded by an optically thinner material, the waveguide cladding.

Waveguides can also guide light when they are bent as long as the critical angle of incidence is not exceeded. The critical angle for total internal reflection becomes larger for larger differences between n_1 and n_2 and waveguide bends can be designed with smaller radii. In SiPh, the refractive index contrast is typically achieved by using silicon (Si) as waveguide core material and silicon dioxide (SiO_2) as waveguide cladding material. Sharp waveguide bends, down to a few microns [75], can be realized because of the large contrast between $n_{Si,1550nm} \approx 3.48$ and $n_{SiO_2,1550nm} \approx 1.46$ [76]. This makes high density integration of waveguides and other components possible.

Total internal reflection in the vertical direction of such waveguides is obtained by sandwiching the silicon waveguide layer between two silicon dioxide layers (from now on referred to as “oxide”) as depicted in Fig. 2.2a. Horizontal confinement can be produced by etching into the silicon layer before the top oxide cladding is grown. In this way, the average vertical refractive index in the un-patterned part is higher than in the etched part and light is effectively confined in the horizontal direction as well. Waveguides in which silicon is fully etched away on the sides are called strip waveguides (Fig. 2.2b). Partially etched waveguides are referred to as rib waveguides. Depending on the etch depth, the latter can be further categorized into deep (Fig. 2.2c) or shallow etch (Fig. 2.2d) waveguides. Similar to a large

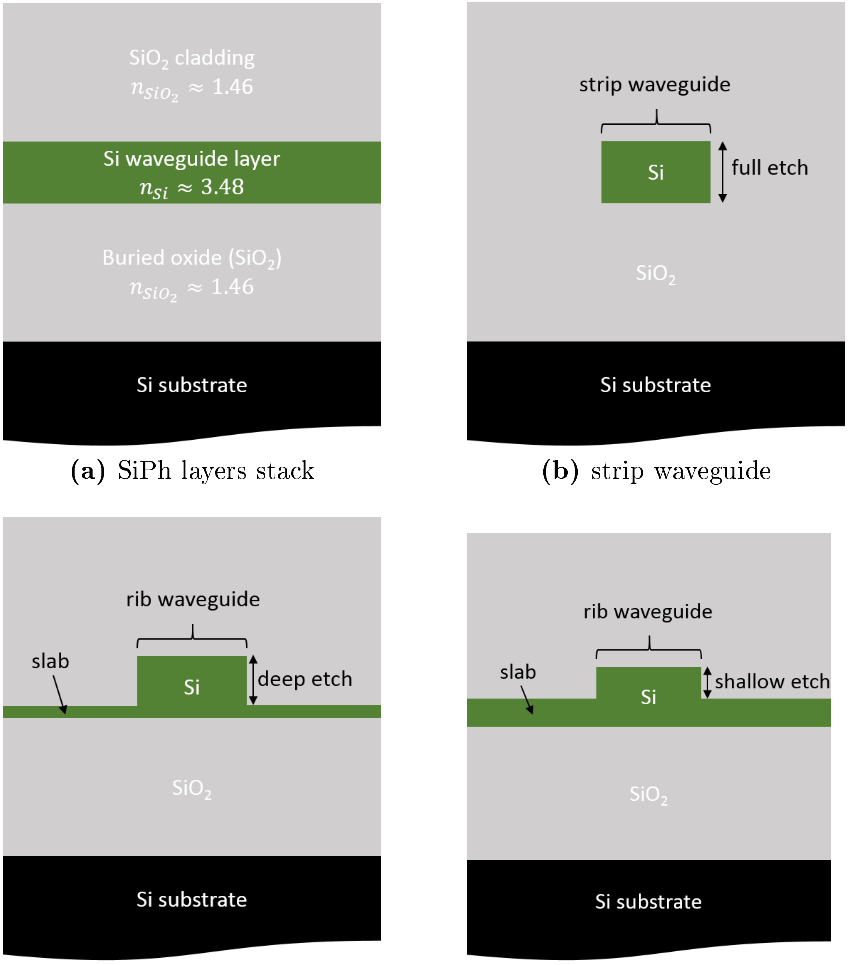

(a) SiPh layers stack **(b)** strip waveguide

(c) deep etch rib waveguide **(d)** shallow etch rib waveguide

Figure 2.2: SiPh layer stack and cross-section of different waveguide types.

difference between the refractive indices of waveguide core and cladding, a deeper etch leads to a stronger confinement of light.

Light that is guided in these waveguides is referred to as an optical mode. Depending on the dimensions of a waveguide, many different optical modes may be guided in it. For optical communications, having only the fundamental mode is often preferred since higher order modes would reduce the quality of a transmitted data signal due to multi-mode interference. The dimensions of a waveguide need to be carefully chosen so only the fundamental mode is guided.

Optical modes are defined by their polarization and eigenvalue, the effective refractive index n_{eff}. They can be mathematically described by the wave equation

$$\nabla^2 \boldsymbol{E} = \left(\frac{n}{c}\right)^2 \frac{\partial^2 \boldsymbol{E}}{\partial t^2}. \tag{2.3}$$

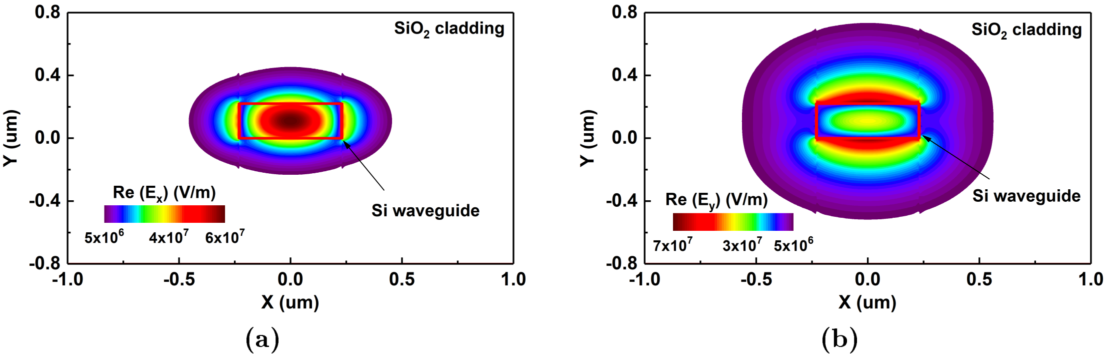

(a) (b)

Figure 2.3: Electric field distribution in a silicon strip waveguide for the fundamental TE (a) and TM (b) mode. Most of the optical power lies within the waveguide core. However, some optical power is guided outside the core with the tails of the optical modes extending into the surrounding cladding material.

Here, c is the speed of light and n is the refractive index of the material in which the mode propagates and $\boldsymbol{E}$ is the vector of the mode's electric field. Typical profiles of the electric field of fundamental modes in a strip waveguide with Transversal Electric (TE) and Transversal Magnetic (TM) polarization are shown in Fig. 2.3. For TE-polarized modes, the electric field oscillates in a plane that is parallel to the waveguide layers. For TM-polarized modes on the other hand, the magnetic field oscillates in that plane. In this case, the electric field is perpendicular to the waveguide layers [70, Chapter 4].

The eigenvalue n_{eff} of the guided modes describes the reduction of the mode's phase velocity as it travels through the waveguide and it links the wavevector of the mode in air $\boldsymbol{k_0}$ to the wavevector of the mode in the waveguide $\boldsymbol{k}$ (see Fig. 2.1),

$$|\boldsymbol{k}| = n_{eff}|\boldsymbol{k_0}|. \tag{2.4}$$

The effective refractive index of a guided mode is thus the equivalent of the refractive index of monochromatic light in a bulk material. The value of n_{eff} is a weighted average of the refractive indices of the core and cladding material and the extension of the mode into the latter. Hence, the refractive index of the waveguide cladding is the lower bound and refractive index of the waveguide core the upper bound for n_{eff}.

The confinement of light in a waveguide can be quantified by means of a confinement factor. The confinement factor describes the ratio of the optical power that is guided in the waveguide core to the total optical power of the guided mode. It is defined as

$$\Gamma = \frac{\iint\limits_{core} |E(x,y)|^2 \mathrm{d}x\mathrm{d}y}{\iint\limits_{-\infty}^{+\infty} |E(x,y)|^2 \mathrm{d}x\mathrm{d}y}. \tag{2.5}$$

The larger the Γ, the better the mode is confined in the waveguide core, i.e. the extension of the modal tails into the surrounding material is minimal.

Optical losses in un-doped waveguides are dominated by the scattering of light, e.g. at bulk defects or at the sidewalls of the waveguide. Since the sidewalls cannot be made perfectly flat during the processing of the waveguide, photons are scattered out of the waveguide at microscopic surface roughnesses. If the surface roughnesses are less than 1 nm, typical waveguide losses are smaller than 2 dB/cm [77] for un-doped waveguides with a height of 220 nm fabricated on a 200 mm-wafer. This value can increase significantly for the doped waveguides needed for active SiPh devices.

2.2 Optical effects in silicon

Variations in the refractive index of the waveguide material, and thus also the effective refractive index of a guided mode, can be employed in active devices for modulating or switching light. The refractive index of crystalline materials can be modified by a range of different effects. Typically, modifications are either induced through changes in the crystal temperature or effects related to its electrical properties.

2.2.1 Thermorefraction

Thermorefraction refers to changes in the refractive index caused by temperature variations. When the temperature of a crystal is changed, the mean lattice distance between adjacent atoms in the crystal increases or decreases. Similar to band gap shrinkage or dilation, this leads to alterations in the interband absorption [78]. According to the Kramers-Kronig dispersion relation, this then leads to changes in the refractive index of the material. The Kramers-Kronig dispersion relation reads

$$n(\omega) = 1 + \frac{\mathcal{P}}{\pi} \int_0^\infty \frac{k(\omega')}{\omega'^2 - \omega^2} \mathrm{d}\omega', \tag{2.6}$$

with $\mathcal{P}$ being the Cauchy principal value, and links the real part n of the complex refractive index to its imaginary part k as a function of frequency ω. Commonly, n is called the refractive index and k is the extinction coefficient of a material. The extinction of light in a material can also be expressed in the more convenient form of an absorption coefficient α that links to the extinction coefficient via

$$\alpha = \frac{4\pi k}{\lambda}, \tag{2.7}$$

with λ being the wavelength of light.

Silicon has a relatively large thermo-optic coefficient of ${}^{\mathrm{d}n}\!/\!{}_{\mathrm{d}T} = 1.86 \cdot 10^{-4}\,\mathrm{K}^{-1}$ [79] and strong changes in n_{eff} can thus be exploited for highly efficient thermo-optic phase shifters [80,81]. However, this also implies that the operation of SiPh devices is inherently very sensitive to temperature variations. Devices relying on resonance effects, in particular ring modulators, need special temperature control mechanisms or thermally isolated waveguides for stable operation [82–84].

Temperature variations near a silicon waveguide can be produced by passing a current through metal strips or doped silicon layers that subsequently change the temperature of the surrounding material. Due to interactions of the optical mode guided in the waveguide with the highly absorbing metal or doped regions, it is important that the heating regions are far enough away from the waveguide to not increase the absorption too much.

2.2.2 Electrorefraction

Effects that change the refractive index at the presence of an applied electric field are referred to as electrorefraction. The applied electric field leads to distortions in the crystal structure and the motion of carriers through the crystal which in turn alters the refractive index n. The strength of this effect depends on the strength of the applied electric field. Changes that scale linearly with the electric field strength can be very strong and are known as the Pockels electro-optic effect. Due to the centrosymmetry of the silicon crystal structure, however, unstrained silicon does not exhibit the Pockels effect. Modifications of the refractive index that scale quadratically with the strength of the applied electric field are called the Kerr effect. This effect is present in all crystalline materials but it was demonstrated to be weak in silicon [85] and it is thus not used for SiPh devices.

2.2.3 Electroabsorption

In contrast to electrorefraction, electroabsorption refers to electric field-induced changes in the absorption of a material. In bulk semiconductors, this effect is called the Franz-Keldysh effect. If an applied electric field tilts the valence and the conduction band edge in a semiconductor, photon-assisted tunneling of carriers from the valence to the conduction band can occur. This causes a red-shift of the absorption spectrum and unlike in an un-tilted band structure, photons with energies below the band gap can be absorbed. This change in photon absorption leads to a change in refractive index via the aforementioned Kramer-Kronig dispersion relation.

Silicon shows a strong Franz-Keldysh effect near its band gap of 1.1 eV, which corresponds to a wavelength of approximately 1130 nm. This is too far away from the main optical communications wavelength window of interest ($\approx 1300\,\mathrm{nm} - 1600\,\mathrm{nm}$) to be used for SiPh devices. Germanium (Ge) on the other hand also shows a strong Franz-Keldysh effect that lies within this wavelength window. Since Germanium can be integrated with silicon during device processing, high performance SiGe Electro Absorption Modulators (EAMs) have been demonstrated based on this effect [86–89].

2.2.4 Plasma Dispersion Effect

Changes in absorption of photons induced through changes in the free carrier concentration in a semiconductor are described by the Plasma Dispersion Effect (PDE). The PDE is present in all crystalline materials. For silicon, that is transparent in the optical communications wavelength range, electrons cannot absorb photons and be excited from the valence band to the conduction band. Intraband transitions, however, can still lead to photon absorption as long as the energy and momentum in this process is conserved. Since silicon is an indirect semiconductor, phonons or impurities are required to provide the additional momentum for the absorption process to occur. Injecting carriers into or depleting carriers from a diode-like structure is therefore a common way to manipulate the free carrier concentration and enhance or suppress intraband absorption. Similar to thermorefraction, this leads to changes in the refractive index of the region in which the carrier concentration changes.

The change in refractive index n and absorption coefficient α as a function of free hole N_h and electron N_e concentration are given by the Drude Lorenz equations,

$$\Delta\alpha = \frac{e^3\lambda^2}{4\pi^2c^3\varepsilon_0 n}\left(\frac{N_e}{\mu_e m_e^{*2}} + \frac{N_h}{\mu_h m_h^{*2}}\right), \tag{2.8}$$

$$\Delta n = \frac{-e^2\lambda^2}{8\pi^2c^2\varepsilon_0 n}\left(\frac{N_e}{m_e^*} + \frac{N_h}{m_h^*}\right) \tag{2.9}$$

with the fundamental charge e, speed of light c, vacuum permittivity ε_0. $\mu_{e,h}$ and $m_{e,h}^*$ are carrier mobilities and effective masses for electrons and holes, respectively. Soref and Bennet examined the change in absorption $\Delta\alpha$ and in the refractive index Δn of silicon as a function of the free carrier concentration for the telecommunications wavelength bands. They deduced simple, semi-empirical equations [85, 90] that nowadays are widely used for silicon photonic device design and simulation. At $\lambda = 1.3\,\mu\text{m}$, the equations read

$$\Delta n = -6.2 \cdot 10^{-22}\Delta N_e - 6.0 \cdot 10^{-18}(\Delta N_h)^{0.8}, \tag{2.10}$$

$$\Delta\alpha = 6.0 \cdot 10^{-18}\Delta N_e + 4.0 \cdot 10^{-18}\Delta N_h. \tag{2.11}$$

For $\lambda = 1.55\,\mu\text{m}$, the formulas become

$$\Delta n = -8.8 \cdot 10^{-22}\Delta N_e - 8.5 \cdot 10^{-18}(\Delta N_h)^{0.8}, \tag{2.12}$$

$$\Delta\alpha = 8.5 \cdot 10^{-18}\Delta N_e + 6.0 \cdot 10^{-18}\Delta N_h. \tag{2.13}$$

As can be seen in Eqns. (2.10) - (2.13), to achieve a significant change in absorption of refractive index, large changes in the free carrier concentration are required. This is why active SiPh devices relying on the PDE are highly doped, typically in the order of $10^{17} - 10^{18}\,\text{cm}^{-3}$. Such high free carrier concentrations also increase the absorption significantly and a compromise between increase in absorption and change in refractive index has to be found by optimizing the doping profile.

2.3 Lasers

Naturally-occurring silicon is an indirect band gap material. The momentum of an electron when it emits or absorbs a photon is thus not automatically conserved. Additional momentum is required for both processes to occur. As additional momentum cannot be provided systematically, the process of stimulated emission in silicon cannot be controlled. Efficient lasers, needed as light sources for SiPh TRx, cannot be made in natural silicon. Approaches for lasers in strained silicon [91] or with Germanium-on-Silicon (GeSi) [92] have been demonstrated in labs but are still far from commercial viability [93].

The currently preferred alternative is hybrid integration of III-V gain materials, such as InP-compounds, with silicon waveguides [94–96]. This allows the development of silicon-based lasers that can be used as light sources for SiPh TRx. However, due to the challenges of integrating two different material systems, such lasers show inferior performance over traditional III-V lasers. They are nonetheless efficient enough for commercial applications [97].

In contrast to typical commercial applications, lasers would not be directly integrated on-chip for HEP applications. Instead, they would be placed away from the SiPh chips and the two would be connected with optical fibers. This approach enables the use of COTS III-V lasers that can be placed far enough away from the innermost detector regions. In this way, radiation-induced damage on the laser can be minimized simply by avoiding the extreme radiation levels.

2.4 Modulator types

Owing to the fact that there are no efficient lasers in natural silicon, directly modulated laser links are not possible with SiPh. Indirectly modulated links based on a modulator fed by an external light source are used in SiPh instead. Several different types of modulators have been proven to work for this purpose. Interference-based modulators like a Mach-Zehnder Modulator (MZM) offer a broadband spectral operation (dozens of nanometers) and a higher tolerance against process variations and environmental changes than resonant-devices [98, 99]. The drawbacks of MZMs are that their footprint is rather large ($> 0.5\,\text{mm}^2$) and they consume a considerable amount of electrical power. This is because their modulation efficiency is not as high as for other modulator types.

On the other hand, ring modulators are small ($< 0.01\,\text{mm}^2$) and consume little power thanks to their high modulation efficiency [100, 101]. This comes at the cost of a very narrow spectral operation window ($< 1\,\text{nm}$) and a high sensitivity to fabrication variations. Furthermore, resonance-based modulators such as ring modulators or Bragg grating modulators [102] are usually extremely sensitive to temperature variations. Therefore, these device types are not well suited for application in HEP experiments where varying temperatures can be found.

Germanium-on-Silicon-based EAMs can have a small footprint, wide modulation bandwidth and low power consumption [103]. However, their spectral operation is also limited to a narrow window near the absorption edge of germanium [104]. This could pose a problem for HEP applications in a varying temperature environment where the wavelength might drift due to thermal changes in the laser. Moreover, the radiation-hardness of similar devices (III-V EAMs) was already assessed and demonstrated to be too low for the targeted application [105].

2.5 Silicon Mach-Zehnder modulator

Mach-Zehnder modulators were chosen to be investigated for HEP applications due to its maturity and robustness against environmental changes and because of the drawbacks of the other modulator types.

2.5.1 Principle of operation

The Mach-Zehnder modulator is one of the most common photonic modulator types fabricated in integrated opto-electronics today. One reason for this is their widespread implementation in $LiNbO_3$- and InP-based photonic modulators for long-haul optical communications. The fundamental concept of such a modulator type dates back to 1891/92 when Ernst Mach and Ludwig Zehnder invented the Mach-Zehnder Interferometer (MZI). As with every interferometer, the optical output power of an MZI is modulated by means of interfering light beams. In their original experimental setup, Mach and Zehnder split an incoming light beam equally into two separate beams and introduced an optical path length difference between them. Depending on this path length difference, both light beams accumulate different phases with respect to each other until the point where they recombine. This phase difference can be exploited to produce either constructive or destructive interference at the interferometer output. The resulting amplitude modulation in an MZI is thus effectively realized by phase modulation in one or both interferometer arms. Constructive interference occurs when the two beams are in-phase, i.e. when the phase shift obeys $\Delta\phi = 2\pi m$ with m being an integer. Destructive interference can be observed for $\Delta\phi = \pi j$ when j is an odd integer.

In integrated photonics, MZMs are used to convert an electrical data stream into

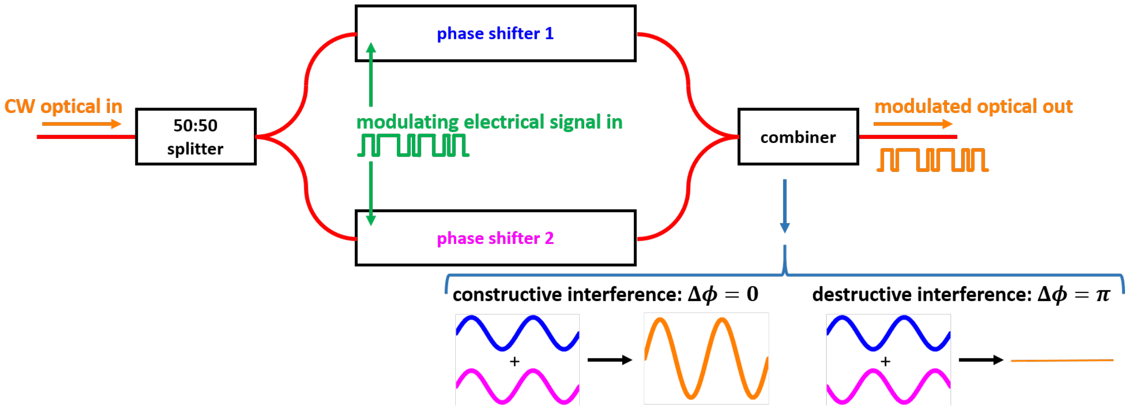

Figure 2.4: Principle of an MZM showing the conditions for the phase shift that leads to constructive and destructive interference at its output. Optical waveguides are shown in red. The splitter and combiner are typically based on Multi-Mode Interference (MMI) couplers [106–108].

an optical data stream. The principle is the same as for an MZI but realized on-chip. A schematic of an integrated MZM in shown in Fig. 2.4. Since the physical path length L cannot be altered on-chip, the optical path length nL has to be modified in order to create a phase shift between the two beams. Phase shifters are therefore incorporated into both waveguides of the MZM to be able to manipulate the refractive index through the Plasma Dispersion Effect described above.

Changes to the material's refractive index n also affect the effective refractive index of the guided mode in the MZM's waveguides. The resulting phase shift after the light beams traveled through the phase shifters can be expressed as [109]

$$\Delta\phi = \frac{2\pi\Delta n_{eff}L}{\lambda}. \tag{2.14}$$

The changes in the effective refractive index Δn_{eff} are determined by the overlap integral between the optical mode and the region where the carrier concentration, and so indirectly also the refractive index, changes. The overlap integral is [110]

$$\Delta n_{eff} = \iiint_{-\infty}^{+\infty} \frac{\Delta n(x,y,z)|E(x,y,z)|^2}{|E(x,y,z)|^2} \mathrm{d}x\mathrm{d}y\mathrm{d}z, \tag{2.15}$$

with E being the amplitude of the electric field of the optical mode and x, y being the spatial coordinates perpendicular to the propagation direction z of the light beam in the waveguide.

The larger the overlap between optical mode and the region in the phase shifter where the refractive index varies, the larger the change in effective refractive index of the guided mode and the better the phase shifter design. Well-designed phase

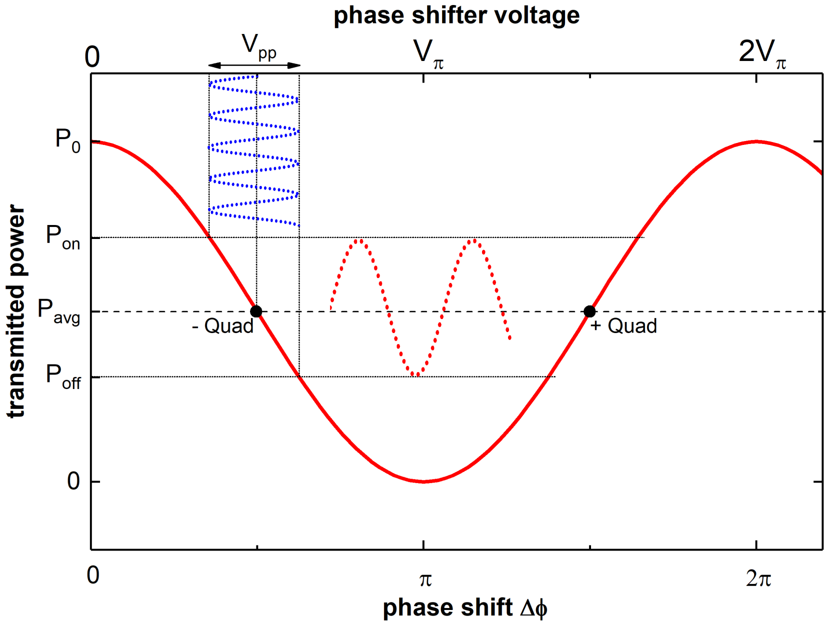

Figure 2.5: Transfer function of an ideal MZM showing the power transmitted through an MZM as a function of phase shift or voltage V_π required to obtain a phase shift of π. The quadrature points (±Quad) around which an MZM is typically modulated and peak-to-peak modulation voltage V_{pp} are highlighted.

shifters exhibit a high phase modulation efficiency, i.e. a phase shift of π can be obtained for low voltages V_π applied to phase shifters with a short length. A typical figure of merit is expressed in units of Vcm, where lower numbers indicate higher phase modulation efficiencies.

The optical output power of an ideal MZM depends on the phase shift of the two recombining light beams with respect to each other and is given by the periodic transfer function [111]

$$P_{out} = \frac{P_{in}}{2}\left[1+\cos\left(\Delta\phi\right)\right] = \frac{P_{in}}{2}\left[1+\cos\left(\frac{2\pi\Delta n_{eff}L}{\lambda}\right)\right], \tag{2.16}$$

where P_{in} is the optical power coupled into the modulator and absorption losses being neglected in this formula. This transfer function is plotted in Fig. 2.5. The plot illustrates that a phase shift as close to π as possible maximizes the difference between the MZM's on- and off-state optical power levels. That so-called extinction ratio, in dB given by

$$ER = 10\cdot\log\left(\frac{P_{on}}{P_{off}}\right), \tag{2.17}$$

is an important property of modulators used for optical communications. For large extinction ratios, it becomes easier for an optical receiver (Rx) to distinguish between zero- and one-levels of a transmitted data stream and the number of bit errors can be reduced. An alternative measure for the difference between the MZM's on- and off-state optical power levels is the Optical Modulation Amplitude (OMA). It relates the average optical power level P_{avg} of the modulated signal to the linear extinction ratio $r_e = {}^{P_{on}}/_{P_{off}}$ and is defined as

$$OMA = 2P_{avg}\frac{r_e - 1}{r_e + 1} = P_{on} - P_{off}. \tag{2.18}$$

Similar to the ER, a larger OMA implies a better modulation performance. According to these definitions, the ER remains unaffected if there is attenuation or amplification in an optical link whereas the OMA changes. The OMA is used in Chapter 6 to quantify eye openings because the absolute power levels at the Rx ultimately decide whether it can correctly identify a bit and therefore keep the Bit-Error-Rate low.

2.5.2 Phase shifter configurations

Three different kinds of phase shifters exist that all exploit the PDE in silicon. All of them rely on p- and n-doped regions inserted into the waveguides of an MZM and the resulting change in the free carrier concentration when a voltage or current is applied to them. The three different types are based on either carrier injection, carrier accumulation or carrier depletion.

Injection-type phase shifters

A forward-biased pin-diode is commonly used for injection type phase shifters. A schematic of such a phase shifter is shown in Fig. 2.6. The waveguide is in the intrinsic (un-doped) region of the pin-diode. Due to the absence of dopants, absorption losses are relatively low when no voltage is applied. When a voltage is applied and carriers are injected into the waveguide, losses increase and the change in carrier concentration induces a change in n_{eff}. This change can be relatively large because of the large change in free carriers. A phase shift of π can hence be achieved in relatively short injection-type phase shifters.

The modulation speed of this phase shifter type is determined by the recombination lifetime of the minority carriers in the junction. As their lifetime is relatively long ($100\,\mathrm{ns} - 1\,\mu\mathrm{s}$), the modulation speed is rather slow with bandwidths in the range

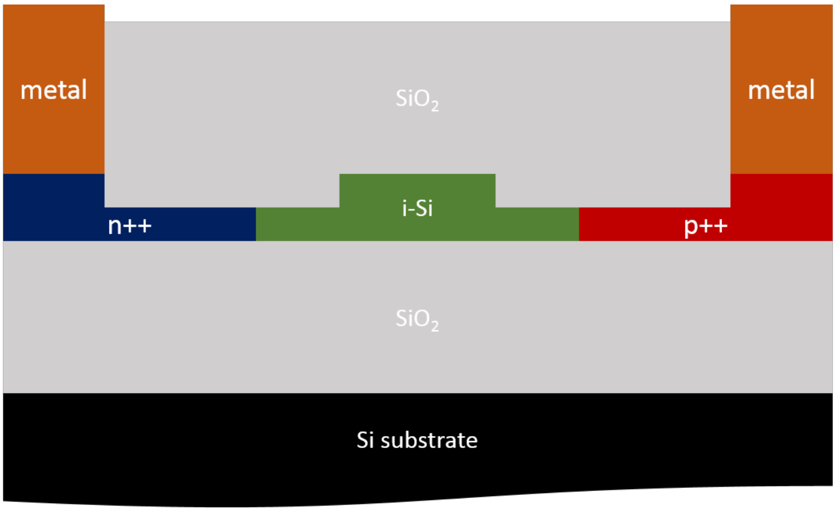

Figure 2.6: Schematic of an injection-type phase shifter based on a pin-diode. n++ and p++ indicate highly n- and p-doped silicon, respectively. Intrinsic (un-doped) silicon is labeled with i-Si.

of MHz [72]. This limitation can be overcome by using pre-emphasis driving signals where the leading edge of the drive signal has a higher voltage than the average voltage during the actual pulse. MZMs with bit rates up to 25 Gb/s have been demonstrated based on this technique [41,112]. The drawback of using pre-emphasis driving signals is the need for more complex and thus more expensive electrical circuits.

A further drawback of this structure is that the power consumption of injection-type phase shifters is comparatively high due to forward currents in the mA range. In addition, pin-diodes are known to be not very radiation-hard because the intrinsic regions can become p-type under irradiation [113]. This causes the depletion region to shift in the waveguide of the phase shifter. Consequently, the overlap with the optical mode becomes smaller and the device loses its efficiency and eventually even its functionality.

Accumulation-type phase shifters

The first ever SiPh MZM with a bandwidth in the GHz-regime was demonstrated by Intel in 2004 [114] using an accumulation-type phase shifter. In contrast to a phase shifter with pin-diode, the recombination of electrons and holes is prevented in this device type by inserting an oxide barrier of few nm thickness in the waveguide between the n- and p-doped regions (Fig. 2.7). In this way, electrons and holes accumulate at both sides of the barrier when injected into the waveguide and locally increase the free carrier concentration. This again leads to a change in n_{eff}.

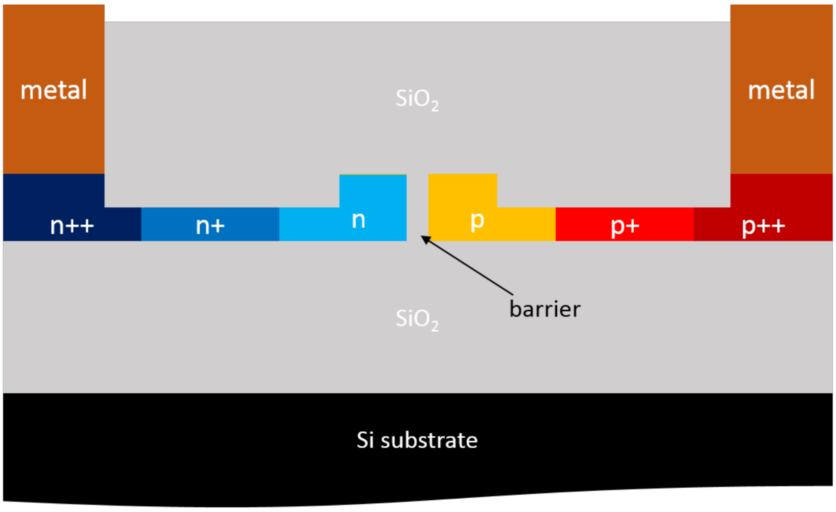

Figure 2.7: Schematic of an accumulation-type phase shifter with a barrier between the n- and p-doped regions.

The modulation bandwidth of an accumulation-type phase shifter is not limited by the minority carrier lifetime since the carriers do not recombine. High-speed and very efficient devices have been demonstrated with speeds up to 40 Gb/s [115]. Furthermore, no significant current can flow in these devices which reduces its power consumption.

On the downside, this structure is more complex to fabricate because of additional process steps required to make the device, particularly when poly-silicon is used together with crystalline silicon to form the conductive paths between the barrier [115]. For HEP application, introducing an oxide layer into the active region of a device should also be avoided since the oxide is very sensitive to radiation damage because of charge buildup (see Section 3.2).

Depletion-type phase shifter

The most often cited phase shifter type is based on carrier depletion from a pn-junction. Many different devices with various junction positions and shapes have been published [116–120]. A cross-section of a depletion-type phase shifter with lateral pn-junction is shown in Fig. 2.8. As opposed to the other two device types, pn-junction phase shifters are reverse-biased to remove carriers from the depletion region and widen it. The reduction in free carriers leads to a change in the effective refractive index n_{eff} with the opposite sign when compared to the other two device types. For the same reason, the absorption reduces when a voltage is applied to the phase shifter.

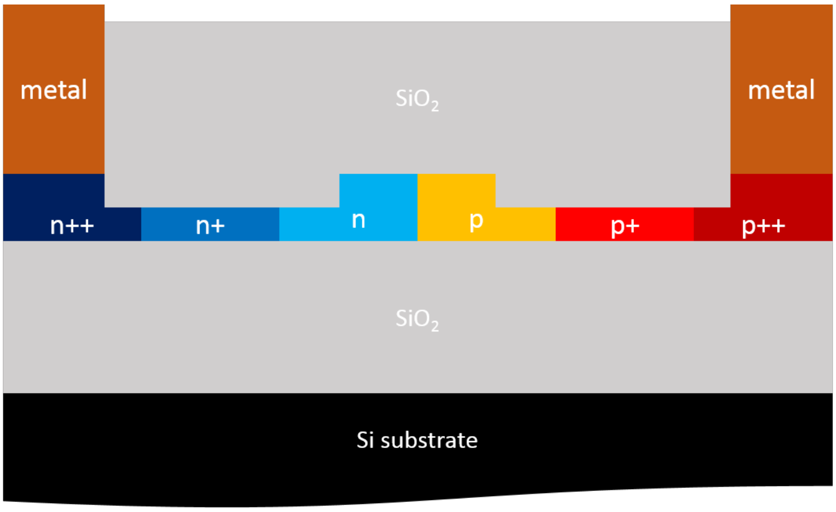

Figure 2.8: Schematic of a depletion-type phase shifter with lateral pn-junction.

Since electrons and holes do not recombine in a pn-diode under reverse bias, the dynamic processes in a depletion-type phase shifter are dominated by the majority carrier lifetime which is typically in the range of picoseconds for these devices. The intrinsic cutoff frequency is thus very large and the modulation bandwidth is usually limited by the inherent series resistance R_S and capacitance C_J of the pn-junction. The modulation bandwidth for MZMs with lumped electrodes can be estimated through [121]

$$f_{3dB} = \frac{1}{2\pi R_S C_J}. \tag{2.19}$$

MZMs optimized for high-speed performance have been demonstrated with bit rates up to 60 Gb/s [122] and modulation efficiencies below 1 Vcm at 1 V reverse bias [123].

Depletion-type phase shifters show the lowest phase modulation efficiencies of all configuration types. They thus need to be relatively long to produce a phase shift of π. Nonetheless, it is the most promising phase shifter type for commercial applications because of its relatively easy fabrication and demonstrated performance.

Crucial for the functionality of all phase shifter types is that carriers can be injected or depleted from the active region in the waveguide to induce a phase shift. The observed x-ray-induced phase shift degradation (see Fig. 1.7) suggests that this mechanism is most likely inhibited by damage created through ionizing radiation. Improving the device's radiation-hardness thus implies mitigating this consequence and maintaining the ability to move carriers in and out of the phase shifter even after exposure to high TID levels.

2.6 Silicon-Germanium photodiodes

Photodiodes (PDs) are required to convert an optical data stream back into an electrical data stream on the receiver side of an optical link. Photodiodes are also needed for feedback and control loops in integrated circuits. Unfortunately, silicon PDs cannot be used for this purpose since silicon is transparent in the wavelength range of interest. Luckily, germanium is a very good absorber in the optical communications wavelength range with a band gap of 0.66 eV (which equals a wavelength cutoff of 1800 nm). Accordingly, GeSi PDs are used to add the photon detection capability to the SiPh platform.

Thanks to the CMOS-compatible epitaxial growth of germanium on silicon, waveguide integrated GeSi PDs nowadays show a performance comparable with their more mature III-V counterparts. With dark currents below 0.1 µA at -1 V bias [124], responsivities of almost 1 A/W [125] and bit rates of up to 40 Gb/s [126–128], GeSi PDs are well suited for high-speed and low-power integrated SiPh.

2.7 Summary

Silicon Photonics offers the possibility to integrate lasers, modulators and photodiodes in a CMOS-compatible process. A common modulator-type in this technology are Mach-Zehnder Modulators (MZMs) that are based on interfering light beams. They are mature and robust against fabrication variations and environmental conditions. Modulating the optical path length in these devices can be achieved by applying a voltage to a pn-junction that is incorporated into a silicon-waveguide surrounded by silicon dioxide. In this way, carriers are depleted from or injected into the waveguide and the resulting changes in the carrier concentrations then translate to changes in the refractive index of silicon through the Plasma Dispersion Effect. Depletion-type MZMs were chosen as candidate devices for radiation-hard optical links in HEP applications because injection- and accumulation-type MZMs are likely more susceptible to damage from radiation.

3 Radiation effects in silicon devices

Many different charged and neutral decay particles are produced when protons collide in the (HL-)LHC. These secondary particles radiate away from the particle collision point into all directions and can sooner or later impinge on the components installed in the particle detector. The resulting particle-matter interactions can be in the form of e. g. Rayleigh scattering, Compton scattering or elastic and inelastic scattering [6]. What all those interactions have in common is that they will result in an energy transfer from the impinging particle to the target material. This transfer of energy can create defects in the target which in turn alter the material and device properties [129], resulting in increased power consumption, reduced speed or even complete loss of functionality of a device.

Fundamentally, two basic damage mechanisms can be distinguished. First, displacement damage caused by non-ionizing energy loss of heavy particles. Displacement damage is particularly relevant in semiconductor materials because it can create defects leading to levels appearing in the band gap. The second damage mechanism is Total Ionizing Dose (TID) damage caused by energy loss of ionizing particles. This effect is especially problematic in insulators, for instance like in the oxide as used for the cladding in SiPh waveguides. The basics of both mechanisms are described in this section.

Single Event Effects (SEE) like those relevant in electronic Integrated Circuits (ICs) [130–132] are not described here. They refer to single ionizing particles that impinge on a circuit or device and result e. g. in a short circuit or a change in a signal level. SEEs play mainly a role when it comes to the radiation-hardness of submicron devices because of the limited volume that can be affected by an single ionizing particle. However, the energy of single particles is typically not sufficient enough to affect devices with feature sizes as big as those in SiPh MZMs ($> 15\,\mu\text{m}^3$).

Further information on particle-matter interactions beyond the scope of this theoretical introduction can be found e. g. in [133–139].

3.1 Displacement damage through non-ionizing energy loss

High energy particles, e. g. protons, neutrons or heavy ions, impinging on a target material can displace atoms from their lattice sites and create defects, i.e. irregularities in the otherwise regular crystal structure. This so-called bulk damage is illustrated in Fig. 3.1. The displacement of atoms originates from the transfer of kinetic energy from the impinging particle to the target, either through elastic or inelastic scattering. If enough energy is transferred to an atom, it can be knocked out of its lattice position. This Primary Knock-on Atom (PKA) often immediately recombines again with its now vacant lattice position. If the atom escapes this initial recombination, it leaves behind a lattice vacancy and finds a new position outside the regular atomic lattice. This atom is then called interstitial atom and together with the vacant lattice position it is known as Frenkel pair. Typically, the PKA knocks out further atoms that can also act as PKAs while they move through the atomic lattice before they recombine or become trapped. This process can provoke entire damage cascades which lead to the formation of clusters of lattice defects.

The irregularities in the crystal lattice give rise to energy states in the otherwise forbidden band gap. These states can act as generation-recombination centers or permanent and temporary trapping sites for carriers in deep and shallow states in the band gap, respectively. Furthermore, they can lead to compensation of donor and acceptor levels, reduced carrier mobilities or type conversion of dopants due

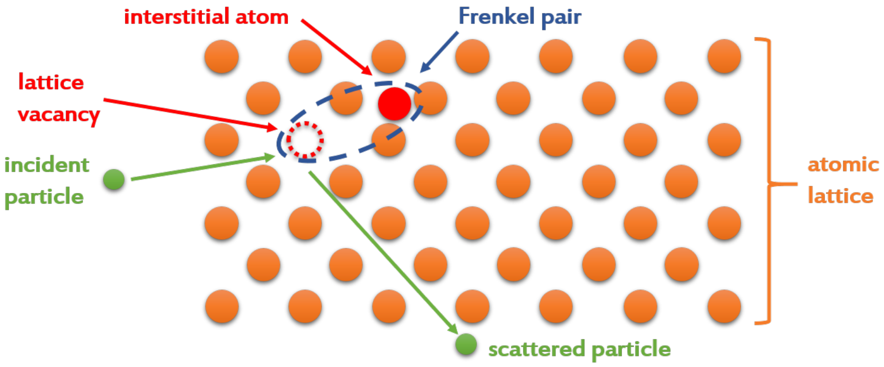

Figure 3.1: Creation of displacement damage in bulk semiconductors when an incident particle displaces an atom from it lattice position. The resulting lattice vacancy and interstitial atom together are referred to as Frenkel pair.

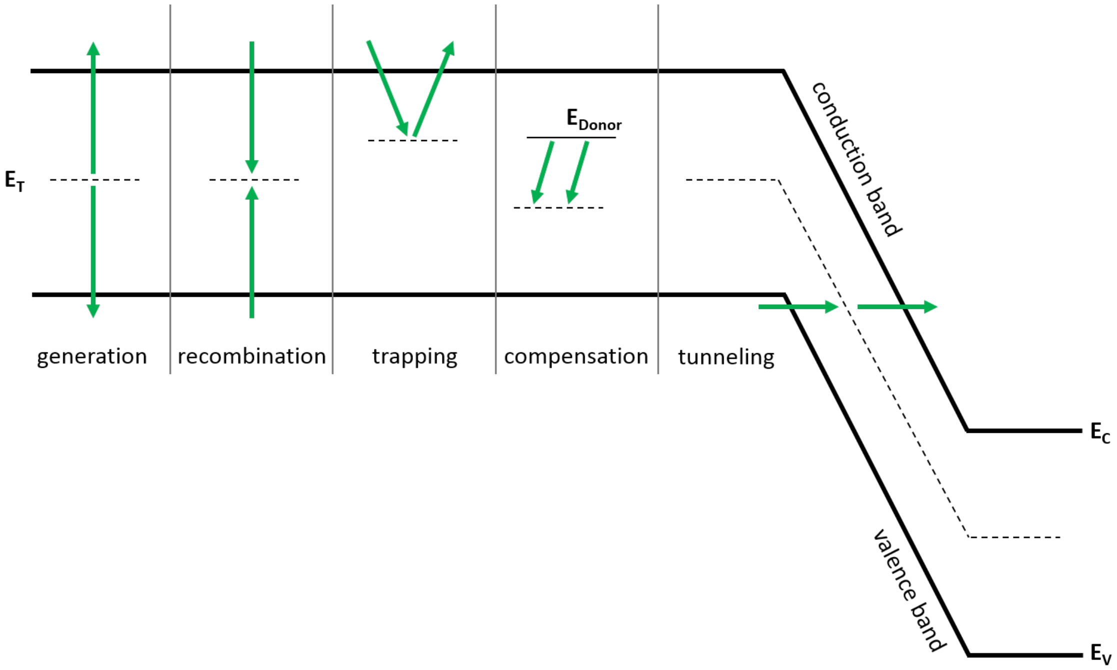

Figure 3.2: Semiconductor band structure with possible defect types created through displacement damage, after [141].

to carrier removal [140]. The different damage processes are depicted in Fig. 3.2. Changes to the doping concentrations in semiconductor devices and electron hole pair creation can significantly degrade the performance of electrical and optical devices. For instance, n-doped regions can become intrinsic or even p-doped when electrons are stripped away [113]. This would affect the position of a pn-junction in SiPh MZMs which in turn might no longer be able to provide the desired phase shift.

The amount of displacement damage caused scales linearly with the Non-Ionizing Energy Loss (NIEL) of the incident particles [142]. The NIEL coefficient depends on the material- and radiation-type. It measures the amount of energy that is lost per unit length by the impinging particle through non-ionizing processes. According to the NIEL hypothesis, it is assumed that the bulk damage created is proportional to the total kinetic energy imparted to replace an atom and the mass m of the target. The corresponding equation that relates the Kinetic Energy Released in Matter (Kerma) K to the radiation- and the material-dependent NIEL coefficient reads

$$K = NIEL \cdot \Phi \cdot m, \tag{3.1}$$

with Φ being the flux of the impinging particles [6].

The NIEL coefficient is a useful means to compare displacement damage in a specific target material caused by different kinds of radiation and allows the correlation of this damage to other test conditions. An often-used standard metric is the so-called 1 MeV-equivalent neutron fluence in silicon. This metric describes the damage produced in silicon by neutrons having an energy of 1 MeV. Damage created by other particles can be converted to that metric and measured radiation resistances can easily be compared.

This standard metric has been chosen because the sensitivity of devices to displacement damage is often tested with neutron radiation. This is because neutrons are uncharged particles and consequently cannot directly create TID damage [6]. Therefore, neutron irradiation tests are a relatively straightforward method to test for displacement damage.

Such neutron irradiation tests of SiPh MZMs were already carried out and showed that their phase shift was not significantly affected up to a very high neutron fluence (see Fig. 1.7). An intuitive explanation for this insensitivity is that a 1 MeV-equivalent neutron fluence of about $1 \cdot 10^{15}\,\mathrm{n/cm^2}$ creates a defect density in silicon of a few $1 \cdot 10^{15}\,\mathrm{cm^{-3}}$ [142]. For lower fluence levels the corresponding defect density scales linearly with the neutron fluence. Based on the NIEL hypothesis, it can be assumed that this linear dependence can be extrapolated to a fluence of up to $1 \cdot 10^{16}\,\mathrm{n/cm^2}$ and the corresponding defect density would be in the order of $10^{16}\,\mathrm{cm^{-3}}$. This is at least one order of magnitude lower than the typical doping concentration in SiPh MZMs, which effectively is just another form of a defect in the crystal structure. The insensitivity of SiPh MZMs to displacement damage can thus be attributed to the fact that the density of doping-like defects is much higher than the defect density induced by radiation of high energy particles.

3.2 Total ionizing dose damage through ionizing energy loss

While x-ray or γ-radiation can be very energetic, from a few keV to a few MeV, the energy of the photons is typically not high enough to directly displace atoms from their lattice sites. Instead, electrons are excited to higher energy states and electron-hole pairs (ehps) are created when an ionizing particle is scattered in a target material. This is of special relevance in insulator materials because the created ehps can become permanently trapped and the electrical characteristics of a device

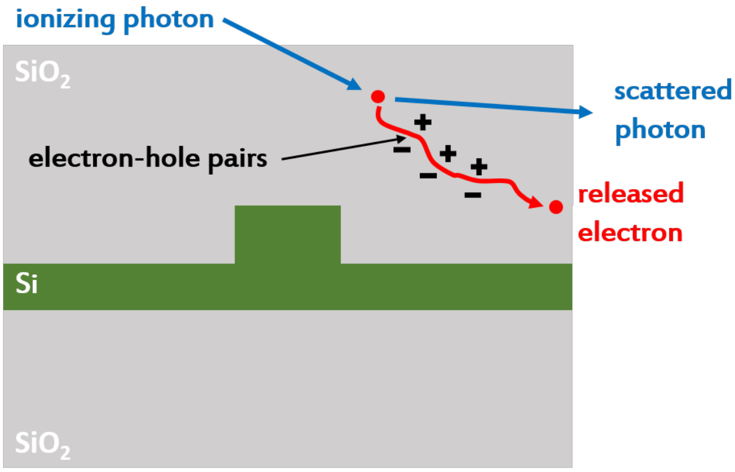

Figure 3.3: Creation of TID damage when an photon excites an electron that travels through the oxide and creates electron-hole pairs along its track.

can change.

The process of charge creation from an incident photon is depicted in Fig. 3.3. An incident high energy photon is scattered at an atom in the target material. Upon impact, some of its kinetic energy is transferred to an atom's electron which is subsequently released. This electron then travels though the material and loses energy by further scattering. The energy can be used to produce additional ehps along the track of the initial electron.

The number of ehps created by radiation depends on the density ρ and the ionization energy E_{ion} of the target material as well as the absorbed radiation energy ΔE. The ionization energy is typically twice the band gap energy, i.e. 18 eV for silicon dioxide. The density of silicon dioxide is $2.27\,\mathrm{g/cm^3}$. The generation rate of ehps for a TID of $1\,\mathrm{rad} = 0.01\,\mathrm{Gy}$ then becomes [143]

$$g_0 = \frac{\Delta E}{E_{ion}} = 7.88 \cdot 10^{12} \frac{1}{\mathrm{cm^3 rad}}. \tag{3.2}$$

Some of the ehps recombine again promptly, similar to a displaced atom with its vacant lattice position for displacement damage. Other ehps escape the recombination process. The ratio of ehps that escape the prompt recombination is determined by the strength of the electric field at the position where an ehp was created and the type of radiation impinging on the material. The higher the electric field strength E, the higher the probability that the two carriers will be separated due to their drift in the electric field before they can recombine. The yield $Y(E)$ of ehps that

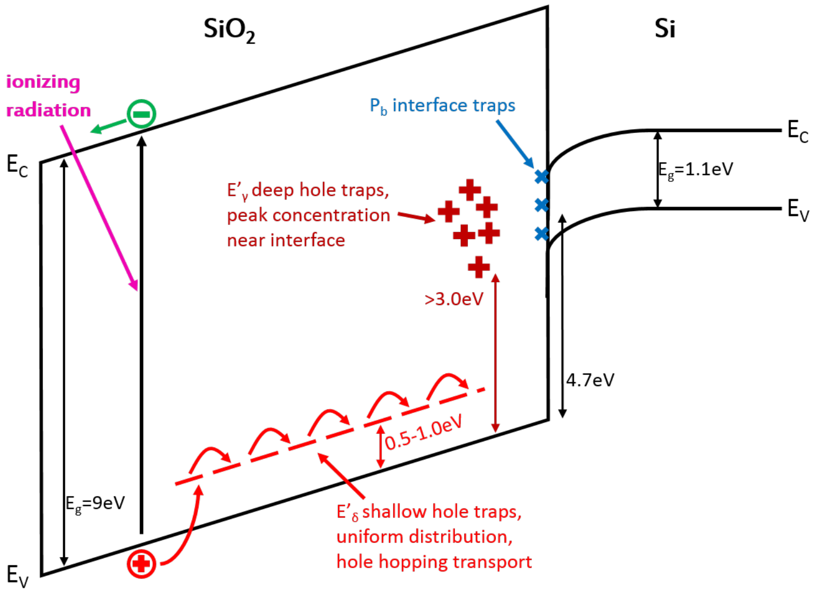

Figure 3.4: Creation, transport and trapping of ehps in oxide, after [133].

escape recombination can be calculated through

$$Y(E) = \left(\frac{E + 0.1\,\mathrm{V/cm}}{E + E_0} \right)^{m_Y}, \tag{3.3}$$

with E_0 and m_Y being radiation-dependent constants [144]. For x-rays, they are $m_Y = 0.9$ and $E_0 = 1.35\,\mathrm{MV/cm}$, while for γ-radiation $m_Y = 0.7$ and $E_0 = 0.55\,\mathrm{MV/cm}$ [143].

The total number of created ehps that do not promptly recombine becomes

$$N_{ehps} = g_0 \cdot Y(E) \cdot TID. \tag{3.4}$$

These charges undergo drift and diffusion transport. Since electrons have a much higher mobility than holes ($\mu_e = 20\,\mathrm{cm^2/Vs}$, $\mu_h = 10^{-5}\,\mathrm{cm^2/Vs}$ [145]), it is generally accepted that all electrons leave the oxide either via the device's anode or through tunneling into silicon [138]. Holes on the other hand remain in the oxide and are considered to move through it by hopping transport [146]. Figure 3.4 shows the entire process schematically. The hopping transport is enabled through shallow defect sites, referred to as E'_δ vacancies, with an energy of $0.5 - 1.0\,\mathrm{eV}$ above the valence band and uniformly distributed throughout the oxide. This defect type belongs to the group of neutral oxygen vacancies, commonly referred to as E' centers [147]. The other important defect type of this group are deep trap levels with energies greater than $3.0\,\mathrm{eV}$ above the valence band [148]. They are called E'_γ vacancies and follow a Gaussian distribution in the oxide with the peak concentration near the silicon/oxide interface [149]. The occupancy of both E' centers can vary as they can exchange charge with adjacent silicon layers via tunneling within a few nanometers from the silicon/oxide interface [150]. For theoretical considerations, however, deep traps are usually considered fixed [151].

The holes moving through the oxide can cause two main effects in it [152]. The first one is trapping of positive charge in the bulk oxide [153, 154]. While the holes hop from one shallow defect level to another, they can fall into pre-existing deep traps levels and become permanently trapped. The number of trapped holes depends on the density of pre-existing defect states in the oxide which is related to the oxide quality. The higher the oxygen vacancy density, the worse the oxide quality and the less radiation-hard it is [155]. The fabrication of silicon devices with its many different process steps has an important impact on the device performance with respect to radiation-hardness [156]. The density of oxygen vacancies can for instance be minimized by using low instead of high temperature annealing during device processing [157]. Using hydrogen during fabrication, e. g. during wet oxide growth or polishing, should also be avoided since it also reduces the oxide quality [158]. Oxides for SiPh are usually not specifically treated and are thus expected to have relatively large defect densities.

Besides becoming permanently trapped, holes can also initiate the second main effect in the oxide, the buildup of interface traps at the interface with silicon. Protons can be released from the oxide if radiation-induced holes interact with hydrogen defects therein [159]. These protons show a very high diffusivity and can accumulate at the silicon/oxide interface [160]. If they reach the interface, they can react with hydrogen-passivated silicon and form dangling bonds via to the following reaction [161]

$$SiH + H^+ \rightarrow Si^+ + H_2. \tag{3.5}$$

Here, Si^+ is the interface trap and is called a Pb center [162]. The most abundant forms often used in simulations are an acceptor level and a donor level at 0.3 eV and 0.85 eV above the valence band of silicon, respectively [163].

3.3 Hydrogen-induced dopant passivation

Apart from the buildup of interface traps, the passivation of deep and shallow dopants in silicon [164–167] is another damage mechanism that involves hydrogen and can be induced by ionizing radiation. Hydrogen species, which are released by radiation-induced electrons or holes from defects in the oxide, can not only accumulate at and react with the interface but also tunnel into adjacent silicon layers [168]. There, hydrogen atoms or ions can bond to boron acceptor or phosphorous donor atoms and passivate them. Excess carriers in silicon provided by the dopants are annihilated in such a reaction. As a result, the free carrier concentration in silicon decreases while the mobility of the remaining free carriers increases [169]. This process is also called hydrogenation.

Concentrations of hydrogen species in the order of $1 \cdot 10^{18} - 1 \cdot 10^{20}\,\mathrm{cm}^{-3}$ near silicon interfaces and concentrations as high as $1 \cdot 10^{18}\,\mathrm{cm}^{-3}$ up to 500 nm deep into silicon [170–172] highlight that the dopant passivation process can affect very highly doped regions deep into the material [173].

As dopant passivation and interface trap creation both involve hydrogen impurities, it is assumed that both are correlated and have a similar dependence on TID. In particular, hydrogen can tunnel more easily through the silicon/oxide interface and trigger the passivation process when interface traps are present [174]. However, the passivation efficiency for boron and phosphorous is different [175]. Reasons include that hydrogen diffuses relatively fast into P-doped silicon and that its diffusion profile resembles that of the boron implantation [176]. In contrast, the diffusion of hydrogen into n-doped silicon is slower [176]. Furthermore, hydrogen binds more tightly to boron than to phosphorous [169]. Hence, the passivation of boron is stronger than that of phosphorous [177].

3.4 Summary

Damage from radiation can occur to semiconductor devices via ionization and/or displacement damage. The latter is of little concern in SiPh MZMs because of the very high doping concentration in these devices. Ionizing radiation on the other hand can lead to the generation of trapped positive charge in oxide layers and interface traps as well as the passivation of dopants in silicon. These defects change the electrical properties in SiPh MZMs and can ultimately lead to device failure. An MZM design that mitigates these defects and shows an improved radiation-hardness against ionizing radiation thus needs to be identified.

4 Design of a silicon photonics test chip

The initial irradiation tests of SiPh MZMs based on a conventional design clearly showed that these devices are barely affected by neutron radiation but degraded until their phase shift eventually disappeared when irradiated with x-rays. Inspired by these outcomes, a SiPh chip was designed and fabricated in an external foundry to determine whether SiPh MZMs can be radiation-hardened by design [178,179]. The chip included twelve different MZMs with varied design parameters that allow a detailed assessment of which parameters affect the radiation-hardness of SiPh MZMs. Six of those MZMs were building block devices pre-designed by the foundry where the chips were fabricated. These building block devices are expected to deliver the performance specified by the foundry but are not necessarily radiation-hard. The other six MZMs were custom-designed modulators. The simulations performed to ensure a proper design for these custom-designed MZMs, the integration of the findings from the simulations into a mask layout and results from functional verification tests are presented in this chapter.

4.1 Multi-project wafer runs at imec

The SiPh chip was designed for fabrication in a Multi-Project Wafer (MPW) run offered by imec [180] and organized through ePIXfab [181]. An MPW run was chosen for this prototyping work as the costs of fabrication are comparatively low because they are being shared among several users. Imec's MPW fabrication process relies on the 130 nm process node and Silicon-On-Insulator (SOI) wafers with a diameter of 200 mm. The design freedom in such an MPW run is limited as it would otherwise be impossible for the foundry to fabricate the wafers at an affordable cost for the individual user. On the other hand, the foundry can offer pre-designed building block devices that will provide a guaranteed minimum performance due to the established process conditions. Examples for offered building blocks include

MZMs, ring modulators, photodiodes and waveguides. This allows customers to create more complex photonic integrated circuits without the need for profound device expertise.

A schematic cross-section through a phase shifter for the chosen MPW run at imec indicating the relevant design parameters is shown in Fig. 4.1. The following design parameters are constant in the process flow: concentration of the contact (n++/p++) and intermediate (n+/p+) doping implantations, thickness of the Buried Oxide (BOX, 2 µm) and top oxide (1 µm) waveguide cladding and height of the active silicon layer (220 nm). The height of the active silicon layer was chosen such that only the fundamental modes for TE- and TM-polarization are guided in the vertical direction [77]. General single-mode operation can then easily be satisfied by defining the width of the waveguide accordingly.

Design parameters that could be varied in the MPW are the following: width of the waveguide w, etch depth h of the waveguide (full etch, shallow etch with 150 nm thick slab or deep etch with 60 nm thick slab), n- and p-doping concentrations in the waveguide (nominal doping or 2× nominal doping) as well as the width w_{Dop} of the waveguide doping. The width of the waveguide doping should not significantly affect the overall performance of the MZMs if the intermediate n+/p+ doping is not too close to the waveguide rib. If w_{Dop} is too small, however, it will yield increased absorption losses due to interactions of the optical mode with the intermediately doped regions. w_{Dop} was nonetheless included in the parameter set to be varied to assess whether it will affect the MZM's phase shift degradation when irradiated with x-rays.

Since the design freedom is limited in an MPW, the number of possible MZM designs is also restricted. In total, eight different custom-design MZMs for a wavelength around $\lambda = 1550$ nm were included in the chip layout:

- MZM with deep etch waveguide and nominal doping in the pn-junction,
- MZM with shallow etch waveguide and nominal doping in the pn-junction,
- MZM with deep etch waveguide and 2× nominal doping in the pn-junction,
- MZM with shallow etch waveguide and 2× nominal doping in the pn-junction.

Each of these four configurations comes with two different values for the waveguide doping width w_{Dop}. MZMs having the nominal doping come from one wafer, MZMs having 2× the nominal doping come from another wafer. The chosen designs were inspired by findings published in [182]. According to these results, a shallow etch waveguide and high doping concentrations in the pn-junction of the phase shifters

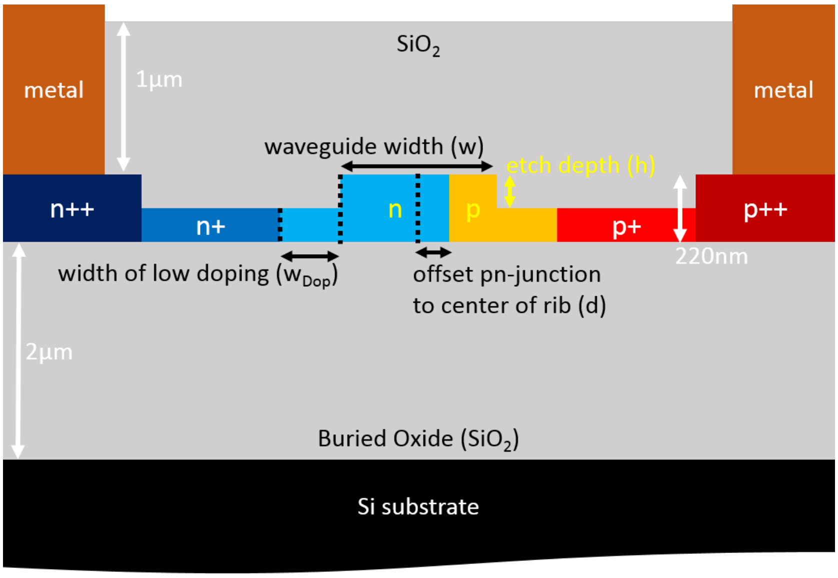

Figure 4.1: Schematic cross-section through a phase shifter from an imec process. Constant process parameters in an imec MPW are shown in white, continuously variable parameters in black and discretely variable parameters in yellow.

should improve the radiation-hardness of SiPh MZMs against ionizing radiation because a larger density of free holes in the waveguide slab would delay a radiation-induced pinch-off (cf. Sec. 5.3.2).

The length of the custom-design MZMs could have been also varied in the imec MPW. It was kept constant, however, because building block MZMs with varied length were used to assess the effect of this design parameter on the radiation-hardness.

Four custom-design MZMs for operation at a wavelength around $\lambda = 1310\,\text{nm}$ were also included in the chip layout, in case tests at this wavelength had to be performed. These devices come with either a deep etch or shallow etch waveguide, one value for w_{Dop} and both doping concentrations.

4.2 Optimization of phase shifter design

Setting the radiation-hardness aside, a large phase shift generally leads to a better modulation performance of MZMs. Therefore, the phase shifter design of the different MZMs must be optimized to achieve the largest possible phase modulation efficiency while keeping the losses to an acceptable level. Static electro-optical simulations were employed for this purpose. The radiation-hardness of the MZMs was not taken into account in the simulation at this stage.

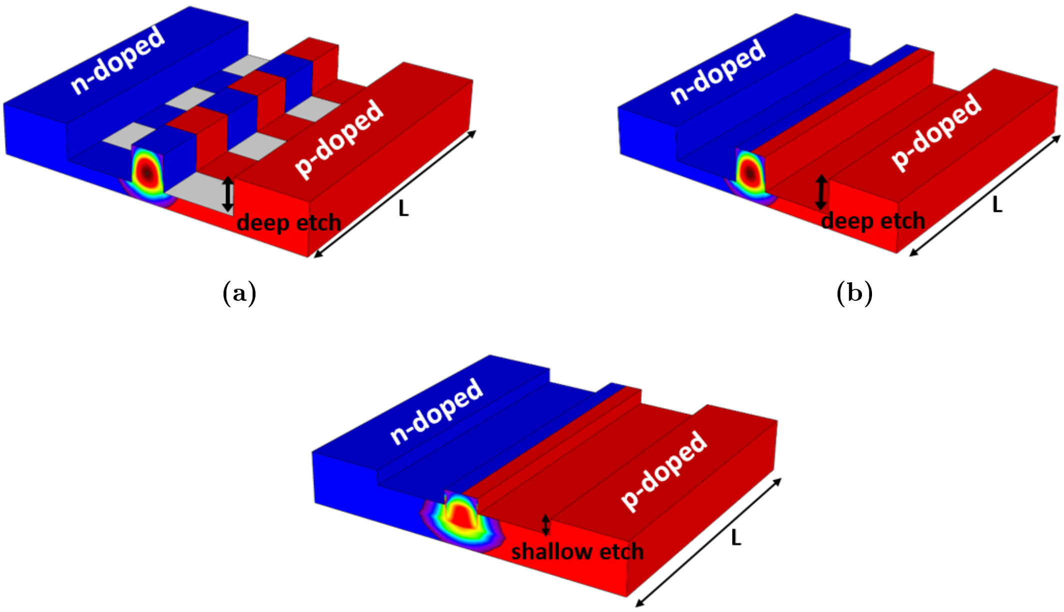

(a) (b)

(c)

Figure 4.2: Schematics of a deep etch phase shifter with interleaved pn-junction (a) as well as deep (b) and shallow (c) etch phase shifters with lateral pn-junction. The gray regions between n- and p-doped fingers in devices with interleaved pn-junctions are un-doped silicon regions. The different shape of the fundamental mode guided in these waveguides results from the different etch depths.

4.2.1 Simulation procedure

The phase modulation efficiency can be evaluated by calculating and comparing the phase shift of different MZMs at a given voltage. For this, the effective refractive index n_{eff} of the optical mode in the doped silicon waveguide of the phase shifter needs to be computed. This can be done by simulating the spatial distribution of the electron and hole densities in the doped silicon waveguide as a function of applied voltage and using the results to convert the carrier densities into a spatial distribution of complex refractive indices via the Soref-Benett Eqns. (2.10 - 2.13).

The 2D carrier densities for MZMs with lateral pn-junction were simulated with the Synopsys Sentaurus TCAD toolbox [183]. 3D simulations did not need to be carried out in this case since the devices are uniform along the z-direction (the direction of the waveguide). In contrast, the carrier densities in MZMs with interleaved instead of lateral pn-junctions, e. g. as depicted in Fig. 4.2 or published in [184, 185], also vary along the z-direction and hence 3D simulations would be necessary to obtain accurate results. MZMs with interleaved pn-junctions were not simulated since their radiation-hardness was investigated based on building block MZMs that were already optimized by imec.

As stated in Sec. 2.5.1, the phase shift is determined by the overlap of the optical mode with the region where the carrier concentrations change when a voltage is applied. Consequently, the width of the waveguide and the position of the pn-junction in it can be used to optimize the phase modulation efficiency of MZMs. Simulations were employed to find the optimal waveguide width and pn-junction position using a range of values for both parameters. The waveguide width was varied between 400 nm and 480 nm for deep and shallow etch MZMs. The width range was chosen such that the waveguide is as wide as possible, since this leads to a larger phase modulation efficiency [74, Chapter 9], while at the same time being not too wide to support more than the fundamental optical mode.

The position of the pn-junction inside the waveguide was varied because, according to the Soref-Benett equations, changes in the hole density create a larger variation in the refractive index and lower absorption losses than changes in the electron density. Due to this asymmetry, phase shifters are often designed with a higher n- than p-doping concentration and the pn-junction is then off-centered from the waveguide towards the n-doped region. In this way, the depletion region extends further into the p-doped region than into the n-doped region when a reverse biased is applied. This can be seen with the equations for the depletion widths W_n and W_p for n- and p-doped regions, respectively, that read [186, p. 83]

$$W_n = \sqrt{\frac{2\varepsilon_0\varepsilon_r}{e}\frac{N_A}{N_D(N_A+N_D)}(\Psi_{bi}-V)}, \tag{4.1}$$

$$W_p = \sqrt{\frac{2\varepsilon_0\varepsilon_r}{e}\frac{N_D}{N_A(N_A+N_D)}(\Psi_{bi}-V)}, \tag{4.2}$$

where ε_0 is the vacuum permittivity, ε_r the relative permittivity, N_A the concentration of acceptors and N_D the concentration of donors. The built-in potential Ψ_{bi} of the pn-junction is given by

$$\Psi_{bi} \approx \frac{kT}{e}\ln\left(\frac{N_A N_D}{n_i^2}\right), \tag{4.3}$$

with the Boltzmann constant k, temperature T and the intrinsic carrier density n_i. To account for the effect of holes being more efficient in inducing a phase shift than electrons, the offset of the pn-junction with respect to the center of the waveguide needs to be determined for a given doping concentration. In the simulations, the absolute offset d from the center of the waveguide was determined relative to the width w of the waveguide (see Fig. 4.1 for parameter assignments) and is given through

$$d = w * d_{offset} \quad \text{e. g.} \quad 40\,\text{nm} = 400\,\text{nm} * 0.1. \tag{4.4}$$

Here, d_{offset} is a relative offset factor that was varied between -0.3 and 0.2 in the simulations. A positive sign indicates an offset towards the p-doped region whereas a negative sign denotes an offset towards the n-doped region.

The implantation profiles for all six implantations (contact, intermediate and waveguide doping for n- and p-type implants) were derived from approximate information about the peak implantation depths and concentrations that was received from imec (precise implantation information is confidential and was not disclosed). The peak implantation depths were used to deduce the energies of the implantation process step in the "Stopping and Range of Ions in Matter" (SRIM) [187] application. Based on these findings, SRIM simulations were performed to get the distribution of the implants in 220 nm thick silicon. The profiles obtained were then fitted and normalized to the expected peak concentrations and used in the Sentaurus TCAD device simulations. The lateral broadening of the implantation profiles with respect to the implantation direction, the so-called straggle, for the different energies was taken from [188].

The simulation was performed in several steps as depicted in Fig. 4.3. The phase shifters with the geometry and doping concentration to be simulated were constructed and meshed in the Sentaurus Structure Editor. This output was then used to solve the Poisson equation and current continuity equations as a function of applied reverse voltage (0 V, 1 V, 2 V, 3 V) in Sentaurus Device to obtain the electron and hole concentrations. For the electron and hole concentrations in silicon, Fermi statistics were used in the simulations. Further, band gap narrowing and the following models were enabled:

Carrier Recombination

Doping- and temperature-dependent Shockley-Read-Hall (SRH) recombination, including field enhanced SRH lifetimes,
Auger recombination,
Avalanche generation,
Band to band carrier tunneling,
Interface SRH recombination.

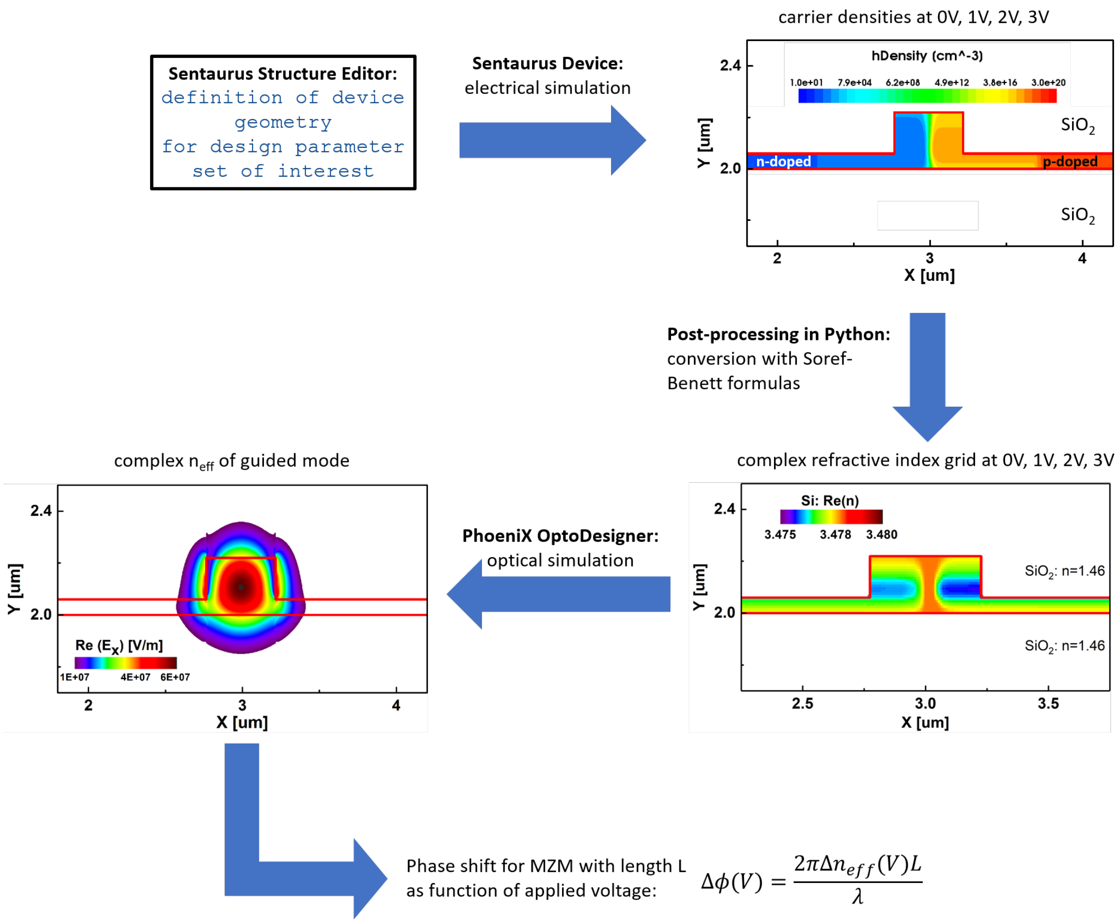

Figure 4.3: Simulation flow diagram from the definition of a device in the Sentaurus Structure Editor to the calculation of the carrier densities in Sentaurus Device and the simulation of the complex n_{eff} in PhoeniX OptoDesigner.

Carrier Mobility

Doping-dependent mobility degradation,
Temperature dependence of mobility,
Carrier velocity saturation due to high electric fields,
Mobility degradation at material interfaces.

The default parameter settings provided with the simulation software were used for all models.

The simulated carrier densities at a given voltage were exported from Sentaurus Device to convert them into a grid of complex refractive indices (Fig. 4.3) with the Soref-Benett formulas. These grids of refractive indices for the voltages of interest were then imported into PhoeniX OptoDesigner [189]. There, a finite difference mode solver was employed to calculate the complex effective refractive index n_{eff} of the guided modes in the simulated waveguide for each applied voltage. The change in refractive index

$$\Delta n_{eff} = n_{eff}\Big|_{0\,\mathrm{V}} - n_{eff}\Big|_{V_1} \tag{4.5}$$

and the resulting phase shift at a voltage V_1 as well as the loss coefficient of the waveguide at 0 V could then be calculated.

4.2.2 Simulation results

Phase shift and loss calculations were produced for each MZM configuration as a function of waveguide width w and pn-junction offset d_{offset}. Example results for the phase shift $\Delta\phi$ per unit length for deep and shallow etch MZMs with nominal doping and waveguide doping width $w_{Dop} = 400\,\mathrm{nm}$ or $w_{Dop} = 600\,\mathrm{nm}$ at an applied reverse voltage of 3 V are shown in Fig. 4.4. Simulations on MZMs having 2× the nominal doping were not carried out as the geometrical designs are the same to their equivalent MZMs with nominal doping. This is to ensure that MZMs with identical design parameters except for the doping concentration can be compared. They are expected to have larger phase shifts and losses due to the higher doping concentrations used.

Comparing the results for MZMs with different etch depth, deep etch MZMs have generally larger phase shifts than shallow etch MZMs. This can be attributed to a larger confinement factor Γ, as given in Eq. (2.5), for the optical mode in the deep etch waveguide than in a shallow etch waveguide (Fig. 4.5). As a result, the overlap between optical mode and depletion region is enhanced for deep etch waveguides.

The largest phase shift for both etch depths was found when the pn-junction is centered in the waveguide (zero offset). Based on the received approximate information about the implantations, the n- and p-doping implants are supposed to be of almost equal concentration. The depletion region will hence extend almost symmetrically into both regions under reverse bias, compare Eqns. (4.1) and (4.2). The overlap integral of the optical mode's electric field with the depletion region is thus largest when the pn-junction is not offset with respect to the waveguide center. In contrast, if the pn-junction were closer to the edge of the waveguide ($d_{offset} = 0.2$ or -0.3 in Fig. 4.4), the overlap between depletion region and optical mode would go down and the phase shift decrease.

The simulations further show that the phase shift of deep etch MZMs is barely affected by the waveguide width. This is because the optical mode in deep etch

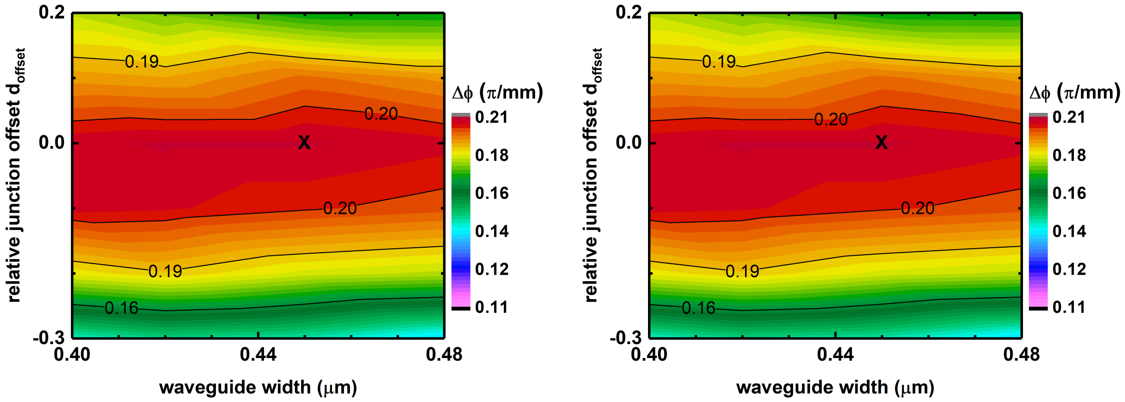

(a) deep etch, $w_{Dop} = 400\,\text{nm}$ **(b)** deep etch, $w_{Dop} = 600\,\text{nm}$

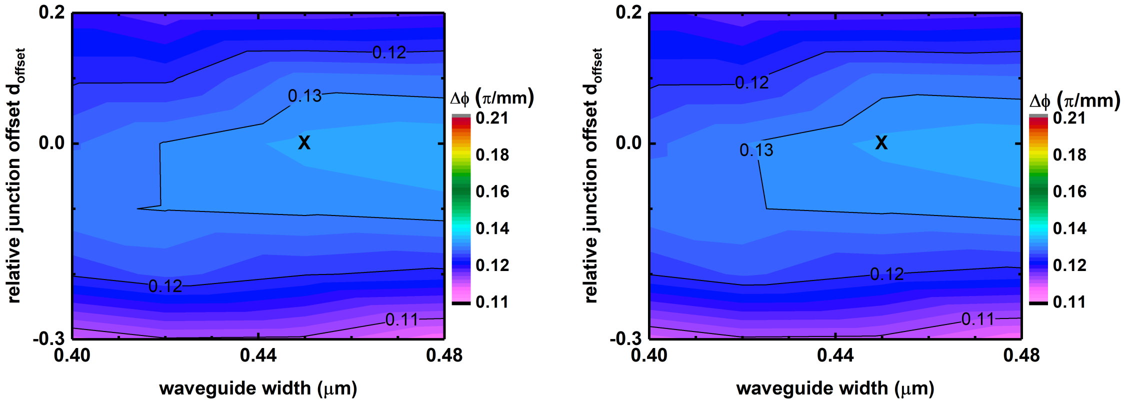

(c) shallow etch, $w_{Dop} = 400\,\text{nm}$ **(d)** shallow etch, $w_{Dop} = 600\,\text{nm}$

Figure 4.4: Simulated phase shifts at $-3\,\text{V}$ as a function of waveguide width and pn-junction offset for phase shifters with nominal doping. The "X" indicates the choice that was made for the designs to be implemented into the final mask layout.

MZMs is very well confined in the waveguide rib. Consequently, the overlap with the depletion region does not significantly change when the waveguide width is varied from 400 nm to 480 nm. In contrast, the phase shift becomes larger for shallow etch MZMs when the waveguide widths increases. For wider shallow etch waveguides, a larger fraction of the optical power is guided in the waveguide rib and the overlap integral with the depletion region therefore enhances.

Figure 4.4 also shows that the simulated phase shift values for the two different widths of the waveguide doping w_{Dop} are virtually the same. This is because the phase shift is determined in the center of the waveguide where the depletion region widens when a reverse voltage is applied. The distance at which the intermediate doping starts thus does not affect the phase shift because it is too far away from the center of the optical mode.

The simulated losses, on the other hand, are affected by w_{Dop} (Fig. 4.6). The

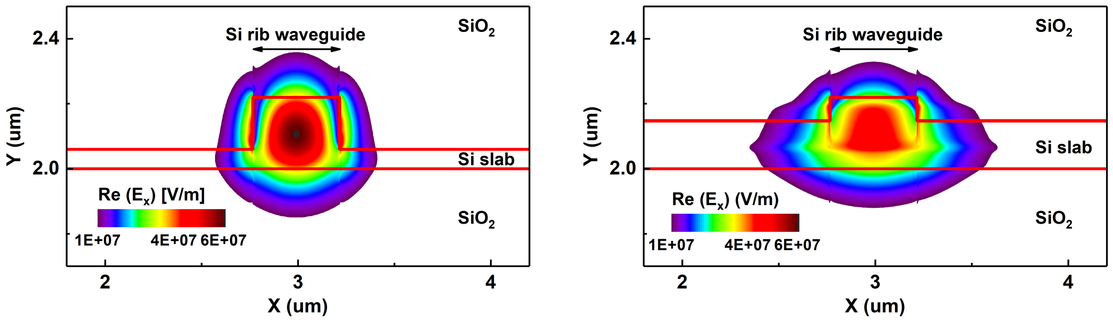

(a) deep etch **(b)** shallow etch

Figure 4.5: Distribution of the electric field of the fundamental TE mode in a deep and shallow etch waveguide. Due to the reduced etch depth, a larger fraction of the mode in a shallow etch waveguide extends into the slab region. The intensity in the rib region is consequently lower than in a deep etch waveguide for the same overall optical power guided in the waveguide.

tails of the optical mode can still interact with the intermediate doping level in the slab. The absorption losses thus increase if the intermediate doping implantation is brought closer to the waveguide rib where most of the light is guided. This holds true for both etch depths but is again more pronounced for shallow etch MZMs because the tail of the optical mode extends further into the slab and interacts more strongly with the intermediate doping levels.

Figure 4.6 further shows that the losses for deep etch MZMs tend to increase when the waveguide becomes wider. This is due to a better confinement of the optical mode in the waveguide rib which results in a stronger absorption of photons in the doped regions therein. In contrast, the optical mode is less confined and a larger fraction of it is guided outside the waveguide rib in the surrounding oxide when the waveguide is narrower. Consequently, the overall absorption is lower. The optical mode in shallow etch MZMs is also less confined when the waveguide is narrower. In contrast to an optical mode in a deep etch MZM, however, this will lead to an enhanced interaction of the optical mode's tail with the intermediate doping regions in the thick slab. Very high losses occur there and the overall losses thus increase. The overall losses decrease when the width of shallow etch waveguides becomes wider. This is because the interaction of the optical mode's tail with the intermediate doping regions is reduced.

The losses for deep etch MZMs are lowest when the relative position of the pn-junction is slightly offset towards the n-doped region ($d_{offset} = -0.1$). In this case, the depletion region maximally overlaps with the peak intensity of the optical mode and the lowest absorption occurs. The losses increase if the pn-junction is further shifted towards the n-doped region because the waveguide rib would then be mostly

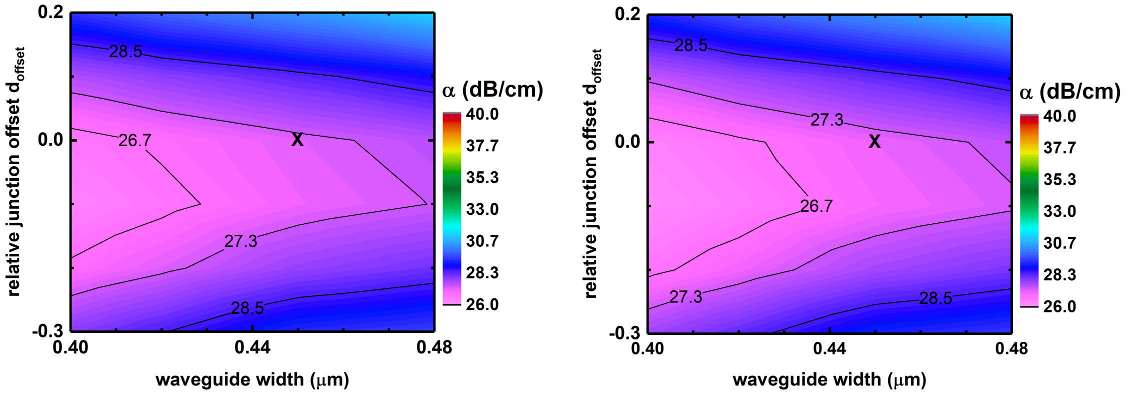

(a) deep etch, $w_{Dop} = 400\,\mathrm{nm}$ **(b)** deep etch, $w_{Dop} = 600\,\mathrm{nm}$

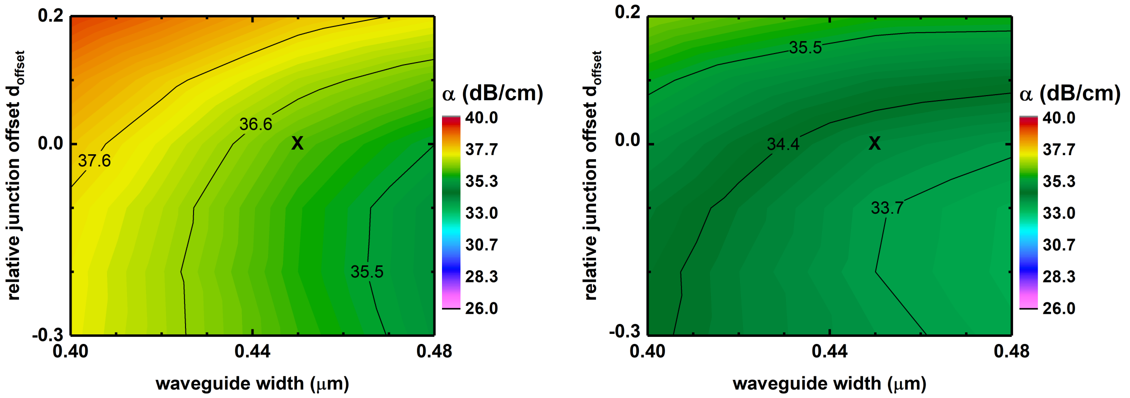

(c) shallow etch, $w_{Dop} = 400\,\mathrm{nm}$ **(d)** shallow etch, $w_{Dop} = 600\,\mathrm{nm}$

Figure 4.6: Simulated loss at 0 V as a function of waveguide width and pn-junction offset for phase shifters with nominal doping. The "X" indicates the choice that was made for the designs to be implemented into the final mask layout.

n-doped and the high density of electrons therein increases the absorption losses, see Eq. (2.13). Inversely, moving the pn-junction towards the p-doped region (negative junction offset) increases the hole density in the waveguide rib and the losses become again larger compared to a pn-junction at $d_{offset} = -0.1$. The results for shallow etch MZMs suggest the same tendency. The lowest losses would occur when the pn-junctions is around $d_{offset} = -0.1$. However, the amount by which the losses increase when the pn-junction is shifted towards either the n- or p-doped side seems to be lower than for deep etch MZMs. Additional simulation results for narrower waveguide widths and over a wider range for d_{offset} would be needed to confirm this trend.

Overall, the simulated losses are comparatively large when compared to published values ranging e. g. from 12 dB/cm [190] to 21 dB/cm [191] because of the high doping concentrations in the waveguide. However, the corresponding phase modulation efficiencies with 1.86 Vcm and 2.4 Vcm for [190] and [191], respectively, are also inferior to a simulated deep etch MZM (1.42 Vcm with $w = 450\,\mathrm{nm}$ and $d = 0\,\mathrm{nm}$).

Combining the above findings, the largest phase shifts were found for a pn-junction centered in a waveguide with a width of 440 nm (deep etch) and 480 nm (shallow etch). The lowest losses could be obtained for narrow deep etch waveguides and wide shallow etch waveguides when the pn-junction was slightly offset towards the n-doped region. Given that the waveguide processing tolerance can be up to 50 nm and waveguides from 500 nm width become multi-mode, a waveguide width of 450 nm was chosen for the actual design for both etch depth. This will ensure that the waveguides will support only the fundamental mode should the actual width become wider during processing. The pn-junction was selected to be centered ($d_{offset} = 0.0$) in the waveguide. Since the width of the waveguide doping w_{Dop} does not significantly affect the simulated phase shift but only the loss, values of 500 nm and 750 nm instead of 400 nm and 600 nm were chosen for the actual design. In this way, the phase shift should remain unchanged whereas the overall losses of the custom-design MZMs should be lower. This facilitates the characterization of the MZMs because of a better optical signal-noise-ratio.

The same simulation approach was carried out for MZMs to be operated at $\lambda = 1310\,\mathrm{nm}$ but is not shown here explicitly. The chosen pn-junction offset was also 0.0 but the waveguide width was selected to be narrower (380 nm) to maintain single-mode operation [77] at this wavelength. All results shown later are based on devices designed for $\lambda = 1550\,\mathrm{nm}$.

4.3 Integration into mask layout

The simulated custom-design deep and shallow etch MZMs with both w_{Dop}-values were integrated into a mask layout along with building block MZMs and other test structures. The final chip layout with a die size of 5 mm × 5 mm is shown in Fig. 4.7. In addition to the four custom-design MZMs for $\lambda = 1550\,\mathrm{nm}$ and two for $\lambda = 1310\,\mathrm{nm}$, the mask layout contains two building block MZMs with traveling wave electrodes and different lengths ($L = 1.0\,\mathrm{mm}$ and 1.5 mm) optimized for operation up to 25 Gb/s, three building block MZMs with interleaved pn-junctions and different lengths ($L = 0.5\,\mathrm{mm}$, 1.0 mm and 1.5 mm) that can be modulated with signals up to 10 Gb/s, a building block ring modulator for test purposes not related to radiation, three building block photodiodes and various passive test structures.

Chips with 2× nominal doping were fabricated based on the same layout with only

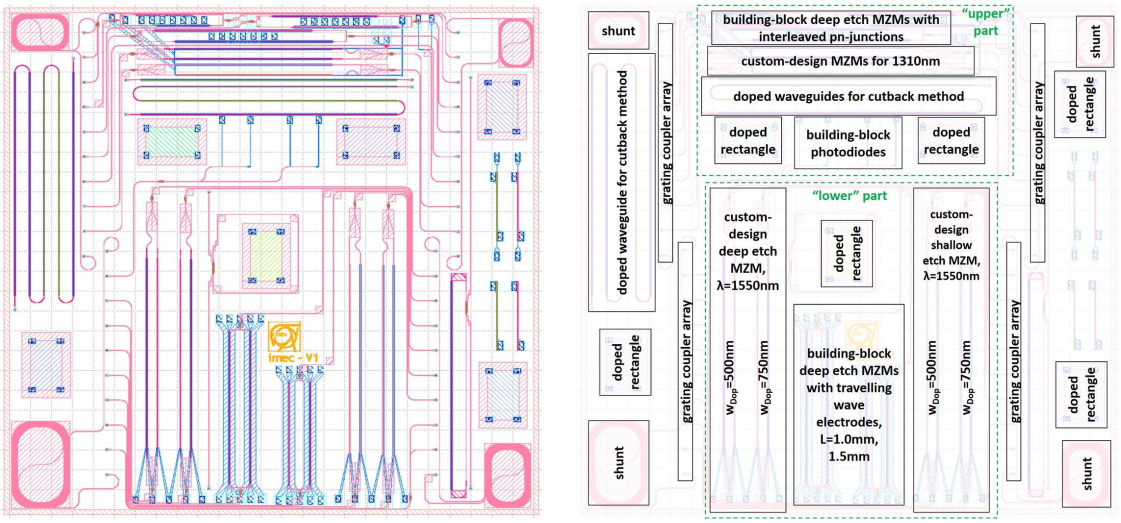

(a) (b)

Figure 4.7: Final mask layout (a) and description (b) of the most important structures on the SiPh test chip.

the implantation step for the n- and p-doping concentration in the waveguide being different.

Building block Multi-Mode Interference (MMI) couplers were used as splitter and combiner (cf. Fig. 2.4) for the custom-design MZMs. Connections to optical fibers can be made through building block grating couplers that were arranged in arrays to facilitate coupling to multiple optical fibers.

The waveguide-connections to these building blocks are strip waveguides, while the MZMs need rib waveguides (cf. Fig. 2.2). The profile of the optical mode between building block components and phase shifters thus needs to be transformed to reduce mode-mismatch and thus coupling losses. Adiabatic tapers were incorporated into the custom-design MZMs between the phase shifters and MMIs for this purpose. The tapers were designed such that, coming from a rib waveguide, the slab is gradually reduced from its initial width to zero over a length of 100 µm (Fig. 4.8). In this way, the mode shape is adiabatically transformed from a strip to a rib waveguide and optical losses are kept to a minimum.

The two arms of the custom-design MZMs were made asymmetric, i.e. the waveguides after the two phase shifters but before the combiner do not have the same length (Fig. 4.9). This introduction of an extra length in one waveguide creates an additional, inherent phase shift which will produce a wavelength-dependent interference pattern at the MZM's output. This facilitates the experimental determination of the actual phase shift when a voltage is applied to a phase shifter. The path

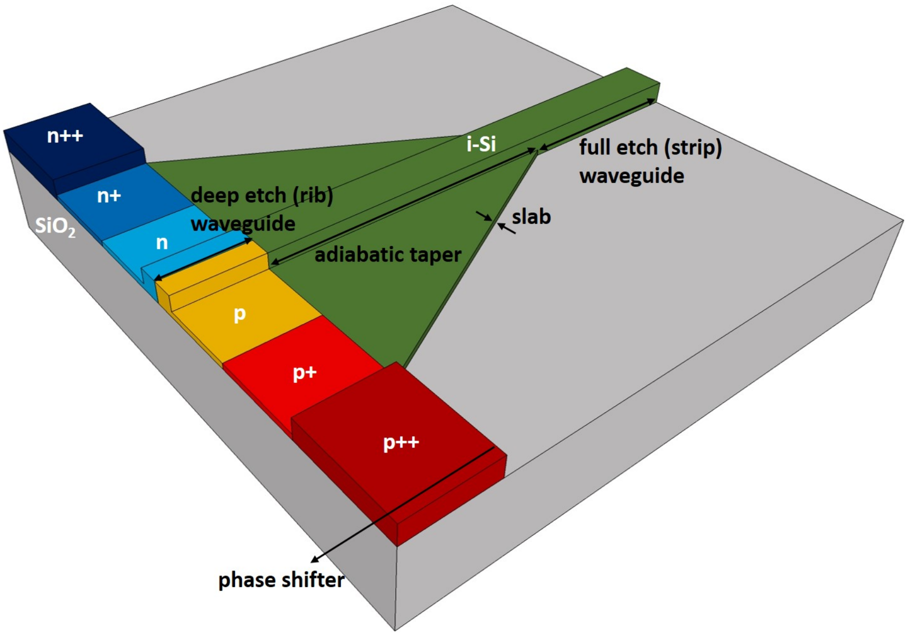

Figure 4.8: Schematic of the adiabatic taper used to transform the optical mode from a deep etch rib waveguide to a strip waveguide by gradually reducing the width of the slab. The position of the tapers before and after the phase shifters is illustrated in Fig. 4.9.

length difference ΔL_{path} was chosen to be 30 µm and together with a simulated group refractive index of $n_g = 4.14314$ for strip waveguides should result in a Free Spectral Range (FSR) of [192]

$$FSR = \frac{\lambda^2}{n_g \Delta L_{path}} = \frac{(1.55\,\mu\mathrm{m})^2}{4.14314 \cdot 30\,\mu\mathrm{m}} = 19.3\,\mathrm{nm}. \tag{4.6}$$

With the goal to put as many different MZMs on the mask layout as possible, compromises with respect to the arrangement of all the bond pads of the individual MZMs had to be made. It was foreseen to attach planar fiber arrays [193, 194] to

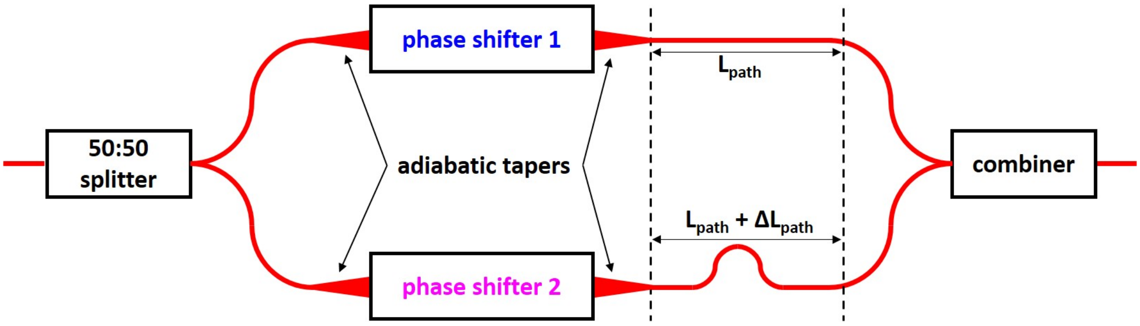

Figure 4.9: Illustration of unbalanced MZM arms, achieved by adding an extra path length ΔL_{path} to one arm. The positions of the adiabatic tapers is also highlighted.

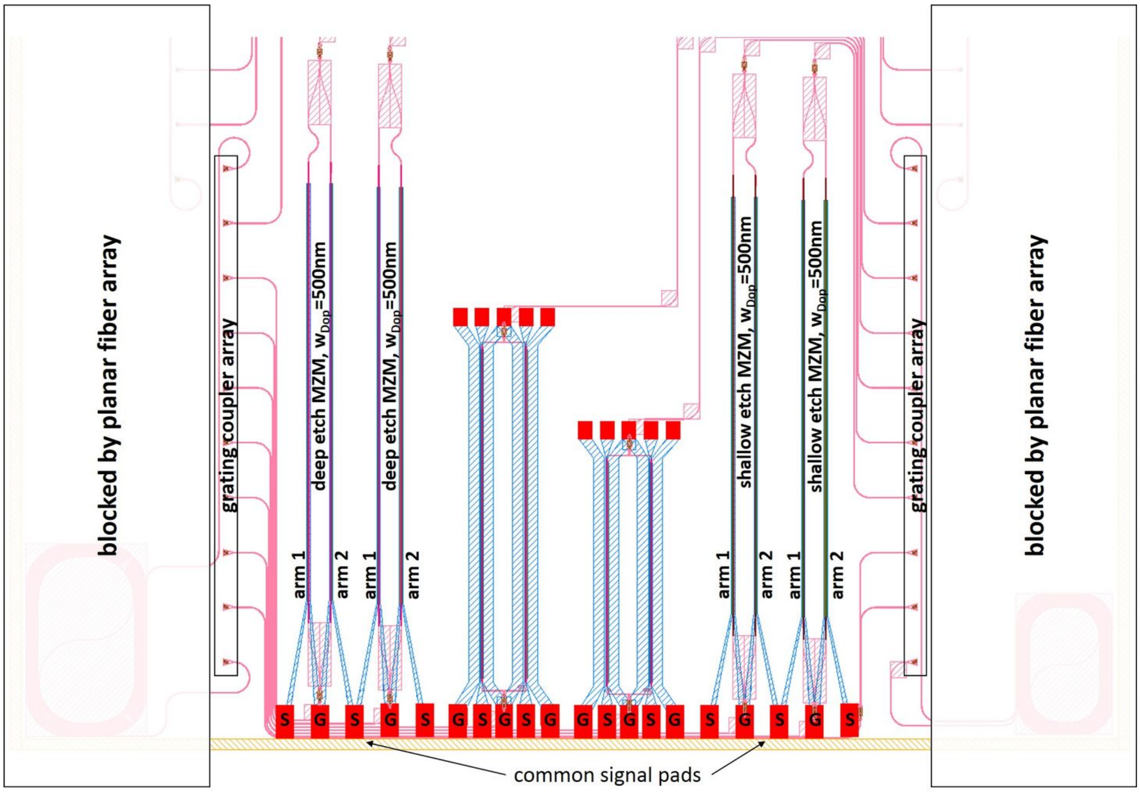

Figure 4.10: Area to the left and right of the grating coupler arrays where no MZMs or bond pads could have been placed because planar fiber arrays would cover that part. A photograph of a sample with planar fiber array is shown in Fig. 5.1. The arrangement of the bond pads on the lower side of the chip is also shown. Due to lack of room, each custom-design MZM has only one ground (G) pad and shares one signal (S) pad with its neighbor. In contrast, the building block devices come with a GSGSG configuration to be able to contact all doped regions individually and to optimize the electrode for high-speed applications.

the grating coupler arrays in order to allow for phase shift measurements during an irradiation test. Therefore, bond pads could not be placed on the left or right side of the chip behind those grating coupler arrays. Otherwise the planar fiber arrays would have covered the bond pads and no electrical connections to the MZMs could have been made (Fig. 4.10). MZMs could not have been placed there either as the planar fiber array would have covered them from radiation. Consequently, the available unblocked width between the grating coupler arrays was not sufficient to place wide enough (80 µm) bond pads with the recommended pitch (150 µm) for all MZMs. A special bond pad arrangement was thus chosen (Fig. 4.10). Each custom-design MZMs has only one ground (G) pad connected to both arms of the modulator. In addition, both custom-design deep etch MZMs as well as both custom-design shallow etch MZMs share a common signal (S) bond pad with their neighbor. In this way, the total count of bond pads could be reduced while the dimensions and spacing of the remaining bond pads comply with the suggestions from the bonding partner. At the same time, it is possible to measure the phase shift of all MZMs properly.

In contrast, current-voltage (IV) measurements on MZM arms that share a common signal pad are not representative of the pn-diode incorporated into these arms. When measuring the IV of an arm that shares the signal pad with another arm, there is a leakage current flowing through the second arm. Consequently, only IV measurements done on an isolated MZM arm can be regarded as fully representative of the true performance.

As a result of this bond pad compromise, the electrodes of the custom-design MZMs were not optimized for high-speed applications either. In detail, there are no traveling wave electrodes, there is no possibility to terminate the custom-design devices electrically and the velocities of optical and electrical RF wave were not matched. This is not a drawback for the purpose of this research since the focus of this chip layout was to test the radiation-hardness of MZMs with different design parameters statically. High-speed applications were of secondary interest at this stage.

Building block PDs are included in the layout so that first results on their radiation-hardness can be measured as well. The building block ring modulator was put on the chip in case some tests with such a device would be required. It is not considered for radiation-hardness evaluations because of its inherent sensitivity to temperature and process variations.

The passive optical test structures on the chip layout included doped and un-doped waveguides with different lengths but the same geometrical design as for the deep etch MZMs. They can be used to determine the waveguide losses via the cutback method [195]. In order to save some real-estate on the die, the un-doped waveguides were used as shunt waveguides to connect the two outermost grating couplers of the arrays together and allow for active alignment of the planar fiber arrays to the grating couplers [196, 197].

Six un-etched, doped silicon regions (one per available doping concentration) are added to the layout to allow for the determination of the actual doping concentrations used in the process. This can be done by measuring the resistivity of those doped regions by means of the Van-der-Pauw-technique [198, Chapter 8] and converting it to a doping concentration.

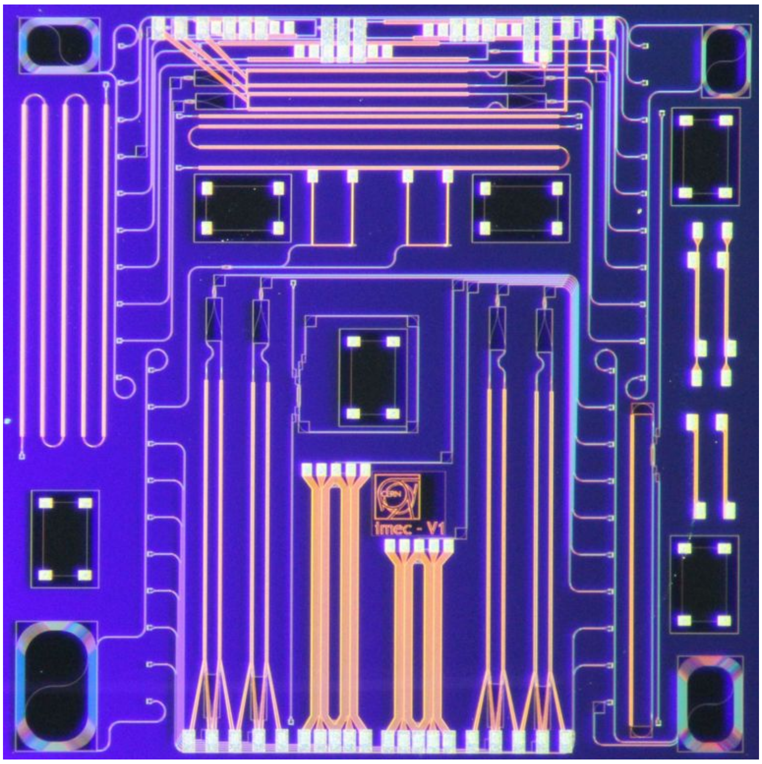

Figure 4.11: Photograph of the fabricated SiPh chip. The corresponding mask layout and an explanation of the different structures are given in Fig. 4.7.

4.4 Functional verification of fabricated chip

The above described mask layout was submitted to imec in January 2015. The fully fabricated chips were received in October 2015. A photograph of such a chip is shown in Fig. 4.11. To verify the functionality of the MZMs and compare the results to the simulations, the phase shifts of the individual MZMs were measured. The setup of the probe station on which all measurements were done manually is schematically shown in Fig. 4.12. A phase shift was induced in an MZM arm by applying a reverse voltage with a *Keithley 2410 SourceMeter* to the phase shifter in the corresponding arm. Light from a broadband Superluminescent Light Emitting Diode (SLED) was coupled through a lensed optical fiber, aligned to the corresponding grating coupler, into the MZM under test. The transmitted light was collected with a second lensed optical fiber and measured with a *Yokogawa AQ6370B* Optical Spectrum Analyzer (OSA). Example spectra of such a measurement are plotted in Fig. 4.13. The plot also shows that the measured FSR of the recorded spectra is 18.9 nm, which is very close to the target value of 19.3 nm.

For the phase shift to be determined, the FSR and wavelength shift $\Delta\lambda$ need to be

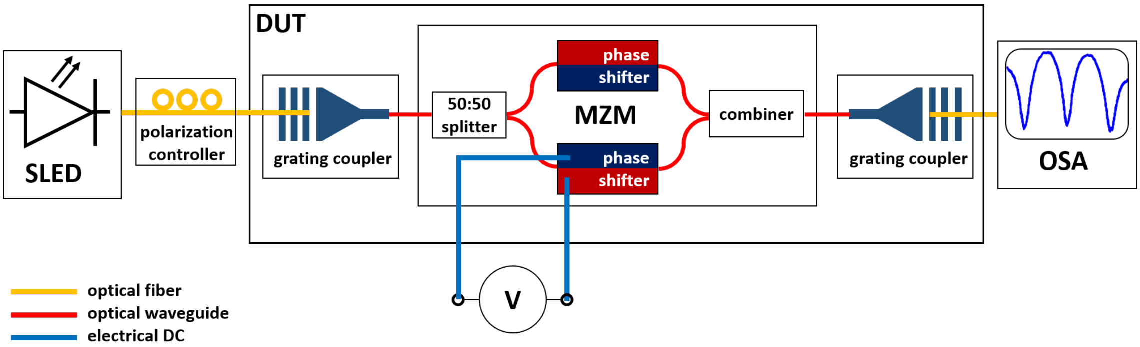

Figure 4.12: Schematic of the test setup to measure the phase shift of MZMs.

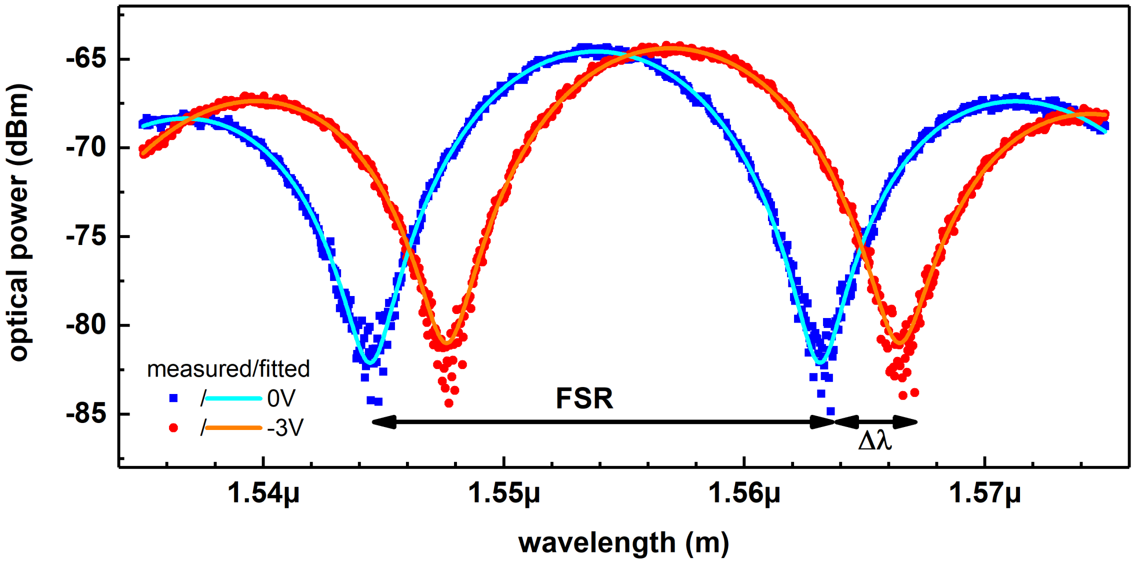

Figure 4.13: Example spectra of a custom-design MZM showing the voltage-induced shift in the transmission as a function of wavelength. The spectra were fitted to Eq. (4.7) in oder to determine FSR and $\Delta\lambda$. The excellent fit confirms the choice of the fitting function. The static extinction ratio determined from the fitted curves is 16.9 dB.

known. Therefore, the spectra were fitted to

$$P_{out} = y_0 + A \exp\left(-\left(\frac{\lambda-\lambda_{env}}{\sigma_{env}}\right)^2\right) \cos^2\left(\frac{(\lambda-\lambda_0)\pi}{FSR}\right), \tag{4.7}$$

with A, λ_{env} and σ_{env} being the amplitude, center wavelength and width, respectively, of a Gaussian-like convolution of the SLED spectrum with the grating couplers' transfer function, y_0 is an offset parameter and λ_0 the position of a transmission minima. With the values from the fit of a spectrum measured at a voltage V_1, the wavelength shift

$$\Delta\lambda = \lambda_0\Big|_{V_1} - \lambda_0\Big|_{0\,\mathrm{V}} \tag{4.8}$$

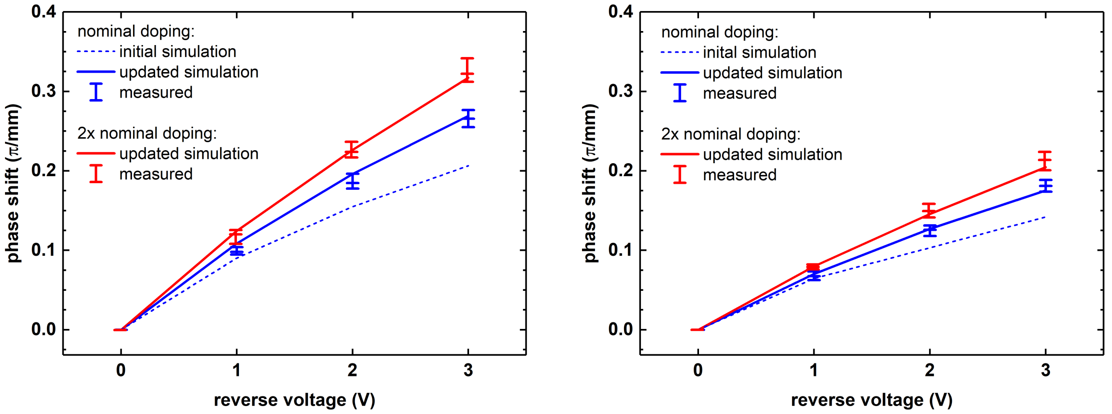

(a) deep etch

(b) shallow etch

Figure 4.14: Comparison of measured and simulated phase shifts for custom-design deep and shallow etch MZMs with both doping levels. The initial simulation shown as dashed lines were done with the expected doping concentrations (same as in Fig. 4.4). After updating the doping concentrations with measured values, the simulated and measured phase shifts agree well. The whiskers indicate the lowest and largest measured phase shift of all tested samples. The corresponding median is also plotted.

could be calculated and the actual phase shift at V_1 with respect to 0 V be determined according to [117]

$$\Delta\phi = \frac{2\pi\Delta\lambda}{FSR}. \tag{4.9}$$

4.4.1 Phase shift

The measured phase shifts for custom-design MZMs were up to 40 % higher than the initially simulated values (Fig. 4.14). A similar conclusion could be drawn for the building block MZMs with traveling wave electrodes. Their measured $V_\pi = 7.7\,\mathrm{V}$ at $-2\,\mathrm{V}$ bias was lower than the expected value of 8.5 V. A lower V_π is equivalent to a larger phase modulation efficiency (cf. Sec. 2.5.1) which typically results from higher doping concentrations when the design of the MZM is otherwise not altered. It was hence concluded that the actual doping concentrations used in the fabrication process were higher than the approximate values that were used for the simulations. Van-der-Pauw resistivity measurements were therefore performed according to [198, Chapter 8]. The obtained resistivity-values were converted to doping concentrations via [199]. The measurements indeed showed that the n- and p-doping concentrations were roughly 20 % larger than the approximate values used for the initial simulations.

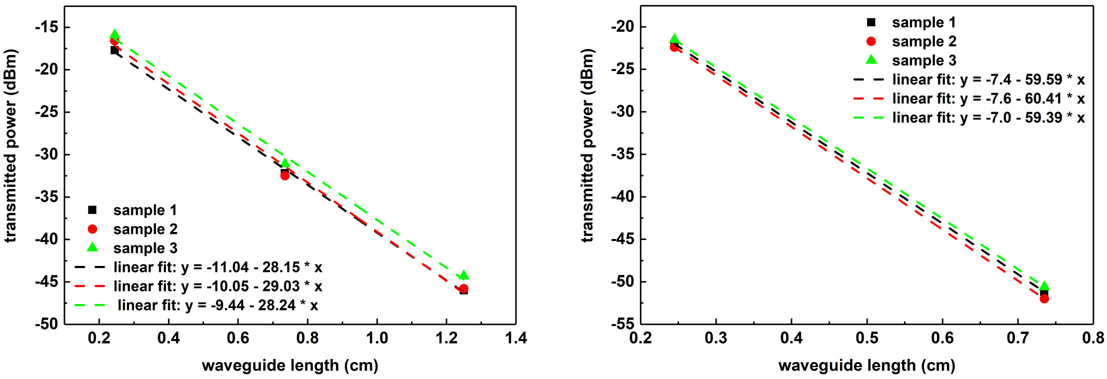

(a) (b)

Figure 4.15: Transmitted optical power through doped deep etch waveguides with different lengths for nominal (a) and 2× nominal (b) doping. The y-intercept of the linear fit gives the insertion loss and the slope the propagation loss of the waveguides.

Based on the measured doping concentrations, the implantation profiles in the simulations were adjusted and the simulations for the MZMs at hand were repeated. A very good agreement between measured and simulated phase shift values could be observed when measured instead of approximated values for the doping concentrations were used (Fig. 4.14). This confirms the validity of the simulation procedure and verifies that the MZMs are fully functional.

4.4.2 Waveguide loss

The losses of the designed deep etch MZMs were assessed by means of the cutback method. The measurement setup was similar to the one shown in Fig. 4.12 except that the SLED was replaced with a 1550 nm-Distributed Feedback (DFB) Laser and the OSA with a *Keithley 81635A* photodiode. The transmitted optical power through waveguides with an identical design as the waveguides in deep etch MZMs are plotted in Fig. 4.15. The data was linearly fitted and the insertion- and propagation loss of the waveguides were determined from the y-intercept and slope, respectively.

The average propagation loss for deep etch waveguides with nominal doping was 28.5 dB/cm. This value is about 2 dB larger than the simulated loss (cf. 4.6). This difference is reasonable given that the approximate values for the doping concentrations used for the initial simulations were lower than the measured values.

The average insertion loss was 10.2 dB. This can be attributed to a grating coupler loss of about 4 dB (cf. Sec. 6.2) and 0.5 dB loss from the lensed fiber [200] on both coupling sides. The remaining 1 dB loss is attributed due to the manual coupling tolerances.

For deep etch waveguides with 2× nominal doping, the propagation loss was so high that the photodiode could not measure the transmitted power through the longest waveguide. Consequently, only two data points were available for a linear fit. Hence, the fit results cannot be regarded as quantitatively representative for the determined losses. This can be seen with the reduced insertion loss which should normally be the same as the one determined for deep etch waveguides with nominal doping. Nonetheless, the fit values for the slope qualitatively indicate that the propagation losses through waveguides with 2× nominal doping are roughly doubled to about 59.8 dB/cm. With this value for the propagation loss and an insertion loss of 10 dB, the expected transmitted power through the longest waveguide can be extrapolated to be −84.8 dBm. This is below the maximum sensitivity (−80 dBm) of the photodiode and hence explains why it was not possible to measure the transmission through the longest deep etch waveguide with 2× nominal doping.

4.5 Summary

MZMs with varied design parameters are required to assess how their radiation-hardness could be improved. Simulations were performed to find MZM designs with the best compromise between phase shift and loss for the process parameters in an imec MPW. Based on the simulations, the width of the waveguide for deep and shallow etch MZMs was chosen to be 450 nm and the position of the pn-junction was centered in this waveguide. Two different widths for the waveguide doping w_{Dop} were selected, 500 nm and 750 nm. MZMs on several dies were characterized after fabrication to verify their functionality. All structures were fully functional. The actual doping concentrations used during fabrication were determined with Van-der-Pauw resistivity measurements and found to be higher than initially expected. After modifying the simulations accordingly, the simulated phase shifts agreed well with the phase shifts that were experimentally determined by fitting transmission spectra of the tested MZMs.

5 Evaluation of radiation-hardness of Mach-Zehnder modulators

The effect of the varied MZM design parameters on their resistance to ionizing radiation was assessed with the fully functional SiPh test chips. Three different x-ray irradiation tests were conducted to identify an MZM design that does not show a significant phase shift degradation up to a TID of at least 1 MGy. Simulations were performed to attempt to reproduce the experimental results and understand why different MZM designs respond differently to radiation. The test procedures and findings of the three x-ray irradiation tests as well as the simulations are presented in this chapter.

5.1 Measurement setup and procedure

All three irradiation tests were done with a *Seifert RP149* x-ray irradiator. X-rays were chosen over γ-radiation for irradiation tests with ionizing radiation because x-ray systems are more convenient to use than ^{60}Co γ-radiation-sources. They typically provide a highly-directed beam which allows for a uniform irradiation of an area on a chip. Radioprotection constraints that are inevitable when working with ^{60}Co can also be avoided when working with x-rays.

The irradiator emits x-rays with a peak energy of 10 keV. This peak energy is not directly related to the actual radiation spectrum as it would occur inside an HEP experiment. Such a radiation spectrum cannot be quantitatively reproduced in any test facility. However, 10 keV is a high enough energy to ionize silicon dioxide and test the resistance of MZMs against ionizing radiation while not creating displacement damage. Additional neutron irradiation tests are typically conducted to investigate the radiation-hardness against displacement damage separately (cf. Sec. 3.1). If candidate devices survive high enough energy levels in both tests, it can be inferred that they will also withstand the same accumulated radiation levels created by the different particles that make up the radiation spectrum inside HEP experiments.

For each irradiation test, one SiPh test chip was placed on a chuck underneath the x-ray tube. The test chip was aligned to the x-ray tube with a laser pointer. The distance between the chip and the x-ray tube was set to 3 cm which resulted in a fairly uniform beam diameter of approximately 3 mm, enough to cover either the upper part of the SiPh chip with the MZMs having interleaved pn-junctions or the lower part with the MZMs having lateral pn-junctions (cf. Fig. 4.7). The voltage and current of the x-ray tube were set to 40 kV and 40 mA, respectively. This led to a dose rate of 14.05 Gy/s for the chosen distance between test chip and x-ray tube [201]. The irradiation time was adjusted for each irradiation step such that the target TID was reached with the above dose rate.

The temperature inside the irradiator and the bias applied to the MZMs on a test chip during irradiation were varied for the three tests. IV curves and phase shifts of both arms of all MZMs on either the upper or lower part of the test chip were measured during the tests.

5.1.1 Stepwise irradiation of bare chips at room temperature

The first irradiation test was done with bare dies that were not wire-bonded or fiber-pigtailed. As a consequence, the samples were not biased or measured while the x-ray source was on. Instead, a stepwise irradiation test where the TID was sequentially increased was performed. All MZMs were manually characterized on a probe station before the test started and after each irradiation step. The setup of the probe station was identical to the one described in Sec. 4.4. Once all measurements were completed after the test chip was exposed to a certain TID, the next irradiation step followed immediately to prevent annealing of any damage created in the MZMs to occur. Measuring an MZM was stopped if a phase shift could no longer be measured for that device. The irradiation test was ended once either all MZMs on a test chip no longer showed a phase shift or when the available period of use for the irradiator was over.

All the measurements and irradiation steps were done at room temperature, i.e. the chuck on which the test chip was placed was not temperature-controlled. A PT100-sensor was used to track the temperature close to the test chip inside the irradiator. Its readings showed that the temperature did not increase by more than 5 °C during irradiation. Temperature effects impacting the performance of the MZMs can thus be neglected.

Four different dies were used for this test:

- one die with nominal doping to test MZMs with lateral pn-junctions on the lower part of the chip,
- one die with 2× nominal doping to test MZMs with lateral pn-junctions on the lower part of the chip,
- one die with nominal doping to test MZMs with interleaved pn-junctions on the upper part of the chip,
- one die with 2× nominal doping to test MZMs with interleaved pn-junctions on the upper part of the chip.

5.1.2 Continuous irradiation and online measurement of packaged chips at room temperature

Wire-bonded and fiber-pigtailed samples that allowed the MZMs to be biased and measured during irradiation were used for the second irradiation test. Not only does such a test configuration resemble more closely an actual system implementation in HEP experiments, it is also possible to determine whether the radiation-hardness of SiPh MZMs changes as a function of bias as it has been observed for CMOS transistors [202].

For that purpose, test chips were glued onto a Printed Circuit Board (PCB) and wire-bonded to it. The test voltages and constant bias during irradiation were applied to the MZMs via a connector on the PCB. Light was coupled in and out of the chip through two planar fiber arrays that were attached above the arrays of grating couplers (cf. Fig. 4.7). The wire-bonding and attachment of the planar fiber arrays was done at Tyndall National Institute [203]. A photograph of a packaged sample and the installation inside the x-ray irradiator is shown in Fig. 5.1.

Optical and electrical switches were used to sequentially measure the individual MZMs on the SiPh test chip. The switches were set such that light was sent through the MZM that was currently being measured and the voltage applied to it for IV- or phase shift measurements could be ramped. All other MZMs that were not being measured were biased at a constant voltage and no light was coupled into them.

The transmitted power of the SLED through the MZMs was also measured during irradiation to estimate by how much the propagation loss changes as a function of

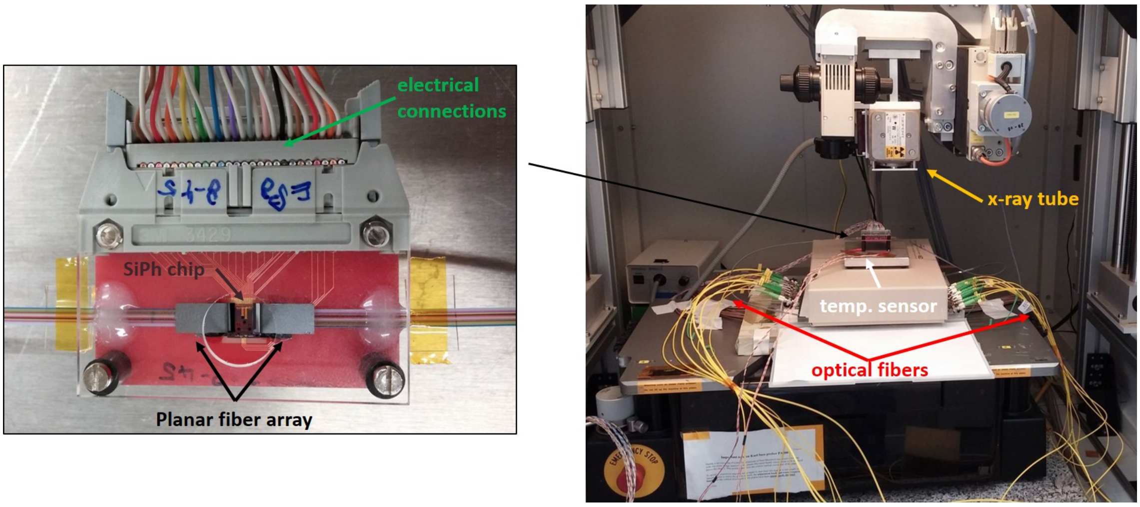

Figure 5.1: Photograph of a packaged sample (left) for the online-irradiation test and the installation of the sample inside the x-ray irradiator (right) before the x-ray tube was aligned to the SiPh test chip.

TID. The losses could not have been determined with the cutback method during irradiation because the planar fiber arrays covered parts of the doped waveguides that would have been needed for this approach.

In contrast to the stepwise irradiation test, all MZMs were measured throughout the entire irradiation test even when they no longer showed a phase shift. The total duration of each irradiation tests varied for each tested die and was between $25 - 72\,\mathrm{h}$, depending on how long the MZMs withstood the x-rays.

Based on the outcomes from the first test, only the lower part of the chip with MZMs having a lateral pn-junction was tested with three different dies:

- one die with nominal doping with the MZMs biased at $-3\,\mathrm{V}$,
- one die with $2\times$ nominal doping with the MZMs biased at $-3\,\mathrm{V}$,
- one die with $2\times$ nominal doping with the MZMs biased at $-1.5\,\mathrm{V}$.

Annealing of the damage after irradiation was also investigated for the third sample. For that purpose, the sample was put in a climatic chamber and heated to $60\,^{\circ}\mathrm{C}$ for $22h$ after the phase shifts of all MZMs on that die were close to zero. $60\,^{\circ}\mathrm{C}$ was chosen for annealing because the epoxy used to attach the planar fiber arrays could not have reliably withstood higher temperatures. After that the same sample was exposed to x-rays a second time. The bias during annealing and the second irradiation step was kept to $-1.5\,\mathrm{V}$.

In addition to MZMs, the dark- and photo-current of two building block PDs on the third die were also monitored. Both PDs were biased at $-1\,\mathrm{V}$ during irradiation and both currents were measured at this voltage. To measure the photo-currents, light from a 1550 nm single-mode laser was coupled via one grating coupler into a 1 × 2-MMI splitter to which the two PDs were connected. This ensured that the same optical power impinged on both PDs. The actual optical power impinging on the PDs could not be precisely determined because of the losses occurring in the grating coupler, MMI and waveguides. Hence, the measured photo-current was not converted to a responsivity. The laser was switched off when the dark-currents were measured and during the idle period when the MZMs were measured. Nonetheless, the measured dark-currents include a small photo-current that is inevitably generated by the x-rays.

This irradiation test was also performed at room temperature without a temperature-controlled chuck. Measurements with a PT100-sensor showed that the temperature close to the tested die was $25 \pm 1\,^{\circ}\mathrm{C}$ throughout the test. The temperature varied less compared to the previous test because a new air conditioning system, that removed the heat from the x-ray irradiator more effectively, was installed in the lab between the two tests taking place.

5.1.3 Stepwise irradiation of bare chips at $-30\,^{\circ}\mathrm{C}$

The third irradiation test was conducted with the chuck cooled down to $-30\,^{\circ}\mathrm{C}$, a temperature similar to the actual temperature inside the innermost regions of HEP experiments. Bare dies were again used for this test as the availability of the x-ray irradiator came on short notice and so it was not possible to arrange for packaged samples. Like for the first irradiation test, bare dies were sequentially irradiated and the MZMs were measured between the irradiation steps.

To minimize the buildup of ice during the test, wet air had to be removed from the inside of the irradiator before the temperature of the chuck could be lowered. Therefore, the chuck was heated to $80\,^{\circ}\mathrm{C}$ for 30 min to enhance evaporation of wet air while the irradiator was simultaneously flushed with dry air. After half an hour passed, the chuck was cooled down while dry air continued to flow into the irradiator during the entire irradiation time.

Six dies with nominal doping were used for this irradiation test. Apart from the TID they were exposed to, the test conditions were the same for all of them. If a single die was used and sequentially irradiated for this test, heating up the chuck before it was cooled down could have caused annealing of damage created during the previous irradiation step. This would have made a direct comparison of the measurement results to the ones from the other two tests impossible. Thus, to keep the test conditions as similar as possible, different dies were used for each irradiation step. For instance, the first die was exposed from 0 kGy to 200 kGy, the second die from 0 kGy to 300 kGy, the third die from 0 kGy to 450 kGy, etc. In this way, the dies were only heated once before the irradiation started.

The pre-irradiation phase shifts from the MZMs on all the different dies showed a good uniformity. The values did not vary more than 10 % (cf. Fig. 4.14). This allowed a direct comparison of the phase shifts from the different dies after irradiation with each other without impairing the validity of the test.

5.2 Measurement results

The results from the three irradiation tests are presented in the following figures. IV curves measured during the three tests are analyzed to check whether first trends of how the design parameters of MZMs affect their radiation-hardness can be recognized. Measured phase shift values as a function of TID for the different test conditions are subsequently assessed.

5.2.1 Current-voltage characteristics under irradiation

The voltage applied to the phase shifters was swept from 1 V to -3 V and the corresponding current recorded. The absolute current values as a function of applied voltage for custom-design MZMs with nominal doping from all three irradiation tests are plotted in Fig. 5.2. IV results from MZMs with 2× nominal doping followed the same trend and are thus not shown explicitly.

It can generally be noted that the leakage currents of packaged MZMs (Fig. 5.2b & 5.2e) were a few nA higher than the leakage currents of MZMs on bare dies. A potential cause could be a photo-current created by the ionizing radiation that was only measured with the packaged samples used for the online irradiation test. Assuming the photo-current I_{ph} scales linearly with the absorbed x-ray power P_x and otherwise depends only on the ionization energy E_{ion} of silicon [52], it can be approximated by

$$I_{ph} = \frac{eP_x}{E_{ion}}. \tag{5.1}$$

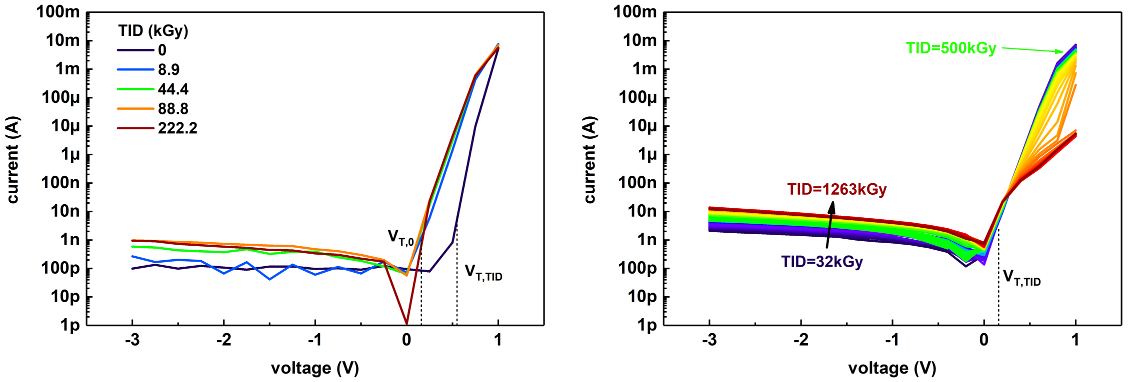

(a) deep etch, ≈ 25 °C,un-biased, bare die **(b)** deep etch, ≈ 25 °C,biased, packaged

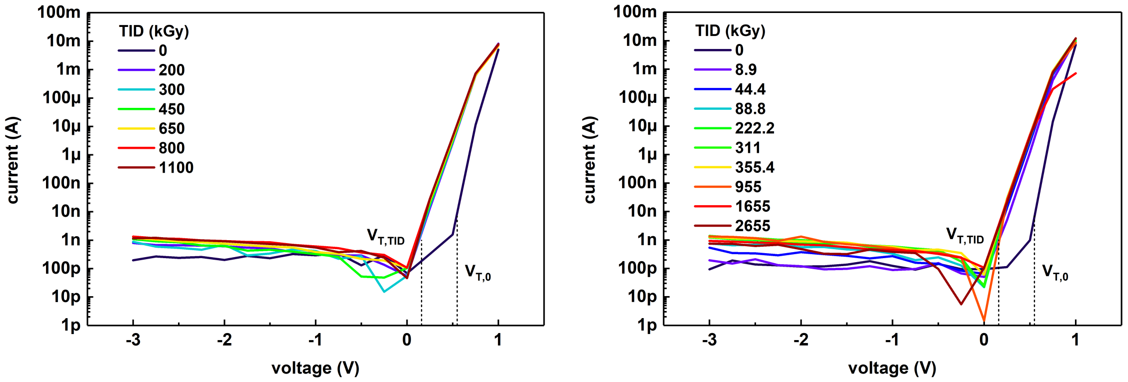

(c) deep etch, −30 °C,un-biased, bare die **(d)** shallow etch, ≈ 25 °C,un-biased, bare die

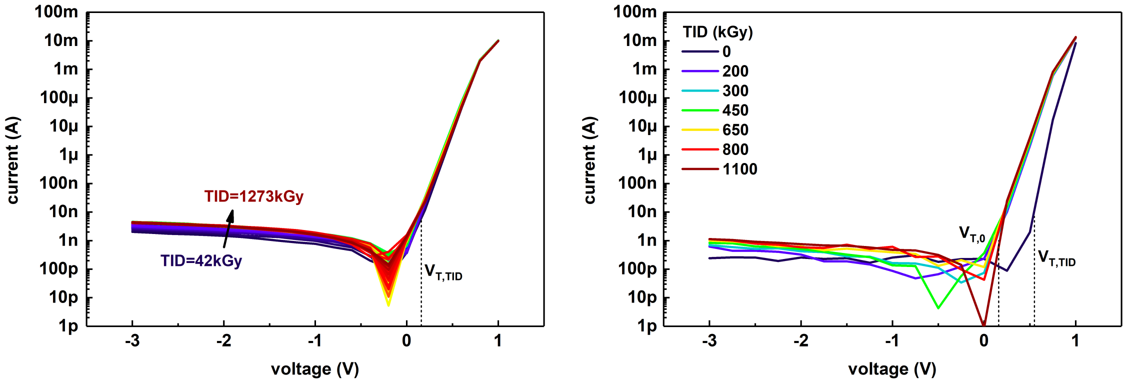

(e) shallow etch, ≈ 25 °C,biased, packaged **(f)** shallow etch, −30 °C,un-biased, bare die

Figure 5.2: Measured IV curves for custom-design MZMs with nominal doping from all three irradiation tests. The bias during irradiation for the packaged samples was −3 V. The forward turn-on voltages before ($V_{T,0}$) and after irradiation ($V_{T,TID}$) shift towards zero due to the radiation.

Silicon's ionization energy is 3.6 eV $= 5.77 \cdot 10^{-19}$ J [138]. The absorbed x-ray power is given by the dose rate $\dot{D}$ multiplied with the volume V_{Si} and density ρ of the silicon in the depletion zone of the phase shifter,

$$P_x = \dot{D} \cdot \rho \cdot V_{Si} = \dot{D} \cdot \rho \cdot L \cdot h_{Si} \cdot W_D. \tag{5.2}$$

The height of the depletion zone is $h_{Si} = 220\,\mathrm{nm}$ and the width of the depletion zone W_D can be calculated with help of Eq. (4.1) and (4.2),

$$W_D = W_n + W_p = \sqrt{\frac{2\varepsilon_0\varepsilon_r}{e}\frac{N_A + N_D}{N_A N_D}(\Psi_{bi} - V)}. \tag{5.3}$$

The resulting photo-current is smaller than 1 pA for the MZMs at hand. This is negligible compared to the measured values and thus cannot be the reason for the higher leakage currents. Since this behavior was only observed for packaged samples, it is assumed that the wire-bonding procedure or the soldering of the electrical connector to the PCB probably created additional leakage paths that led to increased leakage currents.

Comparing all plots, the measurements clearly demonstrate that reverse leakage currents for all tested MZMs increased by roughly ten-fold compared to their pre-irradiation values. This increase is from about 100 pA to 1 nA for bare dies and approximately from 1 nA to 7 nA for packaged samples. This can most likely be attributed to positive trapped charge in the oxide and interface traps which were created as a consequence of the radiation. The former can inverse the p-doped region in silicon near the interface to the oxide and give rise to conductive paths [204, 205] which in turn enhance the leakage currents. Interface traps on the other hand can directly lead to leakage currents [206].

While there is only a small difference in the measured leakage currents between deep and shallow etch MZMs that were stepwise irradiated (Fig. 5.2a & 5.2d and Fig. 5.2c & 5.2f), the increase in leakage current for deep etch MZMs that were measured online (Fig. 5.2b) is higher than for online-measured shallow etch MZMs (Fig. 5.2e). This is an indication that deep etch MZMs were more strongly affected by ionizing radiation than shallow etch MZMs. The same observation could have probably been made during the stepwise irradiation test at room temperature as well if measuring deep etch MZMs was not stopped once their phase shift vanished.

Another feature that was only observed during the online irradiation test in deep etch MZMs is the decrease in forward current at 1 V. The current decreased from roughly 10 mA to below 10 µA for TID levels above 500 kGy (Fig. 5.2b). This can be interpreted as an increase in the resistance of the current path. Reduced free carrier densities in the semiconductor typically give rise to an increased resistance. This reduction could be caused for example through hydrogen-induced dopant passivation (cf. Sec. 3.3) or free holes in the p-doped silicon being pushed away by the positive trapped charges in the oxide. Shallow etch MZMs did not exhibit this behavior. This again indicates that they were less affected by ionizing radiation than their deep etch counterparts.

No significant difference in the IV curves between deep and shallow etch MZMs was measured during the irradiation test at $-30\,^{\circ}\mathrm{C}$ (Fig. 5.2c, 5.2f), even though MZMs with both etch depths were exposed to almost the same TID level as during the online irradiation test. An explanation for this could be that the hole mobility in oxide is approximately two orders of magnitude lower at $-30\,^{\circ}\mathrm{C}$ than at room temperature [207]. Radiation-induced holes thus move slower through the oxide and the buildup of defects is delayed. Similar to transistors [208], it can be inferred that the radiation-hardness of SiPh MZMs in a cold environment is better than at higher temperatures.

The IV curves in Fig. 5.2 also show a shift in the forward turn-on voltage from $V_{T,0} \approx 0.6\,\mathrm{V}$ before irradiation to $V_{T,TID} \approx 0.1\,\mathrm{V}$ when the first measurements after exposure to x-rays were taken. This apparent turn-on voltage reduction can likely be associated with radiation-induced leakage paths in the device. At positive voltages lower than V_T before irradiation, the pn-junction was not yet turned on and there was only a small forward-current through the pn-junction due to drift and diffusion. Once leakage paths were created by radiation, a current larger than that small forward-current could flow through these leakage paths. Macroscopically, it looks like the pn-junction was already turned on even though the turn-on voltage of the pn-junction itself probably did not change.

5.2.2 Phase shift results from stepwise irradiation test at room temperature with un-biased samples

The measured phase shifts as a function of TID for custom-design MZMs are plotted in Fig. 5.3. The results confirm the indications found from the IV measurements. Shallow etch MZMs could resist to higher TID levels than deep etch MZMs. This applies for MZMs with both doping concentrations and waveguide doping widths w_{Dop}. The latter parameter virtually did not affect the phase shift degradation. This is most likely because the intermediate doping implantations were too far away

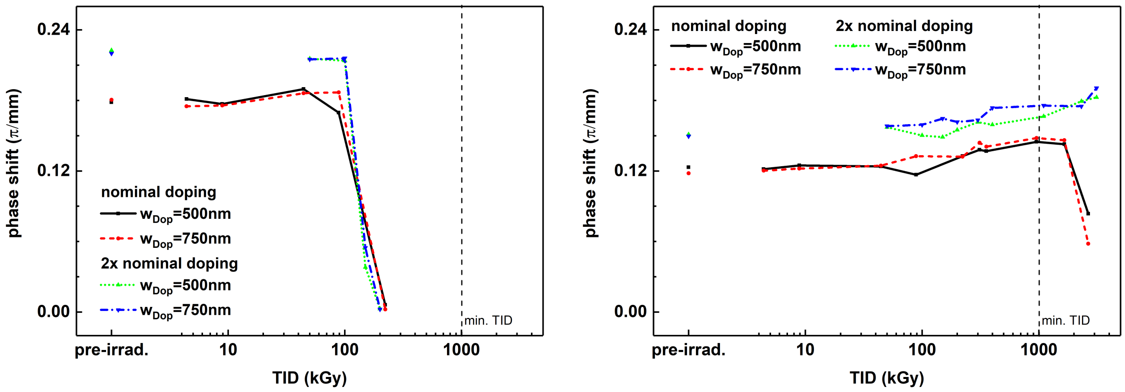

(a) deep etch **(b)** shallow etch

Figure 5.3: Phase shifts of custom-design MZMs from the stepwise irradiation test at room temperature. The phase shifts were measured at $-2\,\mathrm{V}$. The vertical dashed line indicates the minimum TID level SiPh MZMs should be able to withstand.

from the rib region (cf. Fig. 4.1) to accelerate or delay the degradation.

Deep etch MZMs showed a small phase shift enhancement (6 %) up to about 90 kGy before their phase shift rapidly dropped and completely vanished around 200 kGy (Fig. 5.3a). They degraded about 5× faster than the MZMs based on a conventional design (cf. Fig. 1.7). The phase shift of shallow etch MZMs with nominal doping enhanced gradually to 17 % during irradiation up to 1.7 MGy before it then steeply declined. However, the phase shift did not fall below its pre-irradiation value until 1.96 MGy and below 67 % at 2.66 MGy (Fig. 5.3b). This is an improvement of greater than 5× compared to the initial tests that were carried out with the MZMs based on a conventional design.

The radiation-hardness of the MZMs based on a conventional design lies between those of the custom-design deep and shallow etch MZMs. All measurement results are in line with each other because the MZMs with conventional design can be classified as a medium etch MZMs. It can be concluded that the radiation-hardness of SiPh MZMs benefits from a more shallow etch depth. This confirms the findings from [182] that shallow etch MZMs can resist to higher TID levels than deep etch MZMs. The model proposed in [182] suggests that the trapped positive charge in the oxide and the interface traps push the free holes in the p-doped slab away until the carriers in the rib are eventually pinched-off from the contact (Fig. 5.4). In this case, carriers can no longer be depleted from the pn-junction in the center of the waveguide when a voltage is applied because the resistance of the p-doped slab is too high. Consequently, a phase shift can no longer be generated. This effect can be delayed in MZMs with a shallower etch depth, or conversely a thicker slab, since

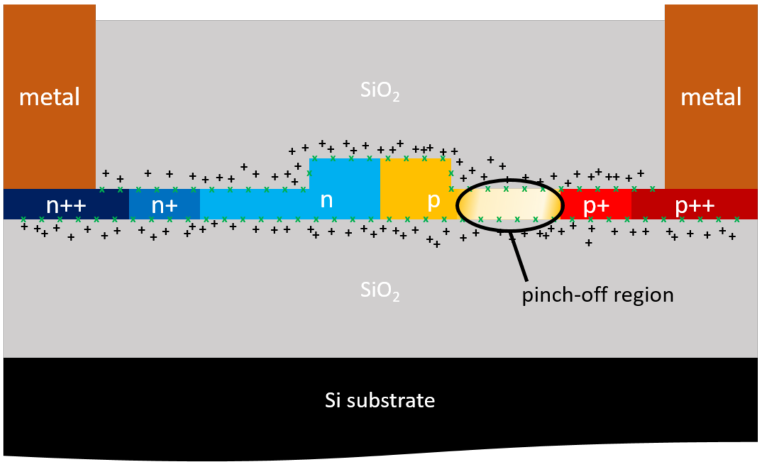

Figure 5.4: Schematic of the pinch-off of carriers in the rib from the slab. Positive trapped charge (+) and interface traps (x) built up due to ionizing radiation and accumulate predominantly along the interface of the device. The positively charged defects push the free holes in the p-doped slab away to the left and right until the concentration of free holes is so low (indicated by the light yellow region) that the conductive path to the p-doped side in the rib is pinched-off. Carriers can no longer be depleted from the pn-junction and the phase shift vanishes.

it contains more free holes and it would take longer to create a pinch-off.

MZMs with 2× nominal doping showed a similar behavior. The phase shift of deep etch MZMs first enhanced (9 %) until approximately 100 kGy. Then the phase shift quickly dropped to zero around 200 kGy (Fig. 5.3a). Shallow etch MZMs showed no degradation but a constant increase (27 %) in phase shift up to 3.1 MGy (Fig. 5.3b).

The reason why a higher doping concentration did not significantly improve the radiation-hardness of deep etch MZMs can probably be attributed to the profile of the p-doping implantation used in imec's MPW. The peak of this implantation lies outside the slab for deep etch MZMs but inside the slab for shallow etch MZMs (Fig. 5.5). The absolute number of additional carriers in a thick slab with 2× nominal doping is therefore significantly larger than in a thin slab compared to MZMs with nominal doping. The pinch-off in shallow etch MZMs with 2× nominal doping thus happened later than in their counterparts with nominal doping, whereas this is not the case for deep etch MZMs with thin slabs.

The results from the irradiation test of building block MZMs with interleaved pn-junctions are shown in Fig. 5.6. Despite having the same etch depth, MZMs with interleaved pn-junction degraded faster than custom-design deep etch MZM with lateral pn-junction. Independent of the doping concentration and the length of the

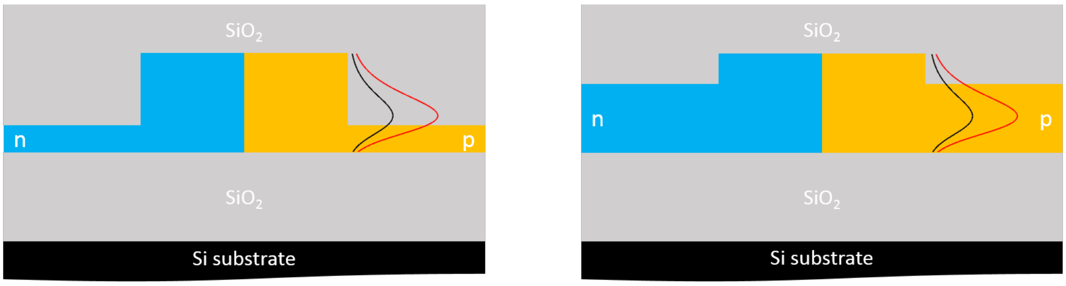

(a) deep etch **(b)** shallow etch

Figure 5.5: Comparison of the shapes of the p-type doping implantations in a deep and shallow etch MZM. The number of additional free holes in a thin slab (as in deep etch MZMs) is much smaller than in a thick slab (as in shallow etch MZMs) when the doping concentration is increased from nominal (black) to 2× nominal (red) doping because the peak of the implantation lies outside the deep etch slab.

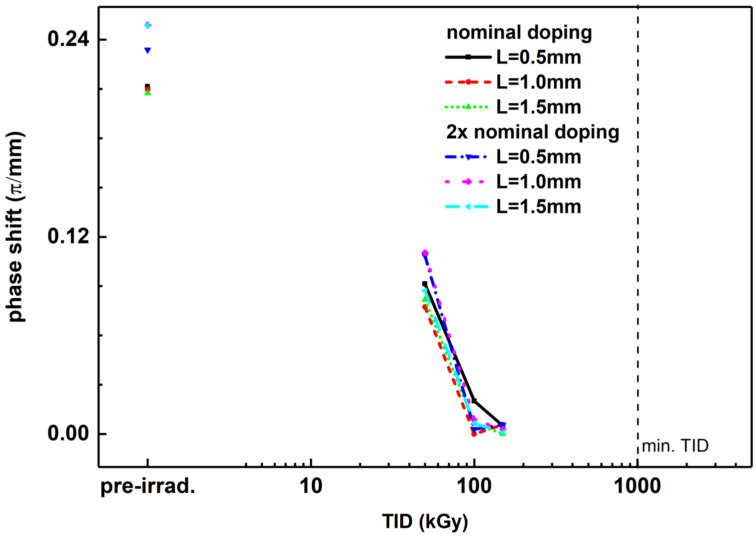

Figure 5.6: Phase shifts of building block MZMs with interleaved pn-junctions from the stepwise irradiation test at room temperature. The phase shift was measured at −2 V.

tested MZMs, the measured phase shifts fell to 50 % of their pre-irradiation values at 50 kGy and completely disappeared at 100 kGy. It is assumed that the faster degradation was due to the un-doped regions in-between the p-doped fingers (see Fig. 4.2) of the interleaved pn-junctions. If positively charged defects accumulate on the p-doped side of the phase shifter, free holes in the slab cannot only be pushed away laterally as in the custom-design MZMs but also longitudinally towards these un-doped regions (Fig. 5.7). The pinch-off effect can thus be more efficient and happens at lower TID levels.

Based on the result that the length of MZMs with interleaved pn-junctions does not

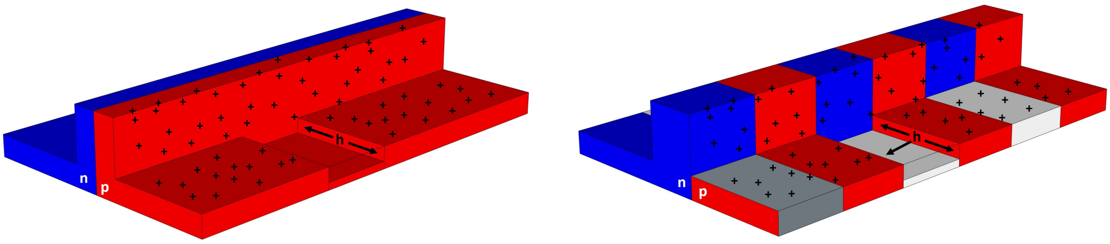

(a) lateral pn-junction **(b)** interleaved pn-junctions

Figure 5.7: Comparison of the pinch-off effect in MZMs with lateral (a) and interleaved pn-junctions (b). Trapped positive charge (+) pushes free holes (h) away laterally towards the rib and contact in MZMs with lateral pn-junctions. For interleaved pn-junctions, free holes can also be pushed away longitudinally towards the un-doped regions. This extra degree of freedom for the direction of motion of holes enhances the phase shift degradation.

affect their radiation-hardness, one can infer that this is also the case for MZMs with lateral pn-junction being uniform along the z-direction. This was confirmed by means of measuring the phase shift degradation of deep etch building block MZMs with two different lengths (1.0 mm and 1.5 mm). The phase shifts of these devices degrade exactly the same as for the deep etch custom-design MZMs for both tested lengths and is thus not explicitly shown.

5.2.3 Phase shift results from online irradiation test at room temperature with biased samples

The results from the online test with samples that were biased during irradiation are qualitatively the same as the ones obtained during the stepwise irradiation test with un-biased samples. MZMs with higher doping concentrations and thicker slabs can withstand higher levels of ionizing radiation than MZMs with other design parameters (Fig. 5.8). Quantitatively, however, MZMs started to degrade already at lower TID levels when biased. The phase shift of deep etch MZMs increased between 6 % and 15 % before it dropped below 50 % of the pre-irradiation value at 43 kGy and 75 kGy for devices with nominal and 2× nominal doping, respectively. The phase shift disappeared between 100 kGy and 110 kGy (Fig. 5.8a). For shallow etch MZMs with nominal doping (Fig. 5.8b), a phase shift enhancement of roughly 30 % could be measured before the phase shift went below 50 % at 738 kGy ($w_{Dop} =$ 500 nm) and 914 kGy ($w_{Dop} =$ 750 nm). Neither of these two shallow etch MZMs showed a phase shift after 1250 kGy ($w_{Dop} =$ 500 nm) and 1560 kGy ($w_{Dop} =$ 750 nm, extrapolated). The increase in phase shift for shallow etch MZMs with 2× nominal doping was limited to $3 - 9$ %. However, the same devices withstood to 1.3 MGy

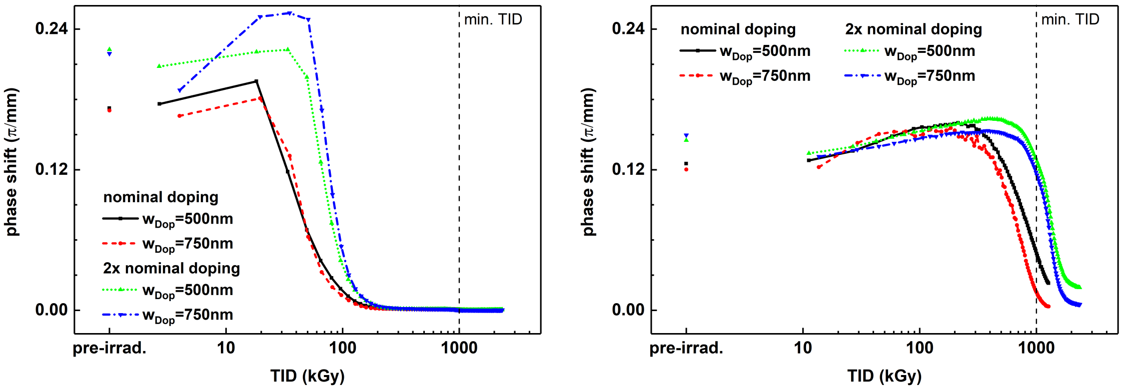

(a) deep etch **(b)** shallow etch

Figure 5.8: Phase shifts of custom-design MZMs from the online irradiation test at room temperature. The phase shifts were measured at −2 V and the samples were biased at −3 V during the irradiation.

without degrading below 50 % of their pre-irradiation values. Their phase shift entirely vanished after 1800 kGy for MZMs with $w_{Dop} = 750$ nm, while MZMs with $w_{Dop} = 500$ nm still showed a small phase shift at 2353 kGy. Since there is no clear tendency whether a smaller or larger value for the waveguide doping width w_{Dop} is better with respect to radiation-hardness, the measured variations are attributed to differences in the individual MZMs due to fabrication tolerances.

The observed enhancement and the general progression of the phase shift as a function of TID is essentially identical for the stepwise irradiation test with un-biased samples and the online irradiation test with biased samples. This implies that the reason for the accelerated degradation is only due to biasing the MZMs during irradiation. Comparing the evolution of the phase shift as a function of TID for MZMs that were un-biased as well as biased at −1.5 V and −3 V confirms this inference (Fig. 5.9). The phase shift degraded slower at −1.5 V than at −3 V, while no bias during irradiation caused the device to withstand the longest. This observation has also been made for CMOS transistors [202] and underlies the similarity regarding radiation-hardness between SiPh and classical CMOS devices.

The origin for the accelerated degradation is most likely due to a stronger electric field in the device when it is reverse biased. The maximum electric field E_{max} at the transition between n- and p-doped regions is given by [186, p. 82]

$$E_{max} = \frac{eN_D W_n}{\varepsilon_0 \varepsilon_r} = \frac{eN_A W_p}{\varepsilon_0 \varepsilon_r}. \tag{5.4}$$

According to Eqns. (4.1) and (4.2), the depletion widths W_n and W_p in the n- and p-doped regions, respectively, become wider for larger reverse biases and the electric

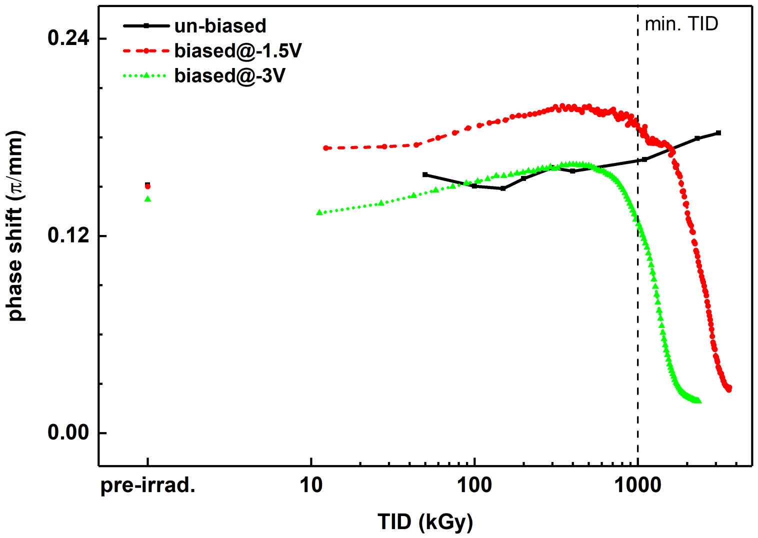

Figure 5.9: Phase shifts of a shallow etch MZM with 2× nominal doping concentration and w_{Dop} = 500 nm measured during irradiation tests with different bias conditions. The phase shift was measured at −2 V. It can clearly be seen that larger reverse biases accelerate the phase shift degradation.

field strength increases. The probability that ehps escape initial recombination then also increases as given by the yield-function in Eq. (3.3). Consequently, the rate at which radiation-generated holes are trapped in deep traps or trigger the generation of interface traps and hydrogenation is enhanced for MZMs that are reverse-biased during irradiation. A stronger electric field E in reverse-biased MZMs also leads to higher carrier drift velocities v_d that scale linearly with the hole mobility μ_h,

$$v_d = E\mu_h. \tag{5.5}$$

This means that holes can move more rapidly through the oxide [209] towards silicon and induce damage there. Consequently, the phase shift in MZMs degrades faster.

5.2.4 Changes in waveguide propagation loss during the online irradiation test at room temperature with biased samples

The change in propagation loss through the MZMs as a function of TID was assessed by measuring the transmitted optical power through the MZMs during the online irradiation. The results for samples that were biased at −3 V during irradiation are plotted in Fig. 5.10. The transmitted power increased with TID for all samples, i.e. the propagation loss through the MZMs decreased. This can be attributed to

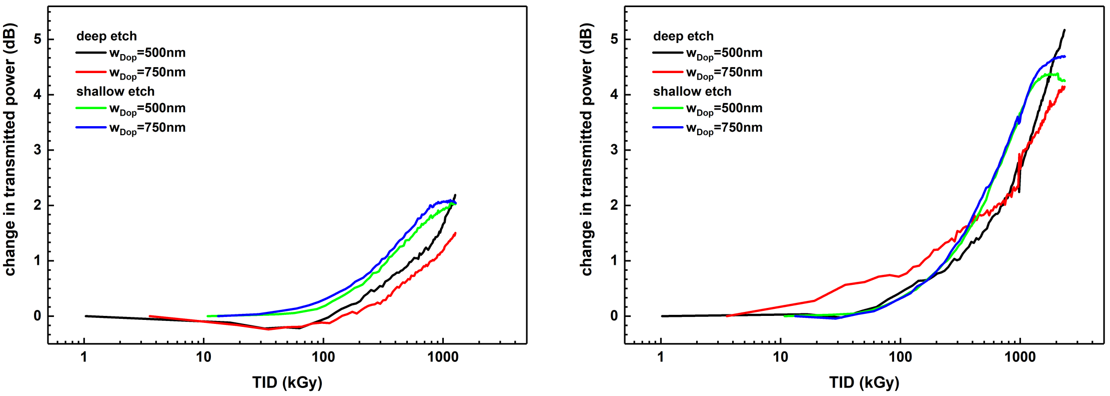

(a) nominal doping **(b)** 2× nominal doping

Figure 5.10: Change in transmitted power through MZMs as a function of TID. The samples were biased at $-3\,\mathrm{V}$ during irradiation.

the pinch-off effect. The reduced density of free holes in the p-doped slab leads to a lower absorption of photons.

The change for MZMs with nominal doping is about 1.4 dB and 2.1 dB at 1 MGy for deep and shallow etch devices, respectively. The change is larger for shallow etch MZMs because a larger fraction of the optical mode is guided in the slab where the pinch-off occurs. The change in transmission at 1 MGy for MZMs with 2× nominal doping is approximately 2.7 dB for deep etch devices and 3.6 dB for shallow etch devices. These numbers are larger than for MZMs with nominal doping because more holes can be pushed out of the p-doped slab in MZMs with 2× nominal doping.

Considering that the measured changes in transmission occurred over a MZM-length of 1.9 mm, the propagation losses of deep etch MZMs after 1 MGy can be estimated based on the measured propagation losses as determined in Sec. 4.4.2. The pre-irradiation propagation losses were 28.5 dB/cm and 59.8 dB/cm for deep etch MZMs with nominal and 2× nominal doping, respectively. With the above mentioned increased transmissions of 1.4 dB and 2.7 dB, the propagation losses after 1 MGy can be estimated to be 21.1 dB/cm for deep etch MZMs with nominal doping and 45.8 dB/cm for deep etch MZMs with 2× nominal doping.

5.2.5 Annealing in Mach-Zehnder modulators after irradiation

The sample that was irradiated at a bias of $-1.5\,\mathrm{V}$ was annealed at 60 °C in a climate chamber after the phase shift of all MZMs went to zero. After a 22 h-anneal, the sample was exposed to x-rays again. The outcomes from this test are shown in Fig. 5.11. The results clearly display that deep and shallow etch MZMs not only

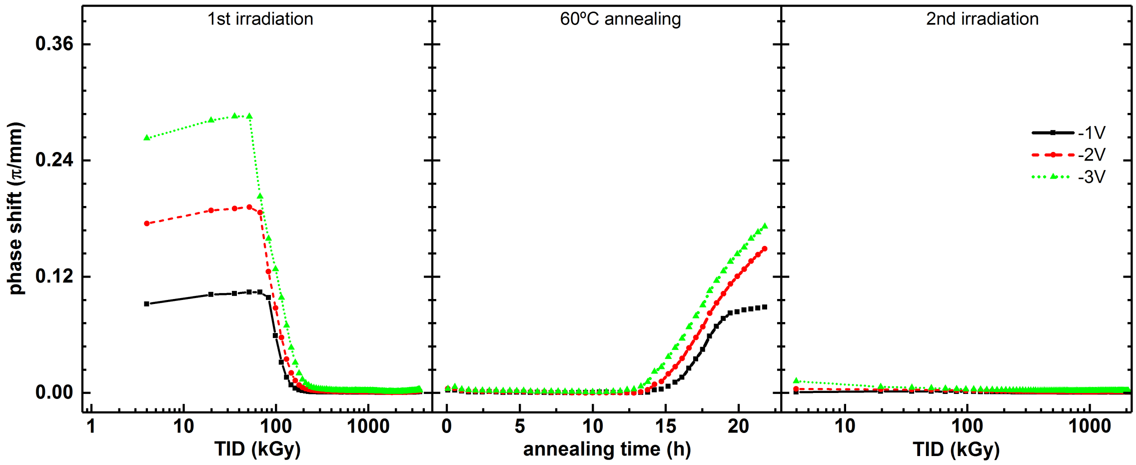

(a) deep etch

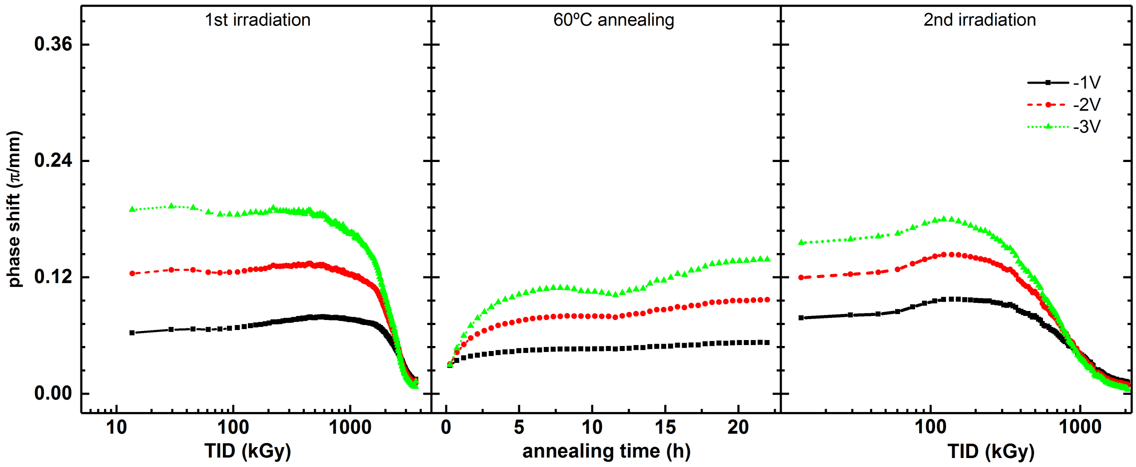

(b) shallow etch

Figure 5.11: Phase shifts of custom-design MZMs with 2× nominal doping and $w_{Dop} = 750\,\mathrm{nm}$ that were first irradiated, then annealed for 22 h at 60 °C and finally irradiated again. The bias during all three steps was $-1.5\,\mathrm{V}$.

withstand to different levels of ionizing radiation but also anneal differently. Shallow etch MZMs started to anneal immediately after the irradiation ceased. They recovered $70 - 80\,\%$ of their pre-irradiation phase shift during the annealing, depending on the applied bias. They survived another 604 kGy ($-3\,\mathrm{V}$), 791 kGy ($-2\,\mathrm{V}$) and 1173 kGy ($-1\,\mathrm{V}$) before the phase shift fell again below 50 % during a second irradiation. The accumulated TID levels for both irradiation steps were 2646 kGy ($-3\,\mathrm{V}$), 3141 kGy ($-2\,\mathrm{V}$) and 4002 kGy ($-1\,\mathrm{V}$). On the other hand, deep etch MZMs only started to recover their phase shift after 15 h in the climatic chamber. Their phase shift annealed completely for a bias of $-1\,\mathrm{V}$ but did not reach the initial value for higher biases in the available time. The results indicate that more annealing time would have probably been required to obtain the same annealing for larger voltages. Even though the phase shift partially recovered in deep etch MZMs, their phase shift dropped to zero almost instantaneously after exposure to ionizing radiation

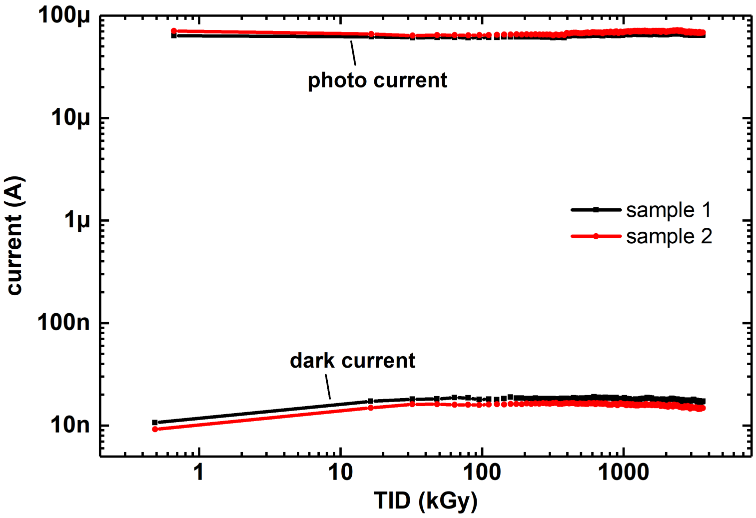

Figure 5.12: Dark- and photo-current of building block photodiodes at −1 V bias as a function of TID.

the second time. What defect type actually anneals at what rate is unknown. However, interface traps are typically thought to anneal quicker than positive trapped charge in the oxide [21]. It is therefore assumed that only a relatively small fraction of the positive trapped charge in the deep etch MZMs annealed and the phase shift recovery stopped somewhere on the steep degradation-slope from the the first irradiation. Thus, the second irradiation directly re-introduced enough damage such that the phase shift immediately degraded again.

The fact that annealing was observed in all of the tested MZMs directly implies that the dose rate affects the degradation rate of the devices. At lower dose rates or when there are intermediate pauses during the irradiation, similar to the actual conditions inside an HEP experiment, some of the radiation-induced damage could already anneal. It can thus be assumed that the same MZMs should be able to withstand higher TID levels than those determined during the online irradiation test if they were irradiated with a lower dose rate.

5.2.6 Dark- and photo-currents of photodiodes from the online irradiation test

The changes of the dark- and photo-currents of building block GeSi photodiodes when exposed to ionizing radiation were also studied during the online irradiation test. Both currents at a bias of −1 V are plotted as a function of TID in Fig. 5.12. The dark-currents roughly doubled during irradiation until a TID level of 3.6 MGy was reached. The maximum measured dark-current of 20 nA nevertheless remained

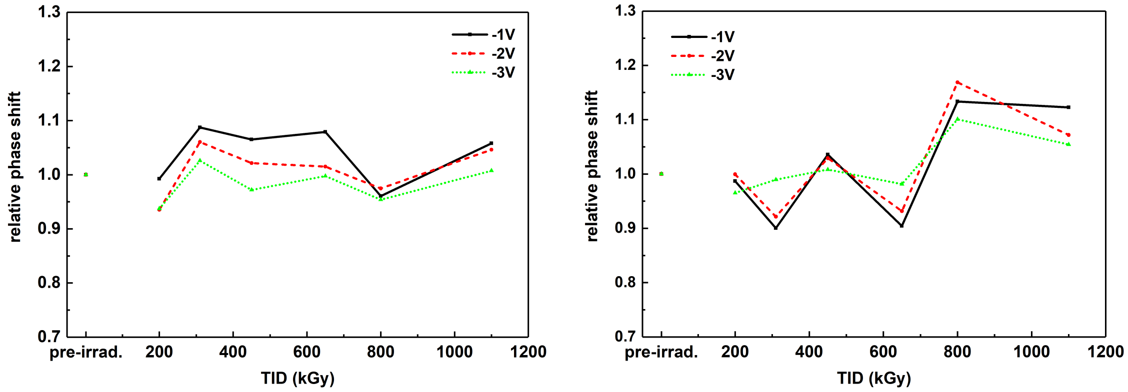

(a) deep etch **(b)** shallow etch

Figure 5.13: Relative phase shift change at $-1, -2, -3$ V of custom-design MZMs from the stepwise irradiation test at $-30\,°\mathrm{C}$. The MZMs had a nominal doping concentration and $w_{Dop} = 750$ nm and were not biased during irradiation.

low. One reason for the increase in dark-current could be x-ray-generated carriers in the photodiode that led to a small photo-current. However, calculating the expected x-ray-generated photo-current with Eq. (5.1) indicated that such a photo-current is in the order of pA. Thus, it cannot be responsible for the observed increase in dark-current. Instead, interface traps between germanium and silicon dioxide probably give rise to additional leakage paths that explain the higher dark-current.

The photo-currents stayed flat throughout the entire irradiation period. With approximately four orders of magnitude difference between the dark- and photo-currents, these outcomes demonstrate that photodiodes were not seriously affected by ionizing radiation. This was expected since x-rays do not create displacement damage. This would have decreased the photodiodes' responsivity and increased the dark-currents [210] due to additional generation-recombination centers.

5.2.7 Phase shift results from stepwise irradiation test at $-30\,°\mathrm{C}$ with un-biased samples

The third irradiation test revealed that neither deep nor shallow etch MZMs with nominal doping degrade when irradiated with x-rays at $-30\,°\mathrm{C}$ (Fig. 5.13). As mentioned in Section 5.1.3, a new die was irradiated for each TID level. The zigzag-like curve is thus partially due to pre-irradiation phase shift variations of up to 10 %. Superimposed to this effect is most likely also a phase shift enhancement as it was observed during all other irradiation tests. MZMs with both etch depths withstood to a TID level of 1.1 MGy without any obvious degradation. This is an improvement in radiation-hardness for deep etch MZMs of more than 11× compared to an irradiation at room temperature (cf. Fig. 5.3a). Shallow etch MZMs did not show a degradation either. This was expected as they also did not show any degradation up to about 1.7 MGy during the stepwise test at room temperature (cf. Fig. 5.3b).

The explanation why MZMs withstand to higher levels of ionizing radiation in a colder environment is the same as given in Sec. 5.2.1 for the IV measurements. The mobility of holes is reduced by two order of magnitude at $-30\,^{\circ}\mathrm{C}$ compared to room temperature. Therefore, the rate at which deep traps are filled and interface traps are built up is lower and the devices can withstand pinch-off for longer.

5.3 Simulation of x-ray induced phase shift degradation

The irradiation of the custom-design MZMs was simulated to understand why the phase shift degraded with increasing TID. The simulation procedure and the outcomes are presented in this section.

5.3.1 Model for simulating damage from ionizing radiation

The simulations were based on the model published in [182]. The introduction of trapped positive charge in silicon dioxide and the buildup of traps along the interface with silicon as a function of TID is included in the model. The irradiation model was implemented through the Physical Model Interface in Sentaurus Device. Its simulation flow is illustrated in Fig. 5.14. The model is based upon a transient simulation where each time-step corresponds to a TID level. Trapped positive charge in the oxide and interface traps are gradually added to the device while the time is incremented. Hydrogen-induced dopant passivation is not accounted for because neither the doping concentrations nor the free carrier densities can be directly manipulated with the Physical Model Interface. Such manipulation would however be necessary when modeling dopant passivation.

The trapped positive charges are added in the oxide within a layer of effective thickness η_{ot} from the interface to silicon. The effective maximum concentration of deep traps that can capture a hole is given by $N_{ot,max}$ (Fig. 5.15). Both parameters define the distribution of deep traps in the oxide. These deep traps are unoccupied

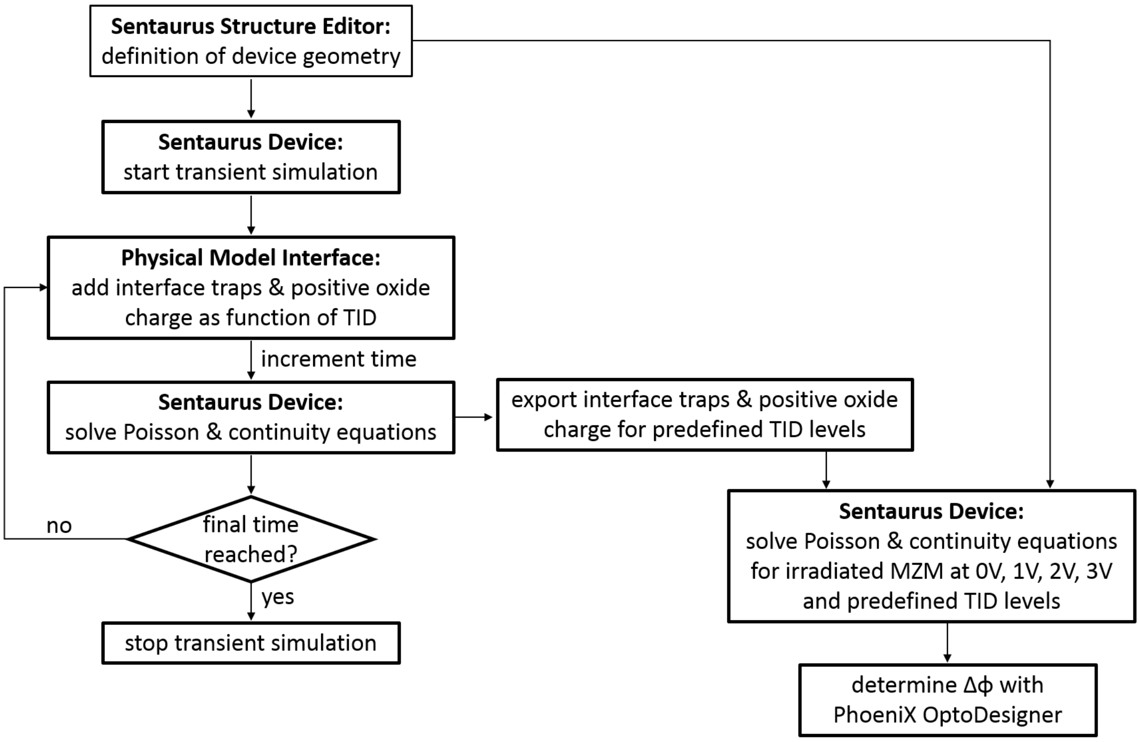

Figure 5.14: Flow-chart for the irradiation simulation in Sentaurus Device.

($N_{ot,0}$) before the transient simulation starts and can capture a hole and become occupied ($N_{ot,1}$) during the simulation. The number of holes that are trapped during each time increment (which equals a TID-step) is given by the number of generated ehps as defined in Eq. (3.4), the density of unoccupied deep traps, a trapping cross-section of holes σ_{ot} and the width η_{ot} over which the trapping can occur. The corresponding equation reads

$$N_{trap} = g_0 \cdot TID \cdot Y(E) \cdot N_{ot,0} \cdot \sigma_{ot}(E) \cdot \eta_{ot}. \tag{5.6}$$

The trapping cross-section $\sigma_{ot}(E)$ describes the dependency of the default trapping cross-section σ_0 on the electric field through [144]

$$\sigma_{ot}(E) = \frac{\sigma_0}{1 + 1.9 \cdot 10^{-4}|E|^{0.55}}. \tag{5.7}$$

The density of occupied traps, i.e. the actual density of trapped positive charge in the oxide, at any given time is simply the difference between available deep traps and unoccupied traps

$$N_{ot,1} = (N_{ot,max} \cdot \beta) - N_{ot,0}. \tag{5.8}$$

Here, β is a parameter to scale the maximum density of deep traps in the buried

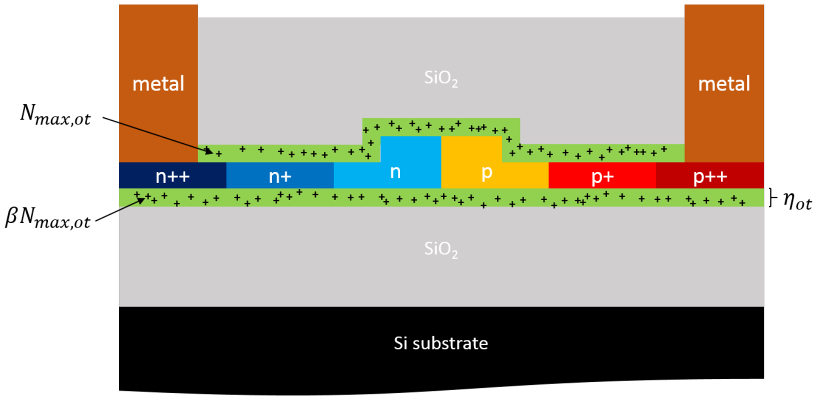

Figure 5.15: Illustration of the parameters for the radiation simulation. η_{ot} is the width of the layer where holes can be permanently trapped. $N_{ot,max}$ is the maximum allowed density of trapped holes within that layer. β is a scaling parameter for the maximum density of deep traps in the bottom oxide with respect to the top oxide.

oxide with respect to the maximum density of deep traps in the top oxide. Since the active silicon layer in SiPh typically needs to be a high-quality crystal [74, Section 12.3.1], it is assumed that a high-quality oxide is used for the buried oxide to reduce the density of dislocations during the growth of the active silicon layer. High-quality oxides typically have a lower defect density than rapidly grown top oxides, hence $\beta < 1$ for the buried oxide to account for this fact in the simulations.

The electron and hole interface trap densities N_{it} were modeled according to [143]

$$N_{it} = a_{it} \cdot TID^{b_{it}}, \tag{5.9}$$

with the exponent typically taking values in the range of $0.5 - 1.0$.

The concentration of trapped positive charge in the oxide and the interface trap densities were exported during the transient simulation at times that correspond to predefined TID levels. They were then imported into a second Sentaurus Device simulation where the bias was ramped from 0 V to −3 V. Similar to the simulations performed for the optimization of the phase shifter designs (cf. Sec. 4.2.1), the carrier densities were then extracted and the change in the effective refractive index of the guided mode computed with PhoeniX OptoDesigner.

5.3.2 Results for custom-design deep etch MZMs

The values for $N_{ot,max}$, σ_0, η_{ot}, β, a_{it} and b_{it} were varied until the simulated phase shift values matched the measured ones reasonably well. Simulation results for

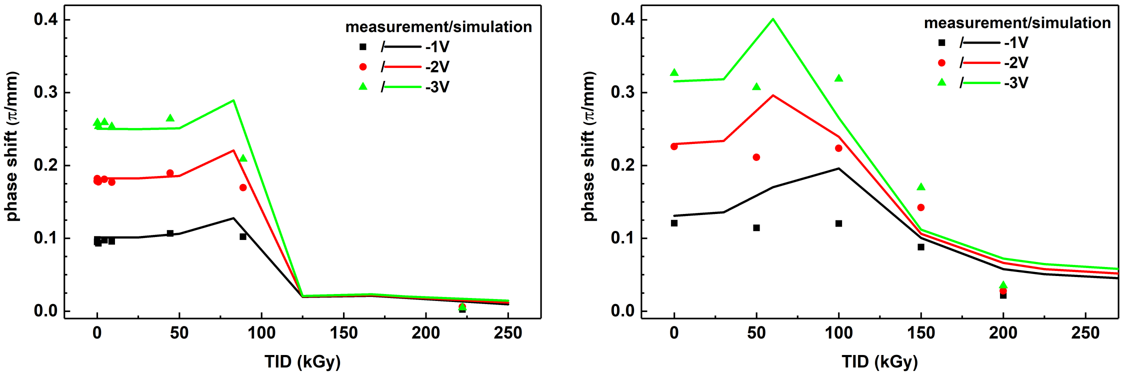

(a) nominal doping **(b)** 2× nominal doping

Figure 5.16: Simulated and measured phase shifts as a function of TID for deep etch MZMs that were irradiated without bias.

custom-design deep etch MZMs without bias during the transient simulation step are compared to measurements in Fig. 5.16. The plots show a very good agreement between measured and simulated phase shift values for deep etch MZMs with nominal doping. For deep etch MZMs with 2× nominal doping, the simulated phase shifts do not fully degrade and there is a stronger phase shift enhancement in the simulations than in the measurements. The less good agreement between measured and simulated values for MZMs with 2× nominal doping could be a result of the different process conditions used for wafers with nominal and 2× nominal doping concentration.

The values for the parameters used in the simulations were $\sigma_0 = 6.5 \cdot 10^{-14}\,\mathrm{cm}^2$, $\eta_{ot} = 20\,\mathrm{nm}$, $\beta = 0.3$, $a_{it} = 5 \cdot 10^4\,(\mathrm{rad} \cdot \mathrm{cm}^2)^{-1}$ for hole interface traps, $a_{it} = 5 \cdot 10^3\,(\mathrm{rad} \cdot \mathrm{cm}^2)^{-1}$ for electron interface traps and $b_{it} = 1$. For MZMs with nominal doping $N_{ot,max} = 5 \cdot 10^{19}\,\mathrm{cm}^{-3}$, while for MZMs with 2× nominal doping $N_{ot,max} = 9 \cdot 10^{19}\,\mathrm{cm}^{-3}$. $N_{ot,max}$ was increased for MZMs with 2× nominal doping because they come from a different wafer that was exposed to a higher fluence of dopants during the implantation step. It is assumed that more defects in the oxide consequently remained after processing.

These values and the resulting effective defects in the simulations are in good agreement with published values. $\sigma_0 = 6.5 \cdot 10^{-14}\,\mathrm{cm}^2$ is only 13 % lower than the value of $\sigma_0 = 7.5 \cdot 10^{-14}\,\mathrm{cm}^2$ reported in [211]. With the chosen values for a_{it} and b_{it}, interface trap densities in the order of $1 \cdot 10^{11} - 1 \cdot 10^{12}\,\mathrm{cm}^{-2}$ are reached at 250 kGy. This compares well with values published in [146, 151, 158]. For the same dose, the occupancy of deep traps reaches about $N_{ot,1} = 1 \cdot 10^{19}\,\mathrm{cm}^{-3}$ (Fig. 5.17d). Densities of trapped positive charge of up to $1 \cdot 10^{18}\,\mathrm{cm}^{-3}$ extending more than 20 nm into the oxide have been measured for samples that were exposed to lower TID levels [211, 212]. The chosen values for $N_{ot,max}$ and η_{ot} are thus reasonable given that they are considered effective values to reproduce the measured results.

The simulated hole concentrations in deep etch MZMs with nominal doping before irradiation and after a TID of 250 kGy are compared in Fig. 5.17a and 5.17b to understand the reason of the device failure. Qualitatively, it can be seen that the trapped positive charges in the oxide push the holes out of the p-doped slab. As a result, an island of holes forms inside the waveguide rib and the density of free holes in the p-doped slab reaches very low values. The holes in the rib thus become pinched-off from the p+ doping and the electrode.

The radiation-induced changes in the p-doped slab can be quantitatively analyzed by plotting the hole density in silicon (Fig. 5.17c) and the density of trapped positive charges in the oxide (Fig. 5.17d) along a cutline. The plots show that while the density of trapped positive charges increases with TID, the density of holes in silicon decreases to values below $1 \cdot 10^{7}\,\mathrm{cm}^{-3}$. Semiconductor regions with such a low carrier density exhibit a very high resistance. This increased resistance can also explain the reduced forward current measured during the online irradiation test (cf. Fig. 5.2b). In the devices at hand, this resistance is in series with the pn-junction of the phase shifter. When a reserve bias is applied, the voltage predominantly drops across the resistance instead of the pn-junction and the waveguide rib effectively becomes pinched-off from the electrical contacts. Carriers thus can no longer be swept out of the device. This is illustrated in Fig. 5.18 where the sum of depleted electrons and holes at $-3\,\mathrm{V}$, defined as

$$\left(N_h\Big|_{0\,\mathrm{V}} - N_h\Big|_{-3\,\mathrm{V}} \right) + \left(N_e\Big|_{0\,\mathrm{V}} - N_e\Big|_{-3\,\mathrm{V}} \right), \tag{5.10}$$

is plotted. The change in free holes in the rib and p-doped slab before irradiation was up to $2 \cdot 10^{18}\,\mathrm{cm}^{-3}$ and $1 \cdot 10^{16}\,\mathrm{cm}^{-3}$, respectively. After irradiation, it is two to three order of magnitude lower. For free electrons, the change is up to five orders of magnitude lower after irradiation. The radiation-induced reduction in the resulting change of the material's refractive index in the rib can be estimated with the Soref-Benett formula, as defined in Eq. (2.12), to be

$$\left(\frac{\Delta N_h\Big|_{-3\,\mathrm{V}}}{\Delta N_h\Big|_{0\,\mathrm{V}}} \right)^{0.8} \approx \left(\frac{1 \cdot 10^{16}\,\mathrm{cm}^{-3}}{2 \cdot 10^{18}\,\mathrm{cm}^{-3}} \right)^{0.8} = 0.014. \tag{5.11}$$

That means the change in the refractive index in the waveguide rib, where typically the largest change is induced, becomes only 1.4 % of the pre-irradiation value

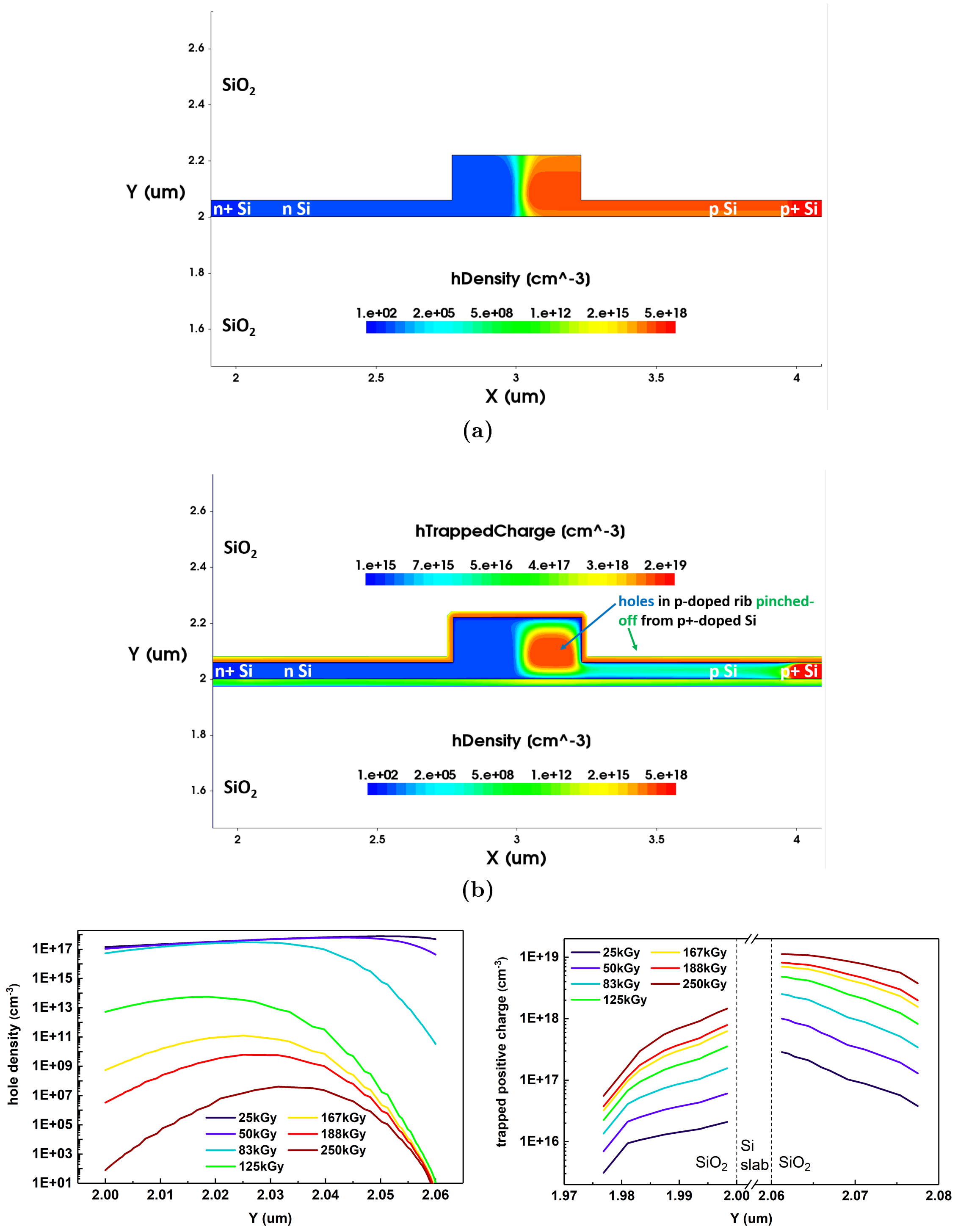

(a)

(b)

(c)

(d)

Figure 5.17: Simulated density of free holes in silicon before irradiation (a) and after 250 kGy (b) for a deep etch MZM with nominal doping and without bias during irradiation. The density of trapped positive charge in the oxide along the interface is also included in the right plot. These trapped positive charges push the holes in the p-doped slab area away and cause the holes in the waveguide rib to form an island that is electrically disconnected from the p+ doping. The hole density in silicon and the trapped positive charge in the oxide along $x = 3.5\,\mu\text{m}$ are plotted in (c) and (d), respectively.

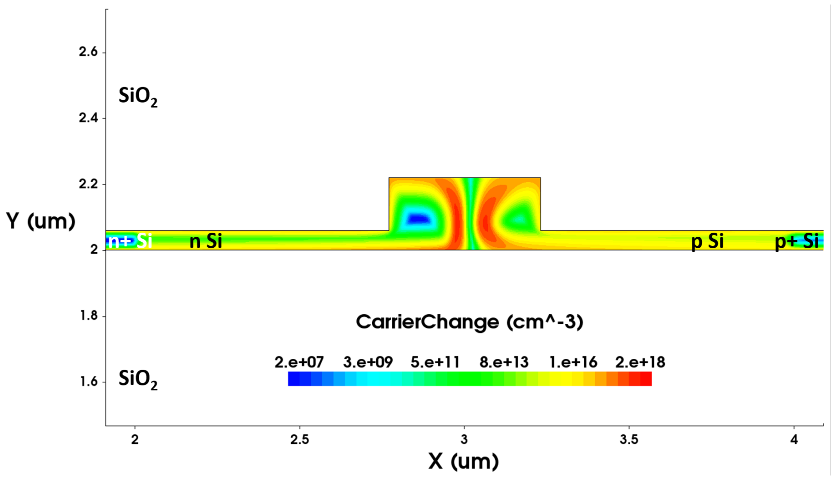

(a) before irradiation

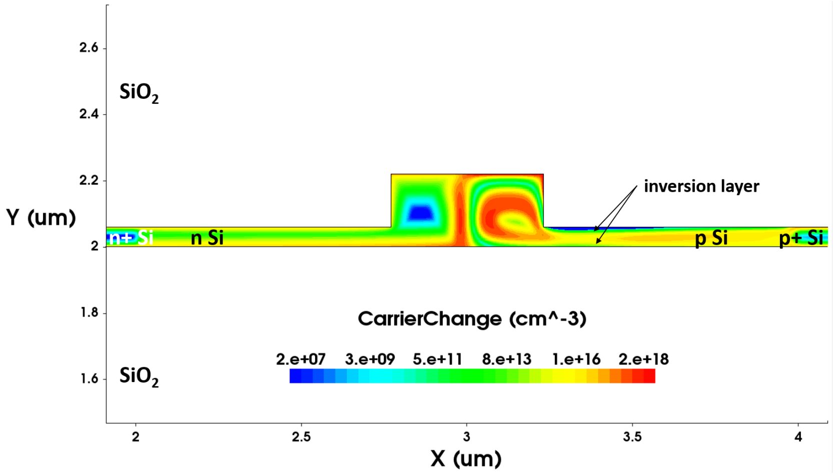

(b) after 83 kGy

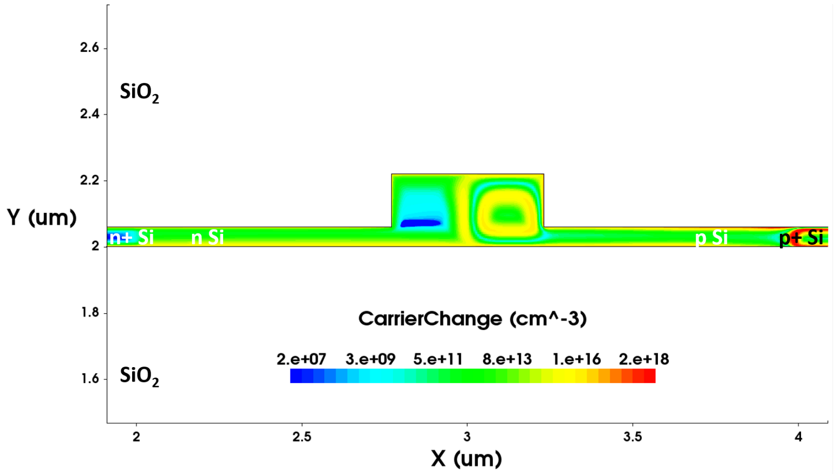

(c) after 250 kGy

Figure 5.18: Sum of depleted electrons and holes at −3 V before irradiation (a) and after a TID of 83 kGy (b) and 250 kGy (c) for a deep etch MZM with nominal doping. Comparing the density of depleted carriers before irradiation and after 83 kGy, one can see that fewer holes are depleted in an un-irradiated device and that an inversion layer is created along the interface after irradiation. After 250 kGy, the change in free carriers in the rib and p-doped slab is two to three order of magnitude lower than before.

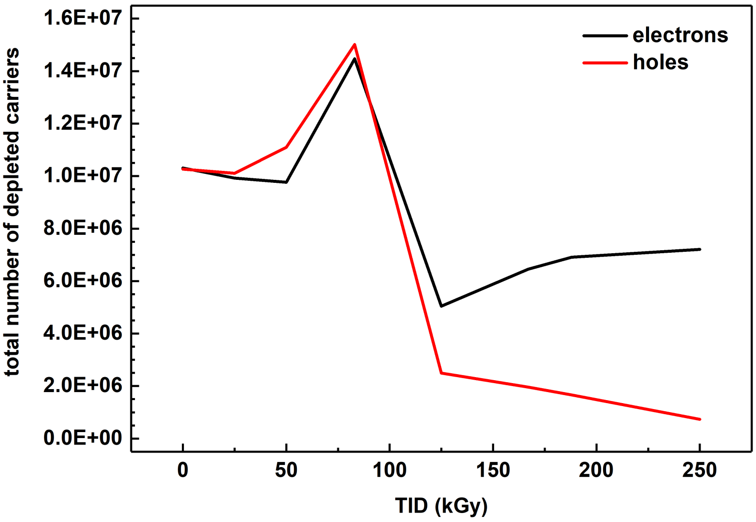

Figure 5.19: The total number of electrons and holes depleted from the n- and p-doped silicon ($x \in [2.02, 3.98]$, $y \in [2.00, 2.22]$) as a function of TID for a deep etch MZM with nominal doping.

after the MZM was irradiated. As modifying the refractive index in a waveguide constitutes the underlying principle of a phase shifter, a phase shift can no longer be created once the refractive index does not change due to the radiation-induced pinch-off in the device.

A similar analysis can be used to explain why the phase shift reaches a maximum before it then drops rapidly (as shown e. g. in Fig. 5.16). For the deep etch MZM with nominal doping, this maximum occurs at 83 kGy. Plotting the sum of depleted electrons and holes at −3 V at this TID level (Fig. 5.18b) reveals that more holes are depleted from the rib and the p-doped slab compared to an un-irradiated phase shifter. Consequently, a larger phase shift is created. The actual number of depleted electrons and holes at −3 V as function of TID is shown in Fig. 5.19. The numbers were obtained by integrating over the density of free electrons and holes in the n- and p-doped silicon at 0 V and −3 V, multiplying the integrals with the length of the phase shifter and subtracting the values from each other. Approximately 40 % more electrons and holes are depleted from the device at 83 kGy when compared to the pre-irradiation case. This is because trapped positive charge in the oxide induces an inversion layer in p-doped silicon and additional carriers can be depleted from there when a reverse voltage is applied.

At 250 kGy, only half the amount of electrons and 10× fewer holes are swept out of the pn-junction compared to the pre-irradiation case. The stronger reduction in hole change confirms that a pinch-off in the p-doped slab is responsible for the phase shift degradation in MZMs when they are irradiated.

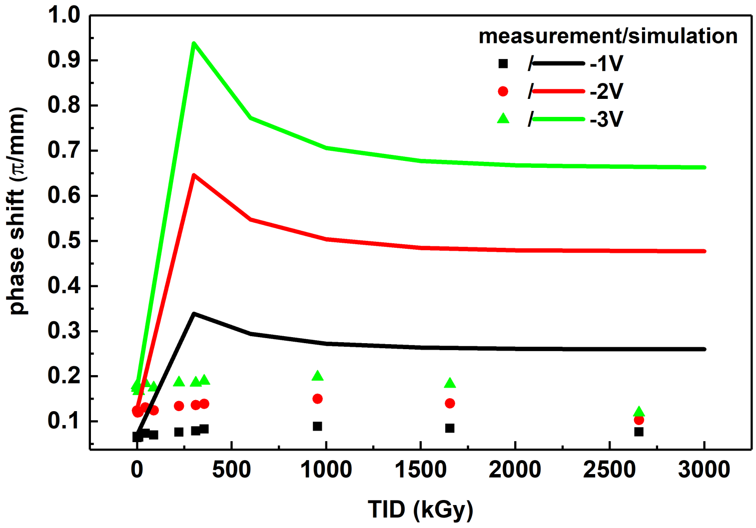

Figure 5.20: Simulated and measured phase shifts as a function of TID for a shallow etch MZM with nominal doping that was irradiated without bias.

Table 5.1: Sum of depleted electrons and holes at −3 V before irradiation and after a TID of 300 kGy for a shallow etch MZM with nominal doping.

TID [kGy]	electrons	holes
0	$1.03453 \cdot 10^7$	$1.03046 \cdot 10^7$
300	$1.14069 \cdot 10^8$	$1.1036 \cdot 10^8$

5.3.3 Results for custom-design shallow etch MZMs

When custom-design shallow etch MZMs were modeled with the same parameter set as deep etch MZMs, the simulated phase shift did neither quantitatively nor qualitatively match the measured values. As shown in Fig. 5.20, the simulated phase shift increased by more than 5-fold for the first TID step at 300 kGy. It then decreased by about 25 % and remained fairly flat. Simulating shallow etch MZMs with 2× nominal doping showed the same behavior and is not explicitly shown. This extremely large discrepancy between simulated and measured phase shifts can be attributed to the creation of wide inversion layers in the simulations. These inversion layers emerge in the p-doped slab along the interfaces with the oxide (Fig. 5.21), similar to the simulation of deep etch MZM e. g. at 83 kGy (cf. Fig. 5.18b). When simulating the application of a reverse-bias to a shallow etch MZM at 300 kGy, the inversion layers result in the depletion of many more carriers from the p-doped slab after 300 kGy than in the pre-irradiation case. The simulated total number of depleted electrons and holes therefore increases by approximately 10× (Tab. 5.1) for shallow etch MZMs with nominal doping whereas the increase was only about 1.4× for deep etch MZMs.

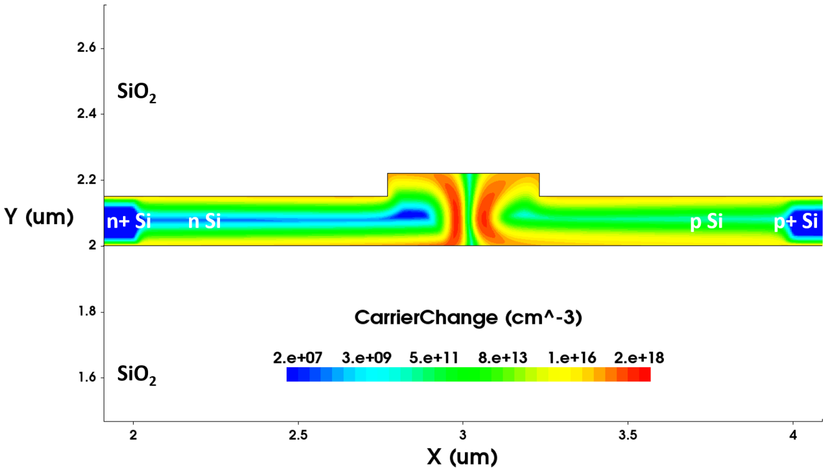

(a) before irradiation

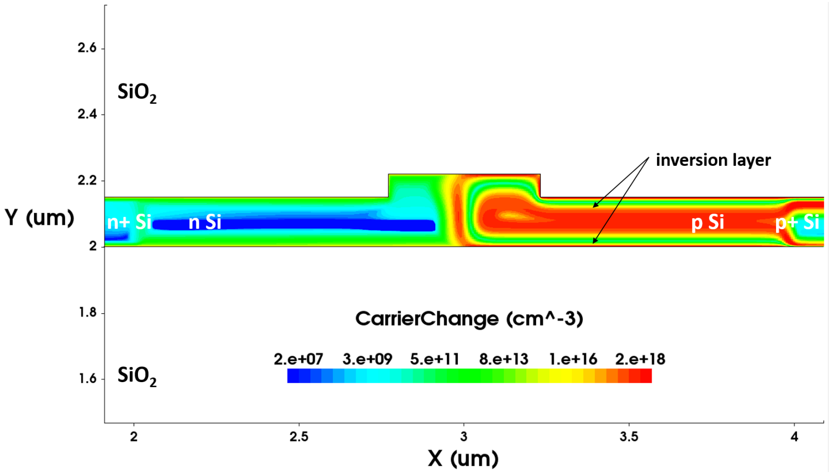

(b) after 300 kGy

Figure 5.21: Sum of depleted electrons and holes at −3 V before irradiation (a) and after a TID of 300 kGy (b) for a shallow etch MZM with nominal doping. The inversion in the p-doped slab along the interface with the oxide causes a very large amount of holes to be depleted from the device.

This difference is due to the thicker slab in shallow etch MZMs which accommodates more free carriers, especially given that the peak of the implantation lies within the thick slab (cf. Fig. 5.5). Hence, the reason why simulations for shallow etch MZMs are less accurate than for deep etch MZMs can be found in the electrostatic repulsion from the trapped positive charge in the oxide that acts upon the free holes in the p-doped slab. This repulsion is strong enough to push the majority of free holes out of the thin slab when simulating deep etch MZMs (cf. Fig. 5.18c). However, there are more free holes in a thick slab of shallow etch MZMs and the repulsion is thus not strong enough to create a pinch-off when simulating shallow etch MZMs. Instead, the free holes accumulate in the center of the slab and the inversion layers emerge.

Table 5.2: Relative doping concentrations compared to pre-irradiation values of a sample with nominal doping after exposure to 2.6 MGy.

implantation type	doping reduction
p	9 %
p+	53 %
n	32 %
n+	74 %

The overlap of the optical mode with the region where the carrier concentration changes also becomes larger because a larger fraction of the optical mode is guided in the slab of shallow etch MZMs compared to deep etch MZMs (cf. Fig. 4.5). The depletion of the inversion layer and the enhanced overlap of the optical mode with the depletion region thus caused the phase shift to significantly increase in the simulations whereas this increase could not be measured.

The phase shifts of shallow etch MZMs could likely be simulated more accurately if it was possible to include hydrogenation (cf. Sec. 3.3) in the model. Van-der-Pauw resistivity measurements on doped rectangles (cf. Fig. 4.7) clearly showed that the n- and p-doping concentrations were reduced between $26 - 91\,\%$ after irradiation up to 2.6 MGy (Tab. 5.2). The measurements also showed that more boron-acceptors are passivated by hydrogen than phosphorous-donors. This is in accordance with literature [169, 177]. The doped rectangles on the test chip were isolated from the surrounding material and structures through a 80 µm-wide trench and are not etched, i.e. the uniform height of the rectangles is 220 nm. The free carriers thus could not leave the rectangles or be pinched-off like in an etched waveguide structure. The measured reduction of dopants thus had to occur in the rectangle itself and is attributed to hydrogenation.

Based on the measurements, it can be inferred that the passivation of dopants affects the tested samples. A simulation was used to test this hypothesis. The simulation was run with the same model parameters as described above but also with a fixed p-type doping concentration that was reduced by 2.5× compared to the nominal doping. This allowed to check whether more realistic simulation results could be expected if hydrogenation were included in the model. The outcome confirmed that the phase shift values of shallow etch MZMs take on more reasonable values (Fig. 5.22). There is yet no quantitative agreement between measured and simulated phase shifts. This test, however, highlights that adding a gradual reduction of the p-type dopants as a function of TID into the existing model to account for hydrogenation would help in reproducing the measured phase shift values for shallow

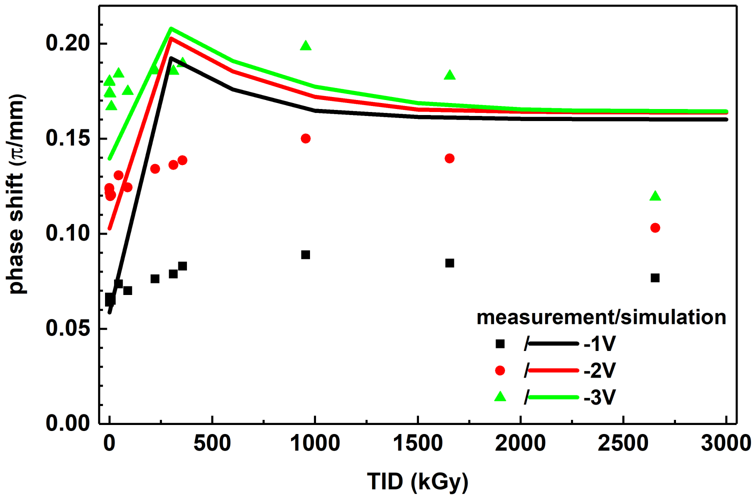

Figure 5.22: Simulated and measured phase shifts as a function of TID for a shallow etch MZM with 2.5× reduced p-doping concentration.

etch MZMs.

5.3.4 Limitations of the model when simulating biased samples or at lower temperatures

Carrier transport in the oxide, specifically hole hopping transport via shallow defect sites, is not included in the simulation model. Increased or decreased carrier velocities arising from higher electric fields due to biasing the MZM or reduced carrier mobilities at low temperatures, respectively, are thus not simulated. Consequently, the observed accelerated phase shift degradation during the online irradiation test and the delayed degradation when the samples were irradiated at $-30\,°\mathrm{C}$ cannot be reproduced.

The simulation allowed, however, the investigation of the magnitude of the yield-function, defined in Eq. (3.3), in un-biased and biased MZMs. Figures 5.23a and 5.23b demonstrates that a stronger electric field in reverse biased MZMs increases the yield in the oxide. Particularity around the waveguide, the yield in the reverse-biased MZM is approximately three times larger than in the un-biased MZM (Fig. 5.23c). With three times as many ehps escaping initial recombination, deep trap sites can be filled faster with holes and hydrogen can be released by holes in the oxide more rapidly. Thus, the same radiation-induced damage in the MZMs can be created at lower TID levels compared to un-biased devices.

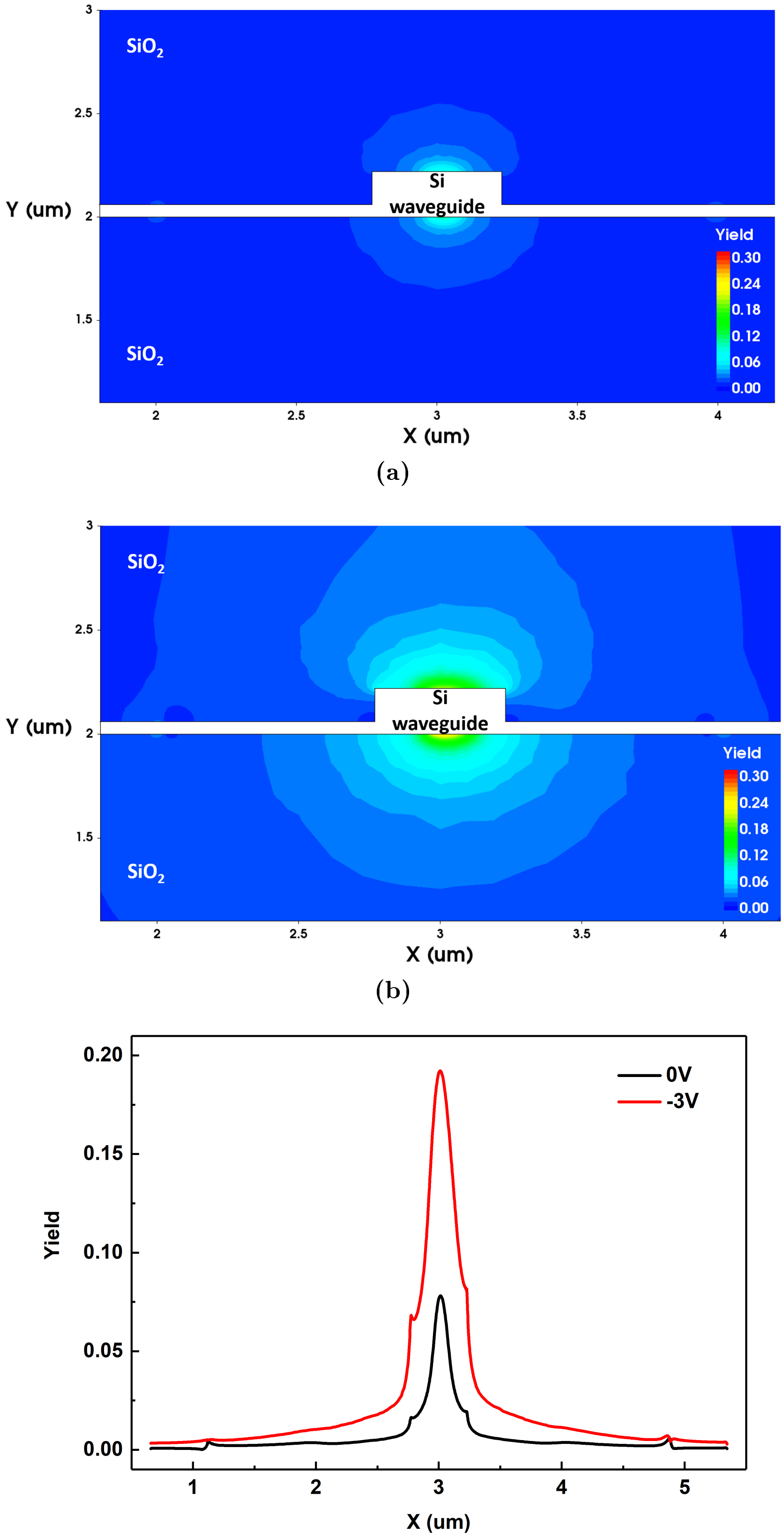

(a)

(b)

(c)

Figure 5.23: Yield of ehps that do not promptly recombine in un-biased (a) and reverse-biased (b) deep etch MZMs with nominal doping. The yield along $y = 2.225\,\mu\text{m}$ is plotted in (c).

5.4 Summary

The outcomes of the conducted irradiation tests showed that the phase shift of SiPh MZMs degraded faster when the devices were biased during irradiation, when a deep etch waveguide was used for the phase shifters or when the doping concentrations in the pn-junction were lower. The reason for the device degradation is a pinch-off of free holes in the waveguide rib from the electrode. The measurements also indicated that hydrogen-induced dopant passivation likely plays a role in the device failure. An MZM's radiation-hardness can be improved when a high doping concentration and a shallow etch depth waveguide is used. MZMs with such a design can withstand to more than the minimum targeted TID level of 1 MGy. Independent of the MZM design, irradiating MZMs at −30 °C also delays the phase shift degradation and leads to a better radiation-hardness.

6 Radiation-hard optical links based on silicon photonics transmitters

MZMs with an improved radiation-hardness that allows them to withstand to more than 1 MGy of ionizing radiation were identified in the previous chapter. Considerations on how such MZMs could be implemented into a system and what specifications this system would have are addressed in this chapter. Optical transmission tests were conducted to compare eye diagrams of irradiated MZMs to those of unirradiated samples. The Optical Modulation Amplitude (OMA) of the eye diagrams was calculated with an analytical model. This model was then used to predict how the OMA would change as a function of TID for a SiPh Tx operated at 10 Gb/s in a radiation-hard optical link. A design for such a Transmitter (Tx) is proposed. Its electrical power consumption is estimated and the optical power budget of a SiPh-based optical link calculated. Both are compared to the single-mode Versatile Link (VL) system that will be installed in the CERN experiments in 2018.

6.1 Electro-optical high-speed tests

Optical eye diagrams of irradiated MZMs were measured and compared to unirradiated reference samples. This allowed assessing whether the dynamic performance of MZMs changed after irradiation. However, the measured dynamic performance is not representative of a final system because the custom-design MZMs were not optimized for high-speed testing (see Sec. 4.3). This would have been necessary to obtain quantitatively meaningful results. A qualitative comparison between irradiated and reference samples can nonetheless be carried out.

The eye diagrams were measured on bare dies with a similar test setup as the one described in Sec. 4.4. Changing the light source, electric signal generator and optical

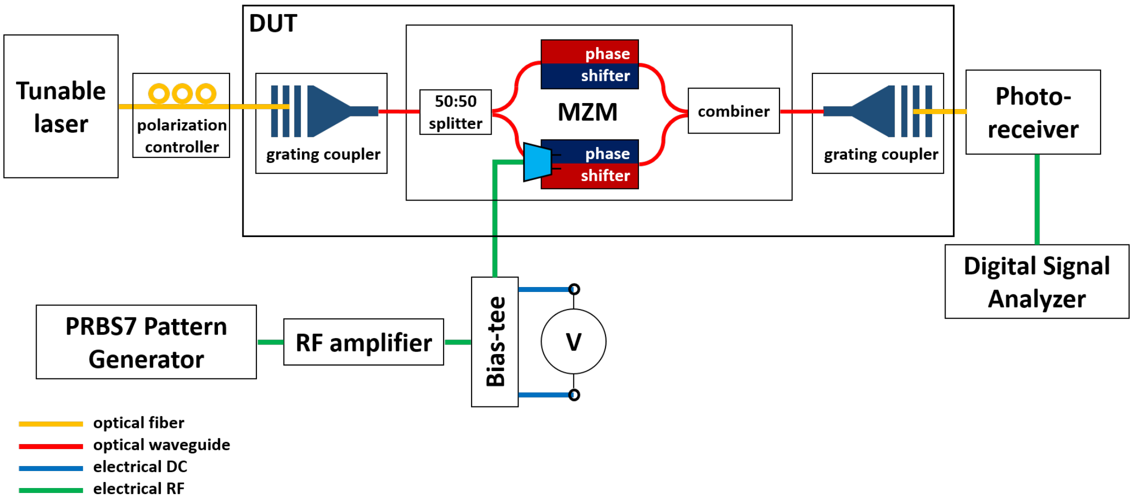

Figure 6.1: Schematic of the test setup to measure the eye diagrams of MZMs.

receiver was required to perform the eye diagram measurements (Fig. 6.1). Since the MZM do not have a dedicated phase shifter to set the quadrature point (cf. Fig. 2.5), a tunable laser was used to adjust the wavelength such that the MZM under test was at quadrature when biased at $V_{DC} = -3\,\mathrm{V}$. This bias was chosen such that the MZM was always in the reverse-bias regime during the test, i.e. the peak-to-peak voltage $V_{pp} < 2 \cdot V_{DC}$. The electrical data signal with which the MZM was driven had a bit rate of 10 Gb/s and was created with a *Agilent N4903B J-BERT*. A Pseudorandom Binary Sequence (PRBS) of length $2^7 - 1$ was used for the test. The pattern length was the same as the one used for the quality assurance in the production of the VL components [9]. The modulated signal from the J-BERT was amplified to a peak-to-peak voltage of $V_{pp} = 3.5\,\mathrm{V}$ with a *JDSU H301 Optical Modulator Driver* and combined with V_{DC} through a bias tee. It was applied to one phase shifter arm of the MZM under test with a *Cascade Infinity* RF probe. The modulated optical signal from the MZM was detected with a *New Focus 1544-A* photoreceiver that was connected to an *Agilent DSA 91204A Digital Signal Analyzer* where the eye diagrams were recorded.

Eye diagrams could only be recorded for samples with nominal doping as the optical power of the tunable laser was not high enough to compensate for the increased absorption losses occurring in samples with 2× nominal doping. Measured eye diagrams of deep and shallow etch MZMs that were exposed to 2.6 MGy are compared to eye diagrams from reference samples in Fig. 6.2. The eye diagrams were measured five months after the irradiation test took place because not all instruments required for the test were available directly after the irradiation test was finished. The irradiated samples were stored at room temperature in the meantime. The

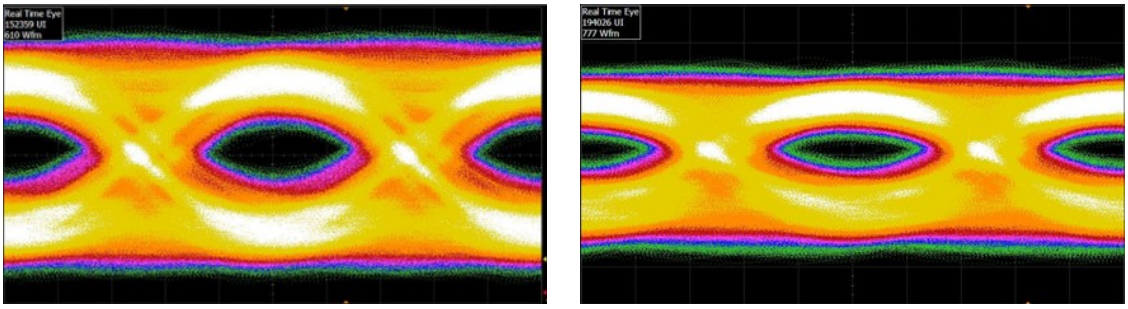

(a) deep etch, reference sample **(b)** shallow etch, reference sample

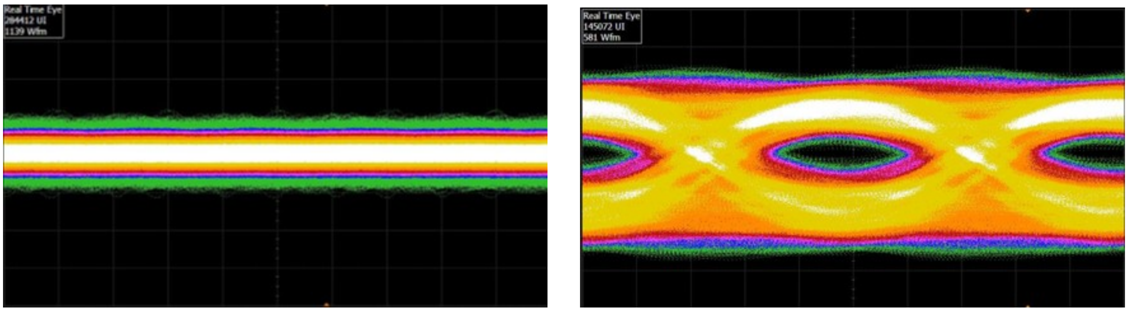

(c) deep etch, 2.6 MGy **(d)** shallow etch, 2.6 MGy

Figure 6.2: Comparison of eye diagrams at 10 Gb/s of un-irradiated reference samples and after irradiation to 2.6 MGy. The OMA for both shallow etch MZMs is approximately −8.5 dBm, while it is −7.4 dBm for the deep etch reference MZM. The ERs are 5.2 dB and 7.1 dB, respectively. OMA and ER were determined for the average on- and off-state optical power.

phase shift of the deep etch MZM recovered from zero after irradiation to 96 % of the pre-irradiation value during these five months. The phase shift of the shallow etch MZM annealed from 34 % to 85 % during that period.

Figure 6.2 shows that the eye of deep etch reference MZMs is more open than for shallow etch MZMs. This is due to a larger phase shift efficiency of deep etch MZMs (cf. Sec. 4.2.2). According to Eq. (2.16), this directly translates to a larger difference between on- and off-state during modulation. This difference is called Optical Modulation Amplitude and given through

$$OMA = P_{on} - P_{off}. \tag{6.1}$$

The eye opening for shallow etch MZMs could be increased if they were driven with a larger peak-to-peak voltage.

The comparison in Fig. 6.2 also displays that it is not possible to measure an eye diagram of irradiated deep etch MZMs. Only a straight line could be measured which indicates that irradiated deep etch MZMs can no longer be modulated even though they still show a phase shift after annealing. On the other hand, there is no significant difference in the eye diagram of irradiated and reference shallow etch MZMs. It can be inferred that the dynamic behavior of irradiated MZMs not only depends on the recovered phase shift. In addition, there must be an intrinsic change in irradiated deep etch MZMs that limits the modulation bandwidth and explains the difference to shallow etch MZMs.

The electrical S11-parameters of the same MZMs as used for the eye diagram tests were measured to determine whether the electrical response of irradiated deep etch MZMs is different to the response of the other samples. This test was conducted with a setup similar to the one depicted in Fig. 6.1. The pattern generator was however replaced with a *Keysight PNA N5225A* Network Analyzer that provides the modulated electrical signal and measures the electrical power and phase reflected from the MZMs. A short-open-load calibration was performed with the RF probe to account for the cabling used in the setup and measure the reflected power and phase of the signal accurately. Electro-optical S21-parameters were not measured because no tunable laser was available at the time of the test. So it was not possible to set the wavelength to the quadrature point of the MZM and measure the correct electro-optical frequency response.

The S11-results confirm that the electrical response of an irradiated deep etch MZM is different from the other samples (Fig. 6.3). Comparing the different curves shows that the irradiated and reference shallow etch MZMs as well as the reference deep etch MZM have a very similar response. The irradiated deep etch MZM on the other hand reflected approximately 4 dB less electrical power at 8 GHz.

The S11-measurement results were used to estimate how the electrical bandwidth of the MZMs reduces after irradiation. The measured S11-data was fitted to a simplified equivalent circuit model for a phase shifter in a lumped MZM [213]. This circuit is based on a series resistance R_S and junction capacitance C_J that represent the pn-junction in the phase shifter (Fig. 6.4). L_{line} is included to account for the inductance of the long metal traces in the custom-design MZMs. Their total lengths is $l = 2.4\,\mathrm{mm}$, with 1.9 mm from the phase shifter length and 0.5 mm for the connection between bond pad and phase shifter. For irradiated MZMs, R_{leak} was added to the circuit to represent the resistance of the leakage paths created by radiation. The capacitance due to trapped positive charge is accounted for with C_{oxide}.

The values for the five elements were varied in ANSYS Electronics Desktop [214] to find the best fit to the S11-measurements. Since custom-design MZMs do not

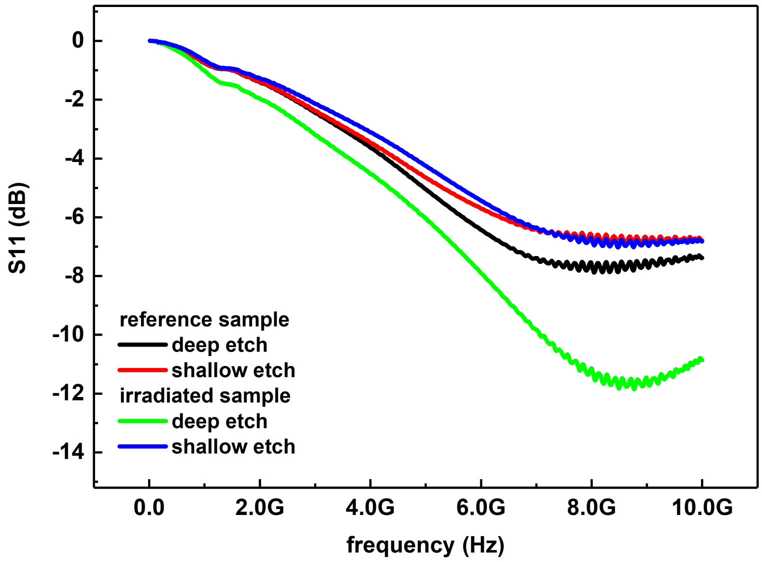

Figure 6.3: Reflected electrical power (S11) from the MZMs that were used for the eye diagram tests (cf. Fig. 6.2). All samples were biased at −3 V during the measurement.

have transmission lines (cf. Sec. 4.3), the measurement data was only fitted until the frequency where the lumped-element approximation for circuits is valid and the phase of the electrical signal can be regarded as constant. This frequency ν_{lumped} can be calculated by assuming that the corresponding wavelength is shorter than 1/10 of the total length l of the electrode [215, p. 204]. This yields

$$\nu_{lumped} = \frac{c}{10l\sqrt{\varepsilon_r}} \approx 6.3\,\mathrm{GHz} \tag{6.2}$$

with $\varepsilon_r = 3.9$ being the relative permittivity of the material (SiO_2) between the signal and ground electrode of the phase shifter. Figure 6.5 shows the outcomes of the fits. The reflected power (S11) and phase of the electrical signal match the measured values reasonably well given the simplicity of the model. The actual fit values used for the different elements before and after irradiation are specified in Tab. 6.1. L_{line} was only varied in the fitting procedure for the reference sample and then kept constant for fitting the irradiated sample because the metal traces should not be affected by the radiation. Therefore, their inductance should not change either. The value of $L_{line} = 0.8\,\mathrm{nH}$ is very close to the approximated inductance value for two parallel, flat and adjacent conductors given through [216, p.484]

$$L \approx \frac{\mu_0}{2\pi}\left[\ln\left(\frac{d_T}{w_T + t_T}\right) + \frac{3}{2}\right] l = 0.9\,\mathrm{nH}, \tag{6.3}$$

where μ_0 is the vacuum permeability, w_T and t_T the width and thickness of the

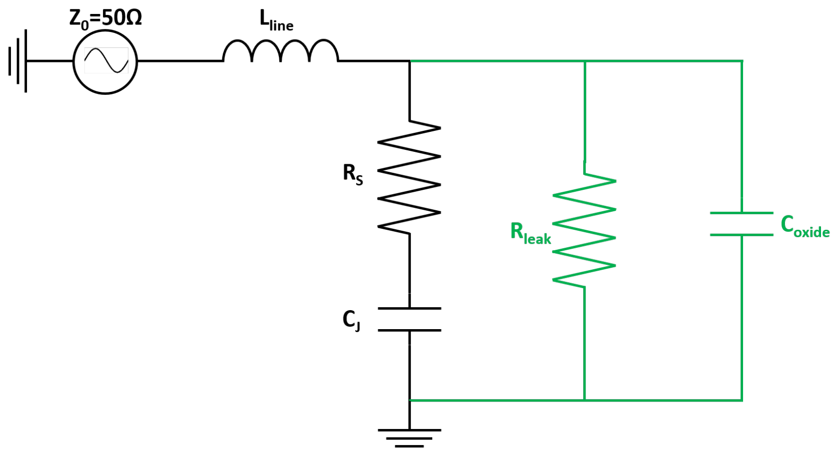

Figure 6.4: Simplified equivalent circuit of a phase shifter in an MZM to which the S11-data was fitted. The black part represents the phase shifter before irradiation. R_S and C_J are the series resistance and junction capacitance of the pn-junction, respectively. L_{line} accounts for the inductance in the metal traces. The green part is added when irradiated MZMs were fitted. R_{leak} and C_{oxide} are the resistance of the leakage paths and the capacitance due to trapped positive charge induced by radiation, respectively.

Table 6.1: Values of the individual elements for the S11-fit of deep etch MZMs to the equivalent circuit in Fig. 6.4. The fit results are shown in Fig. 6.5.

	before irradiation	after irradiation
R_S	20.3 Ω	47.0 Ω
C_J	0.6 pF	0.4 pF
L_{line}	0.8 nH	0.8 nH
R_{leak}	-	117 MΩ
C_{oxide}	-	0.1 pF

metal traces, respectively, and d_T their separation. The fitted series resistance before irradiation is comparabel to values published in [117,213]. The junction capacitance before irradiation can be estimated with the formula for a capacitor whose plates have a distance equal to the depletion width W_D and its area A is given by the height and length of the pn-junction [186, p. 85] in the phase shifter. With a relative permittivity of $\varepsilon_r = 11.7$ for silicon, the capacitance can be approximated with

$$C_J = \varepsilon_0 \varepsilon_r \frac{A}{W_D} = 0.6\,\mathrm{pF} \tag{6.4}$$

and perfectly matches the fitted value.

After irradiation, the capacitance decreased to 0.4 pF. This can be attributed to the fact that the n- and p-doped regions were no longer next to each other. Instead,

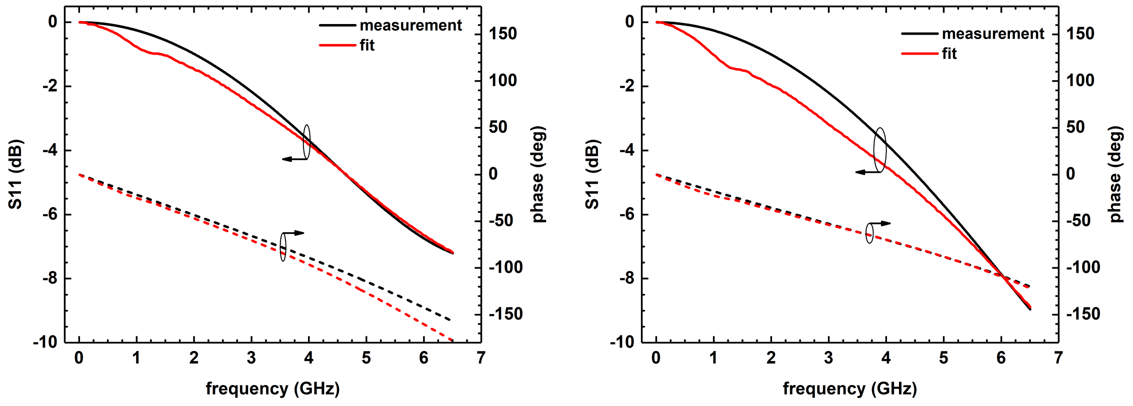

(a) reference sample **(b)** irradiated sample

Figure 6.5: Measured and fitted reflected electrical power (S11) and phase of a reference and irradiated deep etch MZM.

they were separated by a p-doped island and a region with very low carrier densities (cf. Fig. 5.17b) that form as a result of the pinch-off effect in the p-doped slab region. This resembles a configuration in which the distance between n- and p-doped regions is enlarged. According to Eq. (6.4), the capacitance consequently goes down. The series resistance of the pn-junction increases from 20.3 Ω before to 47.0 Ω after irradiation. This observation is compatible with a reduced carrier concentration in the p-doped slab due to the aforementioned pinch-off effect. Hence, the resistivity becomes larger. The order of magnitude for the resistance of the leakage path (117 MΩ) after irradiation seems also reasonable given the measured leakage currents were in the nA regime (cf. Fig. 5.2) and so

$$R_{leak} = \frac{V}{I} \approx \frac{1\,\mathrm{V}}{5\,\mathrm{nA}} = 200\,\mathrm{M\Omega}. \tag{6.5}$$

The corresponding electrical cutoff frequency for the reference sample can be calculated with Eq. (2.19) and yields $f_{3dB} \approx 13.0\,\mathrm{GHz}$. When the additional resistance of the leakage path and capacitance of the trapped positive oxide charge are taken into account for the irradiated sample, the equivalent resistance R_{eq} and equivalent capacitance C_{eq} of the circuit are

$$R_{eq} = \left(\frac{1}{R_S} + \frac{1}{R_{leak}}\right)^{-1} \quad \text{and} \quad C_{eq} = C_J + C_{oxide}. \tag{6.6}$$

The irradiated sample then has a electrical cutoff frequency of

$$f_{3dB} = \frac{1}{2\pi R_{eq} C_{eq}} = 6.7\,\mathrm{GHz}. \tag{6.7}$$

The modulation bandwidth thus halved after irradiation. The available bandwidth after irradiation should nonetheless be enough to see a modulated optical signal when trying to measure eye diagrams at 10 Gb/s of the irradiated deep etch MZMs. Therefore, the reduction cannot explain the measured straight line in Fig. 6.2c. Consequently, a second mechanism had to affect the modulation bandwidth and cause the MZM to be unable to produce a modulated optical signal.

Typically, the modulation bandwidth in a reverse-biased MZMs is determined by the RC-constant of the pn-junction because the carrier lifetimes are very short (cf. Sec. 2.5.2). However, the performed analysis indicated that the RC-constant of irradiated MZMs cannot be the limiting factor here. It is thus likely that the carrier lifetimes in MZMs were affected by radiation.

As mentioned above, measurements of a irradiated deep etch MZM displayed that its phase shift almost entirely annealed between the irradiation test and when the eye diagrams were measured. However, the non-existent eye diagram suggests that the state of the tested MZM is different from its pre-irradiation state. On the other hand, the phase shift recovery suggests that the MZM annealed to a state similar to before the phase shift rapidly dropped during the irradiation test (cf. Fig. 5.3a). Hence, it can be assumed that the state of the tested deep etch MZM is between 0 kGy and 100 kGy, for instance like at 50 kGy in Fig. 5.16a. There, the phase shift hardly changed compared to its pre-irradiation value but the device was already exposed to half of the TID needed to cause the phase shift to vanish. The corresponding 2D carrier densities were simulated and are plotted in Fig. 6.6 and 6.7. The plots show that the accumulation of trapped positive charge in the oxide already caused some pinch-off in the p-doped slab region. The hole density consequently reduced by about six orders of magnitude when compared to the pre-irradiation case, whereas the electron density increased by up to nine orders of magnitude. A detailed plot of the density values for both carrier types along a cutline at $x = 3.5\,\mu\text{m}$ (Fig. 6.8) reveals that the p-doped slab becomes essentially intrinsic. The hole and electron densities were roughly $1 \cdot 10^{17}\,\text{cm}^{-3}$ and $1 \cdot 10^{3}\,\text{cm}^{-3}$, respectively, before irradiation and the slab was thus clearly p-doped. Both carrier densities became around $1 \cdot 10^{10}\,\text{cm}^{-3}$ after 50 kGy. This resembles carrier concentrations in intrinsic silicon in which the number of free holes and electrons is of the same order of magnitude. Many of those intrinsic carriers will recombine with each other and additionally injected carriers cannot easily find a recombination partner. Consequently, the recombination lifetime of additional electrons injected into the p-doped slab under reverse bias will be much longer because it will take them longer to find a free hole to recombine with.

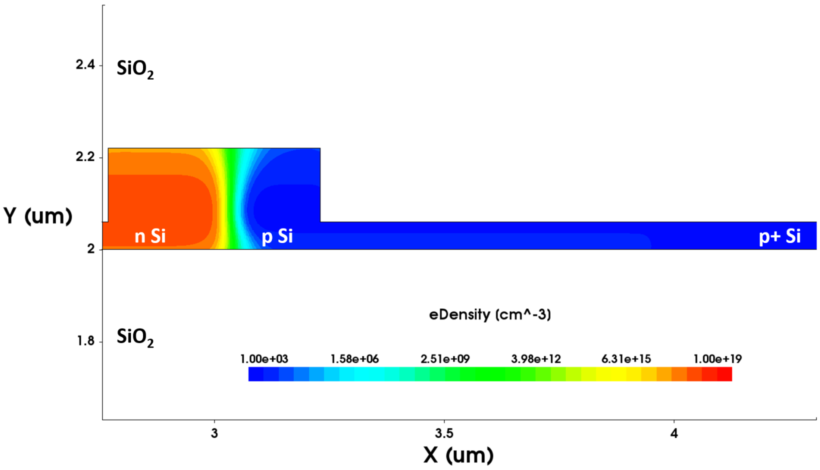

(a) electron density at 0 kGy

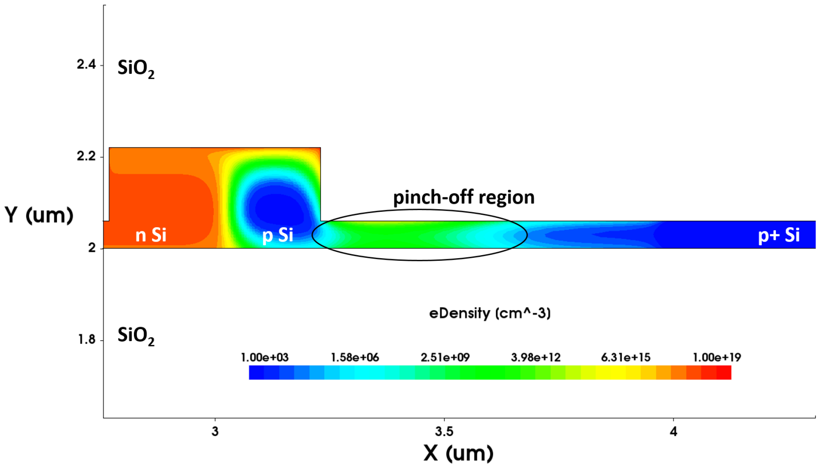

(b) electron density at 50 kGy

Figure 6.6: Simulated electron densities of a deep etch MZM with nominal doping before irradiation and after 50 kGy. The incipient pinch-off effect in the p-doped slab leads to an increase in electron density and a decrease in hole density. The electron densities along $x = 3.5\,\mu\mathrm{m}$ are plotted in Fig. 6.8.

The pre-irradiation carrier lifetimes in reverse-biased MZMs is typically short enough to support modulation bandwidth beyond the RC-limit. Otherwise the carrier lifetimes and not the RC-constant would be the limiting the modulation bandwidth. Carrier lifetimes in reverse-biased silicon MZMs are in the order of magnitude of 100 ps [217, 218] before irradiation. According to [219], the electron lifetime in p-doped silicon increases by more than three orders of magnitude for the simulated acceptor densities at 0 kGy and 50 kGy. If it were assumed that the carrier lifetimes τ in reverse-biased MZMs follow the same correlation, the modulation bandwidth would scale down accordingly from the GHz- to the MHz-range. Such a modulation bandwidth would be too low to produce any modulated output and hence could explain the measured straight line instead of an eye diagram for irradiated deep etch MZMs.

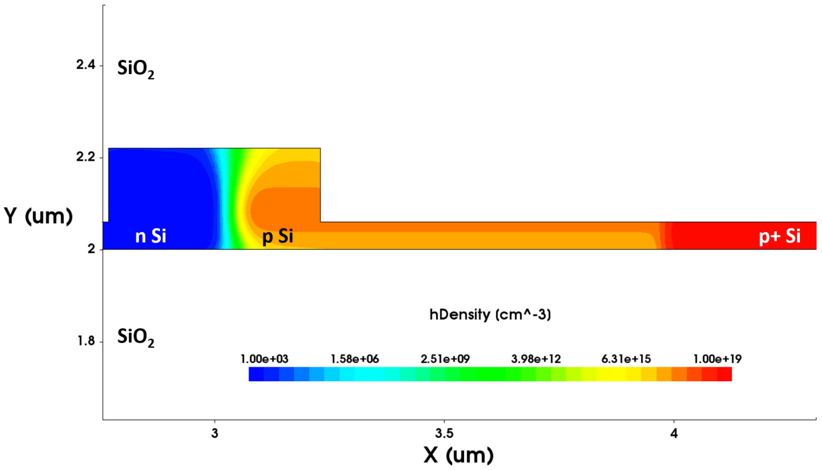

(a) 0 kGy

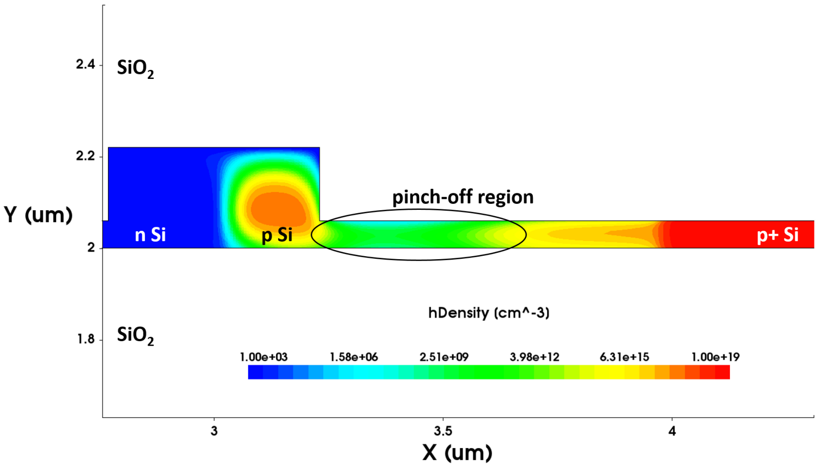

(b) 50 kGy

Figure 6.7: Simulated hole densities of a deep etch MZM with nominal doping before irradiation and after 50 kGy. The pinch-off effect already started in the p-doped slab. This leads to a decrease in hole density but also an increase in electron density. The hole densities along $x = 3.5\,\mu\text{m}$ are plotted in Fig. 6.8.

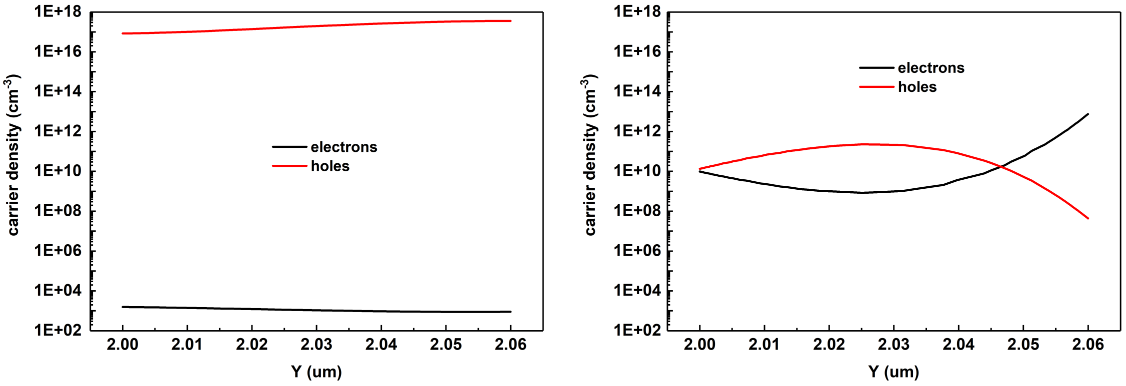

(a) 0 kGy **(b)** 50 kGy

Figure 6.8: Simulated electron and hole densities of a deep etch MZM with nominal doping before irradiation and after 50 kGy along $x = 3.5\,\mu\text{m}$ taken from Fig. 6.6 and 6.7.

It is assumed that irradiated shallow etch MZMs are not affected by this because they did not experience a full pinch-off in their thick slab. Otherwise, their phase shift would have vanished, too. Consequently, there will be no intrinsic-like region which limits the modulation performance and an open eye could be measured.

6.2 Modeling the Optical Modulation Amplitude

It is required to model the OMA based on measured phase shift values to be able to predict the system performance of SiPh-based radiation-hard optical links as a function of TID. As the OMA is determined by the optical power levels of the MZM in the on- and off-state, these power levels can be calculated for an ideal MZM without losses with the transfer function as given in Eq. (2.16). In reality, however, optical power is lost in an MZM due to e. g. absorption and scattering. Taking losses into account, the on- (P_{on}) and off-state (P_{off}) power levels of an MZM become

$$P_{on/off} = \frac{P_{in}}{2}\left(1+\cos\left[\frac{\pi}{2}\mp\Delta\phi\left(\frac{V_{pp}}{2}\right)\right]\right)-\left(\alpha_{MMI}+\alpha_{CPL}+\frac{1}{2}\alpha_{WG}\right), \tag{6.8}$$

$$P_{in} = P_{Las}-\left(\alpha_{MMI}+\alpha_{CPL}+\frac{1}{2}\alpha_{WG}+\alpha_{MZM}+\alpha_{EL}\right). \tag{6.9}$$

Here, P_{Las} is the optical power of the laser that is fed into the MZM and α_{MMI}, α_{CPL}, α_{WG} and α_{MZM} are the losses of the 50:50 splitter/combiner, grating coupler, routing waveguides and phase shifters, respectively. α_{EL} accounts for the varying coupling losses that occurred during the manual alignment of the lensed optical fibers to the grating couplers for each tested MZM. V_{pp} is the differential peak-to-peak voltage that is applied to both arms. If only one arm was driven, twice that V_{pp} had to be applied to this arm to get the same OMA.

The OMA can be modeled with the above formula if the frequency response of the MZMs is flat up to 10 GHz, i.e. the modulation bandwidth is wide enough to not diminish a 10 Gb/s-signal. This is a realistic assumption for MZMs with properly designed electrodes as devices with a bandwidth exceeding tens of GHz were already demonstrated [57].

The model was verified by comparing calculated OMA values with measured ones (Fig. 6.9). The measurements were done with building block MZMs that have traveling wave electrodes and support bit rates of up to 25 Gb/s. The modulation bandwidth of these MZMs as specified by imec is 11 GHz at −2 V and thus complies

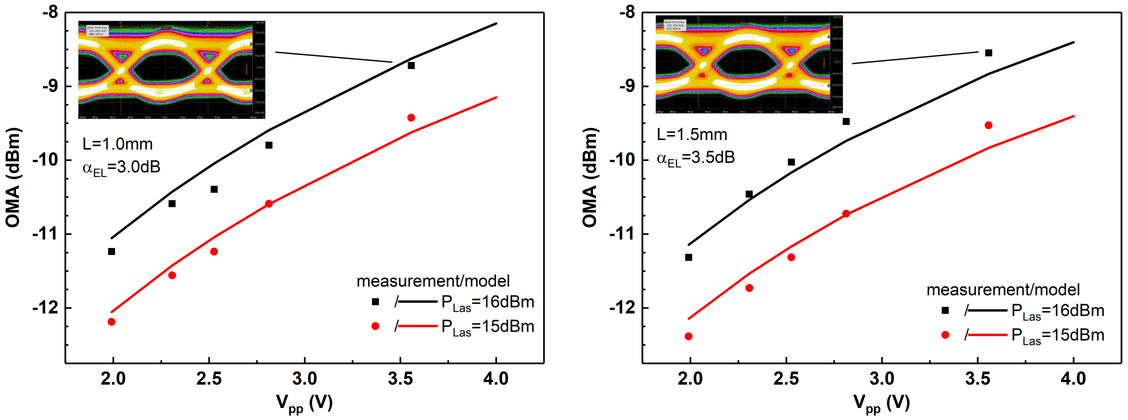

(a) **(b)**

Figure 6.9: Comparison of measured (10 Gb/s) and modeled OMA for two building block MZMs with traveling wave electrodes and phase shifter length of 1.0 mm (a) and 1.5 mm (b). The bias voltage for these measurements was $V_{DC} = -3\,\text{V}$. Example eye diagrams are shown as insets.

with the aforementioned assumption. The MZMs were terminated with an off-chip 50 Ω-load that was connected to a second RF probe to avoid RF power being reflected back at the end of the traveling wave electrodes. Distortions in the devices' dynamic performance could be avoided in this way. The loss values for the calculations of the OMA were $\alpha_{MMI} = 1.0\,\text{dB}$, $\alpha_{CPL} = 4.0\,\text{dB}$, $\alpha_{WG} = 1.7\,\text{dB}$. Based on the good agreement between measured and modeled OMAs for different phase shifter lengths, V_{pp}'s and laser powers it can be concluded that the OMA-model can be used to predict the performance of SiPh-based optical links.

6.3 Proposal for transmitter-architecture and system performance

The fact that shallow etch MZMs exhibit a phase shift and open eye diagrams after irradiation confirms that such devices could be used as transmitters (Tx) in radiation-hard optical links. The design of the MZMs would need to be upgraded for such a Tx to be tested in an actual link configuration. A proposal for such an upgrade and how the OMA of it would change as a function of TID is presented in this section.

6.3.1 SiPh Tx chip optimized for system implementation

MZMs with high-speed electrodes that allow for 10 Gb/s-operation and a mechanism to control and adjust the quadrature point (cf. Fig. 2.5) would be needed for an actual radiation-hard SiPh-based optical link. The quadrature control is particularly important to compensate for shifts in the quadrature point. These shifts could arise e. g. from drifts in the lasing wavelength or temperature variations. If the quadrature point was not controlled in such a case, the MZM would no longer be operated in its optimal condition and the OMA would reduce. A higher number of bit errors would result.

Controlling the state of an MZM with respect to its quadrature point can be achieved e. g. by tapping some light power at the input of the MZM and comparing it with the power after a quadrature phase shifter [220, 221]. A quadrature phase shifter provides the same functionality as a phase shifter in an MZM without the need to operate at high speeds. Injection-type pin phase shifters (cf. Fig. 2.6) are often used in commercial devices for that purpose because they have a high phase modulation efficiency and thus can be short. However, it is not possible to use injection-type phase shifters in HEP experiments since their pin-junctions can change as a consequence of radiation (cf. Sec. 3.1). Using an additional depletion-type phase shifter is possible but would make the total Tx larger due to the lower phase modulation efficiency and thus the required length. Instead, thermo-optic phase shifter are the best candidate because the strong thermorefraction in silicon (Sec. 2.2.1) can be exploited and short phase shifters can be realized. Furthermore, they can be implemented through metal lines which would not be affected by radiation.

A proposal for a design of a radiation-hard SiPh Tx as it could be installed in an HEP experiment is depicted in Fig. 6.10. In the proposed configuration, the Tx and its feed-laser would be installed in the radiation zone of an HEP experiment. The Tx would go in the innermost regions of the particle detector where the highest radiation levels occur. There it would take measurement data from the particle sensors and send it to the counting room for further processing. The feed-laser would be placed a few meters away from the innermost detector regions to reduce the radiation levels it will be exposed to and thus delay radiation-induced degradation. The driver of the MZM and the implementation for a quadrature control is also indicated in Fig. 6.10. The controller for the latter would be based on a simple radiation-hard circuit to process the information from the monitor PDs and adjust the power for the thermo-optic heater accordingly.

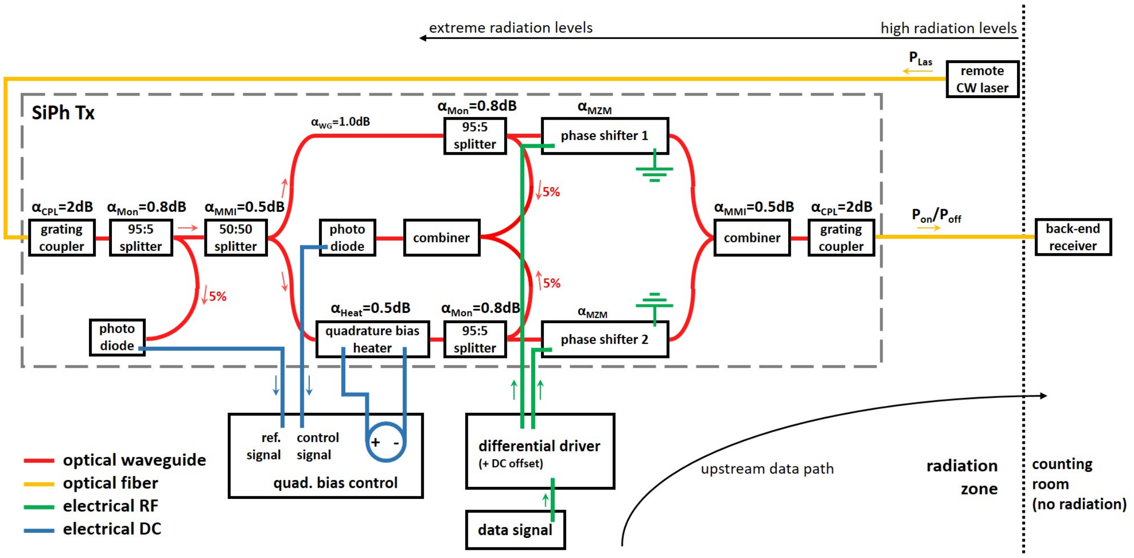

Figure 6.10: Proposal for the use of a SiPh Tx in a HEP experiment. The Tx and its feed-laser would be installed in the radiation zone. There, the MZM is driven with data from a particle sensor and sends it to the counting room. The laser would be installed in a region with lower radiation levels to avoid radiation-induced degradation. The Tx has a thermo-optic phase shifter to control the quadrature point of the MZM. Values for the losses of passive components are indicated above the corresponding element.

It is important that all passive optical components in a radiation-hard SiPh Tx have losses as low as possible. This is a consequence of the high doping concentrations and shallow etch depth needed to improve the radiation-hardness of MZMs. Both entail significant optical losses compared to commercial devices. Target values for the losses of these passive components are also indicated in Fig 6.10. The estimations for these losses are based upon published values for losses in grating couplers of approximately 1.2 dB [222,223], MMI losses of less than 0.1 dB [224] and propagation losses in un-doped waveguides of 2.4 dB/cm [225].

6.3.2 Required laser power and optical power budget

If a SiPh-based optical link were based on this layout proposal, it must have a minimum laser input power to provide the required OMA for the target application. For the receivers (Rx) in the counting room to ensure a Bit-Error-Rate (BER) of lower than $1 \cdot 10^{-12}$, as defined in specifications for the upcoming Versatile Link (VL) system [10], the OMA of a single-mode Tx needs to be at least -5.2 dBm. The optical laser power required to obtain this minimum OMA with the proposed SiPh Tx can be calculated with Eq. (6.8). As the light from the feed-laser in an actual Tx is not coupled manually into the grating couplers and the losses due to

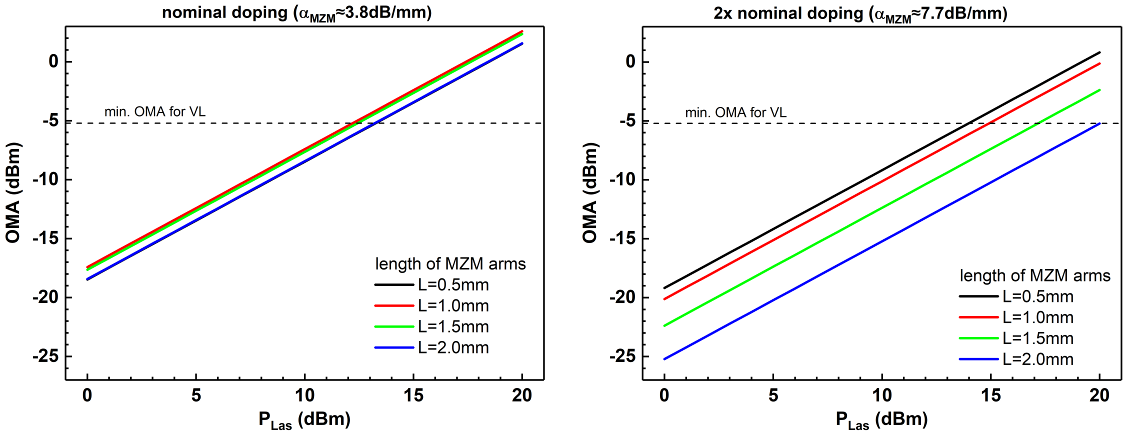

(a) **(b)**

Figure 6.11: OMA as a function of laser power for SiPh Tx as proposed in Fig. 6.10 with nominal (a) and 2× nominal doping (b). A differential $V_{pp} = 2\,\mathrm{V}$ was used for the calculations.

the quadrature control mechanism need to be taken into account, Eq. (6.9) becomes

$$P_{in} = P_{Las} - \left(\alpha_{MMI} + \alpha_{CPL} + \frac{1}{2}\alpha_{WG} + \alpha_{MZM} + \alpha_{Heat} + 2 \cdot \alpha_{Mon}\right). \tag{6.10}$$

α_{Heat} and α_{Mon} are the losses of the thermo-optic heater and the splitters for the monitor PDs, respectively, needed for the quadrature control. The OMA as a function of laser power for Tx with phase shifters based on the same design as the ones in custom-design shallow etch MZMs was calculated for both doping concentrations, MZMs with different lengths and a differential drive voltage of $V_{pp} = 2\,\mathrm{V}$ (Fig. 6.11). The calculations showed that a laser power of at least 12.2 dBm would be needed for MZMs with nominal doping and a length of either 1.0 mm or 1.5 mm. 1 dB more power would be needed for MZMs with 0.5 mm or 2.0 mm long phase shifters. The phase shift in a 2.0 mm-device is larger than in shorter devices and should thus lead to a larger OMA for the same laser power. However, the accompanying increase in absorption losses will reduce the difference between the MZM's on- and off-state and consequently decrease the OMA. This is the opposite for a 0.5 mm-long MZM. The absorption losses are lower because of the shorter length but the resulting phase shift that can be acquired over this length is also limited and the OMA decreases compared to 1.0 mm-long samples.

The very high absorption losses in MZMs with 2× nominal doping lead to a similar effect. The lowest laser power (14 dBm) that yields a minimum OMA of -5.2 dBm at $V_{pp} = 2\,\mathrm{V}$ is found for the shortest phase shifter length. For longer lengths, the losses dominate over the phase shift and a higher laser power would be required to

Table 6.2: Pre-irradiation optical power budget for SiPh Tx with different doping levels and laser input powers. The values are compared to a single-mode Tx from the Versatile Link project.

	nominal doping, $L = 1.0\,\mathrm{mm}$		2x nominal doping, $L = 0.5\,\mathrm{mm}$		Versatile Link [10]
	$P_{Las} = 12.2\,\mathrm{dBm}$	$P_{Las} = 20\,\mathrm{dBm}$	$P_{Las} = 14\,\mathrm{dBm}$	$P_{Las} = 20\,\mathrm{dBm}$	single-mode Tx
Tx OMA [dBm]	−5.2	2.6	−5.2	0.8	−5.2
max. Rx sensitivity [dBm]	−12.6	−12.6	−12.6	−12.6	−12.6
power budget [dB]	7.4	15.2	7.4	13.4	7.4
fiber attenuation [dB]	0.1	0.1	0.1	0.1	0.1
connector insertion loss [dB]	2	2	2	2	2
link penalty [dB]	1.5	1.5	1.5	1.5	1.5
margin [dB]	**3.8**	**11.6**	**3.8**	**9.8**	**3.8**

get the same OMA.

Based on the obtained minimum feed-laser power levels, the optical power budget and margin for SiPh Tx before irradiation were calculated (Tab. 6.2). The margin is an important characteristic of an optical link. It is given by the Tx OMA minus the maximum Rx sensitivity minus all link penalties. A positive margin indicates that the optical power detected by the Rx in the counting room is high enough to distinguish reliably between transmitted bits and thus provide the required BER. The BER in the Rx will increase if the margin drops below zero. The calculations summarized in Tab. 6.2 were also done for a laser power of $P_{Las} = 20\,\mathrm{dBm}$ to show how the margin of the optical power budget can be increased at the cost of a higher laser power. The values for the minimum sensitivity of the receiver in the counting room and all penalties were taken from the VL power budget calculations [8]. The margins in the power budget calculations for the minimum laser powers are thus identical to the one for the VL single-mode Tx (3.8 dB). The margins rise and range from 9.8 dB to 11.6 dB if the laser power is increased. This implies that the SiPh Tx should withstand to higher TID levels before the margin drops below zero.

The evolution of the OMA as a function of TID can be predicted when the pre-irradiation phase shift values in Eq. (6.8) are replaced with the phase shift values measured during the online irradiation test (cf. Sec. 5.2.3). These values were obtained when the MZMs were biased at $-3\,\mathrm{V}$ during the test. The results are shown in Fig. 6.12. The prediction was based on a differential $V_{pp} = 2\,\mathrm{V}$ applied to the SiPh Tx and loss values for passive components as indicated in Fig. 6.10. The plot shows that SiPh-based optical links with a minimum OMA of $-5.2\,\mathrm{dBm}$ would work from 900 kGy (nominal doping and $P_{Las} = 13\,\mathrm{dBm}$) to 1.33 MGy (nominal doping and $P_{Las} = 20\,\mathrm{dBm}$ as well as $2\times$ nominal doping and $P_{Las} = 14\,\mathrm{dBm}$) and 1.74 MGy ($2\times$ nominal doping and $P_{Las} = 20\,\mathrm{dBm}$).

These outcomes demonstrate that SiPh Tx based on shallow etch phase shifters

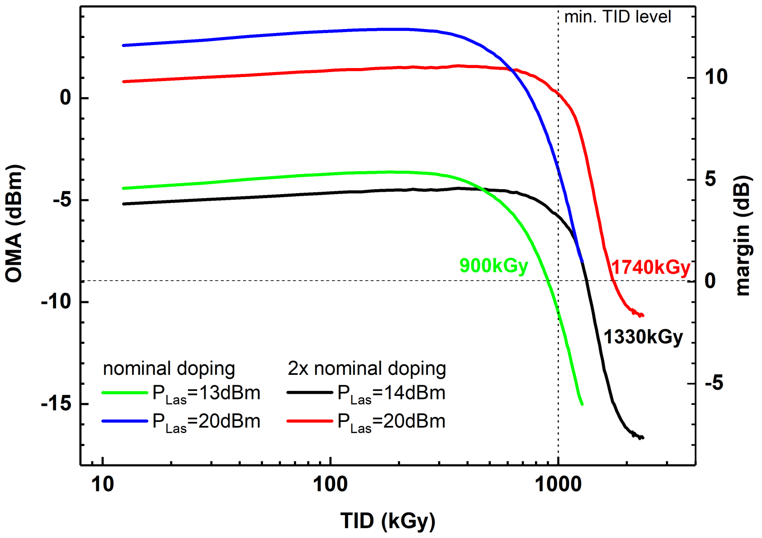

Figure 6.12: OMA and margin of the optical power budget as a function of TID for the proposed SiPh Tx with different doping concentrations and laser powers. A differential $V_{pp} = 2\,\mathrm{V}$ was used for the calculations.

can not only maintain their pre-irradiation phase shift above 50 % up to more than 1 MGy, it would also be possible to have a working system that can provide the minimum required OMA up to 1.7 MGy. It can be imagined that the OMA can be sustained sufficiently high until even higher TID levels based on the above made observations that the phase shift in a cold environment, at lower voltages or when irradiated at a lower dose rate degrades more slowly. SiPh-based optical links that function correctly in harsher radiation environments can thus be expected.

6.4 Estimation of electrical power consumption

The analysis above shows that SiPh-based optical links can withstand TID levels up to 170× and 3.4× higher than components for the VL and VL+ system, respectively, are qualified (cf. Sec. 1.2 & 1.3). The electrical power consumption, however, is also an important figure of merit for an optical link. To determine whether the proposed SiPh-based link can compete with a single-mode VL Tx in this regard, its electrical power consumption was estimated.

The total power consumption in a SiPh Tx consists of the power consumed by the MZM itself, its driver, the quadrature control unit with the monitor PDs and thermo-optic heater as well as the power required to operate the feed-laser. MZMs have virtually no DC power consumption since they are reverse-biased and there is no current flow. However, MZMs consume electrical RF power if they provide high

Table 6.3: Total electrical power consumption for a radiation-hard SiPh MZM-based optical link. The value is compared to a single-mode Tx from the Versatile Link project and a multi-mode Tx from the Versatile Link+ project.

	SiPh Tx (single-mode)	Versatile Link single-mode Tx	Versatile Link+ multi-mode Tx
laser power [mW]	130		
MZM power [mW]	40		
MZM driver power [mW]	320		
photodiode power [mW]	2×30		
heater power [mW]	25		
heater controller [mW]	10		
total power [mW]	**455**	**415**	**50**
bit-rate [Gb/s]	10	4.8	10
energy per bit [pJ/bit]	46	87	5

bit rates and therefore employ electrical transmission lines that are terminated with a load. In a system with an impedance of $Z_0 = 50\,\Omega$ where both arms of an MZM are differentially driven with $V_{pp} = 2\,\mathrm{V}$, i.e. a peak voltage of $V_p = 1\,\mathrm{V}$ is applied to each arm at each time, the total RF power consumption is

$$P_{RF} = 2\frac{V_p^2}{R} = 2\frac{(1\,\mathrm{V})^2}{50\,\Omega} = 40\,\mathrm{mW}. \tag{6.11}$$

The power consumption of a driver circuit for MZMs can be as high as 320 mW [226]. The electrical power needed to induce a phase shift of π, which is enough to adjust the quadrature point, with a thermo-optic heater would be around 25 mW [227]. Since the principle of adjusting the quadrature point in an MZM is the same as the wavelength-stabilization in a ring-modulator, it can be assumed that the power consumption of the radiation-hard circuit for the quadrature controller is also similar. The power consumption of the circuit for the quadrature controller would therefore be in the order of 10 mW [228]. The power consumed by a monitor PD and its transimpedance amplifier (current-to-voltage converter) is up to 30 mW [39]. This yields a total power consumption of 455 mW for a SiPh Tx (Tab. 6.3). The power consumption of the feed-laser, estimated to be 130 mW for an edge-emitting laser that draws a current of 100 mA at 1.3 V, is not included in this number. The reason for this is that the feed-laser would be placed away from the innermost detector regions to avoid damage to it. The heat dissipated by it thus would not need to be transferred away from the innermost region which has to be kept to a temperature below 0 °C. The laser power is clearly needed to run a SiPh-based link. It is however not as critical as if it was dissipated in the detector region that is cooled. The laser power is included in the number for VL and VL+ components, however, as they will be installed with the laser in the innermost detector regions.

The comparison shows that the upper estimation of 455 mW per channel for SiPh-based optical links is only 40 mW higher than the power consumption of a VL single-mode Tx. On the other hand, the power consumption of a VL+ multi-mode Tx is about 400 mW lower than that of a SiPh Tx. This large difference can be attributed to the fact that VCSELs used for VL+ multi-mode Tx can be driven with lower currents than edge-emitting lasers used for VL single-mode Tx. The reduced current requirement also leads to a lower power consumption of the laser driver.

The power consumption of SiPh-based optical links could be further reduced by optimizing the design of the MZM driver as this is the main contributor to the overall power consumption. A driver design for MZMs with a power requirement of only 100 mW was already published [229]. Furthermore, the transmission line and termination load in an MZM could be removed and its design optimized for a lumped operation. In this case, there would be no RF power consumption in the MZM [230] and another 40 mW could be saved. These improvements could bring the total power consumption of a SiPh Tx down to about 200 mW per channel. In addition to the improved radiation hardness, this would make radiation-hard SiPh-based optical links a viable alternative to VCSEL-based optical links for the harshest radiation environments in HEP experiments.

6.5 Summary

Eye diagrams of irradiated and annealed MZMs were compared to eye diagrams of reference samples. Shallow etch MZMs showed no degradation whereas deep etch MZMs could no longer be modulated after irradiation. This was attributed to increased carrier lifetimes that resulted from the radiation-induced pinch-off effect. A model to calculate OMAs was developed and its validity confirmed with measurements. The model was used together with a proposal for a SiPh Tx to predict a working radiation-hard optical link up to a TID of 1.7 MGy. The electrical power consumption of such a link was estimated and found to be similar to the power consumption of single-mode Tx fabricated for the VL system.

7 Conclusions and future work

CERN operates the Large Hadron Collider (LHC) to accelerate and collide charged particles. The particle collisions are detected in large particle detectors that consist of millions of individual sensor channels. The amount of raw data measured by all of these sensor channels is in the order of Tb/s. This data can only be sent efficiently from the radiation-zone within the particle detectors to the processing electronics in the radiation-free counting room through tens of thousands of optical links. The Transceivers (TRx) used for the optical links need to function under very harsh conditions. They need to be able to withstand strong magnetic fields, large temperature variations and extreme radiation levels to send the measurement data reliably. Damage from radiation in the particle detectors is typically the biggest concern for the operation of the optical TRx. Heavy particles can create displacement damage in the atomic lattice of the devices and ionizing radiation can introduce charge trapping and deactivation of dopants. Both damage mechanisms can lead to degradation in the performance of the optical TRx over time and eventually cause the optical links to stop working.

The current- and next generation of optical TRx to be installed in the radiation-zone are custom-made and based on directly-modulated lasers, predominantly multi-mode Vertical Cavity Surface Emitting Lasers (VCSELs). They were qualified to withstand radiation levels high enough for an installation in most regions of the particle detectors. However, the radiation levels in the High Luminosity (HL)-LHC will be so high that VCSELs cannot be used for optical TRx everywhere in future High Energy Physics (HEP) experiments. If VCSELs were installed in the innermost regions of the particle detectors where the highest radiation levels will occur, they would stop working before the end of their required 10-year operational lifetime and measurement data could no longer be sent out. Consequently, a new technology that allows radiation-hard optical links to be installed and reliably operated in the innermost detector regions is needed.

Silicon Photonics (SiPh) is considered a promising candidate for this new technology. This is because silicon has proven itself as a good material for radiation-hard particle sensors. Furthermore, SiPh could allow a highly-integrated detector module including several functions (particle detector, electrical driver, optical TRx) to be envisioned. Such a module could have a lower power consumption, be cheaper, lighter and smaller than current solutions and could thus lead to a paradigm shift in the design of detector read-out systems and radiation-hard optical links in HEP.

SiPh depletion-type Mach-Zehnder Modulators (MZMs) were chosen for investigation as Transmitters (Tx) in radiation-hard optical links. These devices are less sensitive to fabrication and temperature variations than SiPh ring modulators. They should furthermore provide better radiation-hardness than injection- or accumulation-type MZMs. The first irradiation tests of SiPh MZMs with a conventional design have indeed shown that the devices are resistant against a neutron fluence high enough for applications in the HL-LHC. In contrast, the same devices were very sensitive to ionizing radiation and their phase shift vanished before Total Ionizing Dose (TID) levels as those predicted for the HL-LHC were reached. Similar to VCSELs, SiPh MZMs with a conventional design thus cannot be installed in the innermost detector regions of future HEP experiments.

7.1 Main outcomes

This thesis examined how the design of SiPh MZMs could be modified to improve their radiation-hardness such that the innermost detector regions become accessible for radiation-hard optical links. The devices should withstand a TID of at least 1 MGy for that to be achieved. A SiPh test chip containing MZMs with varied design parameters was designed for that purpose. The chip allowed the identification of the design parameters that affect the radiation-hardness of MZMs. Simulations were performed to optimize the phase shift efficiency of the custom-design MZMs on the test chip. The outcomes showed that deep and shallow etch waveguides with a width of 450 nm and a pn-junction being centered in the waveguides were the best design choice to assess the radiation-hardness of MZMs. The chips were fabricated in two versions, with nominal doping and 2× nominal doping concentrations in the pn-junction, in a multi-project wafer run at imec. The chips were found to be fully functional, although their measured phase shifts were higher than initially simulated. The actual doping concentrations used during processing were determined with Van-der-Pauw resistivity measurements. After adjusting the simulations accordingly, a very good agreement between measured and simulated phase shifts was achieved.

Several test chips were irradiated with x-rays to assess the response of the MZMs to ionizing radiation. The temperature in the x-ray irradiator and the bias applied to the MZMs during irradiation were varied for the different tests. The test results demonstrated that shallow etch MZMs withstand more than 10× higher TID levels before their phase shift degraded when compared to deep etch MZMs. All tests also displayed that the phase shifts enhanced up to 30 % before it then degraded.

Increasing the doping concentrations in the pn-junctions of the MZMs also improved the radiation-hardness, particularly for shallow etch MZMs where the difference is larger than for deep etch MZMs.

The phase shift degradation was accelerated when a reverse bias was applied to the MZMs during irradiation. This acceleration was more pronounced when the reverse bias was higher. The faster degradation was attributed to the stronger electric field present in reverse-biased MZM. This leads to more holes escaping prompt recombination after having been created by ionizing radiation. In addition, the velocities at which these holes move through the oxide of the MZMs is faster when the electric field is stronger. Consequently, the radiation-induced damage builds up more rapidly.

In contrast, an irradiation at $-30\,^{\circ}\mathrm{C}$ delayed the phase shift degradation because the mobility of holes is reduced at lower temperatures and so they move slower through the oxide. It hence takes longer to create significant damage in the active silicon layer of the device.

The propagation losses through the doped waveguides of deep etch MZMs decreased during irradiation by approximately 24 % for both doping concentrations.

Some of the radiation-induced damage annealed when the MZMs were heated to 60 °C. Shallow etch MZMs could withstand another significant TID during a second irradiation after annealing. This implies that the dose rate during the test affects the phase shift degradation. It can be assumed that MZMs installed in a HEP experiment can be operated to higher TID levels than those tested for because the actual dose rate would be at least 100× lower (e. g. $0.01 - 0.1\,\mathrm{Gy/s}$ in HL-LHC). Additionally, there would be intermediate breaks during the irradiation. Both would increase the chances that some damage can anneal and the MZMs can withstand the radiation longer.

First results on the radiation hardness of Germanium-on-Silicon photodiodes were also measured. Their dark- and photo-currents were not significantly affected when they were irradiated with x-rays.

Simulating the radiation-induced phase shift degradation in deep etch MZMs quantitatively showed that trapped positive charge in the oxide pushed the free holes out of the p-doped slab region. This caused the free holes in the waveguide rib to become pinched-off from the electrode and carriers could no longer be depleted when a reverse bias was applied. Shallow etch MZMs could not be simulated with the existing model because it did not account for hydrogen-induced dopant passivation. Van-der-Pauw resistivity measurements demonstrated, however, that the doping concentrations were reduced after irradiation. A simulation with reduced doping concentrations further indicated that shallow etch MZMs could be modeled quantitatively if hydrogen-induced dopant passivation were included in the simulations.

The dynamic performance of irradiated MZMs was tested with eye diagram measurements at 10 Gb/s. Eye diagrams of reference and irradiated shallow etch MZMs were virtually identical. In contrast, deep etch MZMs did not show a modulated output signal after irradiation. This was partially attributed to a reduction of the available modulation bandwidth that stemmed from the radiation-induced defects. In addition, the carrier lifetimes in the pinch-off region of the MZMs increased. Thus, it became impossible for deep etch MZMs to produce a 10 Gb/s-modulated signal at its output.

An analytical model to calculate the Optical Modulation Amplitude (OMA) of the measured eye diagrams was developed and verified through measurements. The model was used together with a design proposal for a SiPh Tx to estimate the optical power budget and predict the performance of radiation-hard SiPh-based optical links. The findings indicated that such links could be operated, according the specifications of the single-mode Versatile Link (VL) system that will be installed in 2018, up to 1.7 MGy. Optical links able to withstand even higher TID levels can be imagined when operated at colder temperatures and lower voltages as well as in environments with lower dose rates because each of these conditions slows down the phase shift degradation. Nonetheless, 1.7 MGy already surpassed the minimum target TID of 1 MGy set for SiPh Tx. This would allow the installation of SiPh-based optical links as close as 10 cm from the beam pipe whereas VCSELs or MZMs based on a conventional design could not be installed closer than 17 cm and 25 cm, respectively, from the innermost regions of CMS in HL-LHC (Fig 7.1). Consequently, all sensors of the endcap calorimeter as well as the outer layers of the pixel tracker could now be directly equipped with optical links to read out their measurement data.

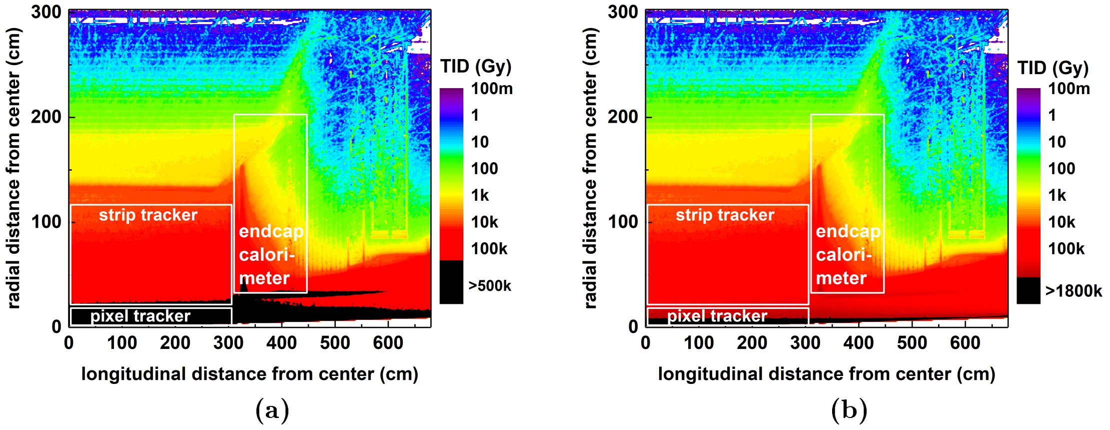

Figure 7.1: Exclusion regions of SiPh MZMs installed in the CMS detector in HL-LHC for devices with a conventional design (a) and after (b) improving the radiation-hardness. The radiation levels in the black areas are too high for the MZMs to be installed in. MZMs with improved radiation-hardness can be installed everywhere in the endcap calorimeter and at the outer parts of the pixel tracker. This was not possible with MZMs based on a conventional design or VCSELs (cf. Fig. 1.6).

The electrical power consumption of the proposed SiPh-based optical links was estimated to be similar to that of the single-mode VL system. The power requirements could be further reduced if the components of the proposed Tx were optimized for low power consumption.

7.2 Future work

Further investigations are required, however, before the full potential of radiation-hard SiPh MZMs is understood. In particular, online irradiation tests of biased MZMs in a cold environment should be carried out to understand the interplay of the accelerated phase shift degradation due to biasing of the MZMs with the delayed degradation when irradiating them at lower temperatures. MZMs should also be irradiated at a lower dose rate to assess how strongly the effect of annealing can counteract the phase shift degradation. These tests will determine the ultimate TID level up to which SiPh MZMs could be used in future HEP experiments.

Besides experimental tests, a revised simulation model would be needed to quantitatively simulate the phase shift degradation of shallow etch MZMs as a function of TID. Adding the transport of radiation-generated holes through the oxide during the transient simulation would be a one possibility to improve the simulation results. The model could then account for the varying carrier velocities when a bias is applied to the phase shifter during irradiation or when the temperature is reduced. Including the mechanism of hydrogen-induced dopant passivation as it most likely occurs in the MZMs could be another way to extend the existing model. For that purpose, the concentration of passivated dopants could e. g. be determined by measuring the change in the doping concentrations of a chip with Van-der-Pauw resistivity measurements during irradiation. Alternatively, the concentration of hydrogen in the active silicon layer before and after radiation by means of Secondary Ion Mass Spectroscopy (SIMS) could be compared. The results could then be used to implement a new simulation model.

Furthermore, knowing the exact energy levels, concentrations and distributions of interface traps and trapped positive charges in irradiated MZMs would be valuable to deepen the understanding of the radiation-induced defects in SiPh devices. This information could allow to find additional means to improve the radiation-hardness of SiPh MZMs.

Figure 7.2 summarizes design suggestions that could already be investigated to improve the radiation hardness of SiPh MZMs further. Having two different etch depths on the p- and n-doped side of the waveguide in a radiation-hard SiPh MZM could be one method to improve the optical performance of these devices. If a deep and shallow etch were employed on the n- and p-doped side, respectively, the optical mode would be better confined than in a shallow etch MZM. In this way, the losses would be lower and the phase modulation efficiency larger while the pinch-off in the p-doped slab region could still be delayed compared to a deep etch MZM.

A similar outcome could probably be achieved if the p-type doping profile were engineered such that the edges of the slab along the interface are higher doped than the center of the slab. Higher TID levels and more trapped positive charge would then be required to push the free holes out of the p-doped slab and create a pinch-off.

Limiting the absolute number of deep traps in the top oxide by growing it only a few nanometers thick could be another approach. Positive charges could then only be trapped in a very thin layer on top of the slab region. The resulting electrostatic repulsion acting upon the free holes in the p-doped slab might not be strong enough to create a pinch-off.

Alternatively, the number of radiation-generated holes that can be trapped in the oxide could potentially be reduced by adding two extra metal electrodes in the oxide. If a voltage is applied to them, they create an electric field which could partially

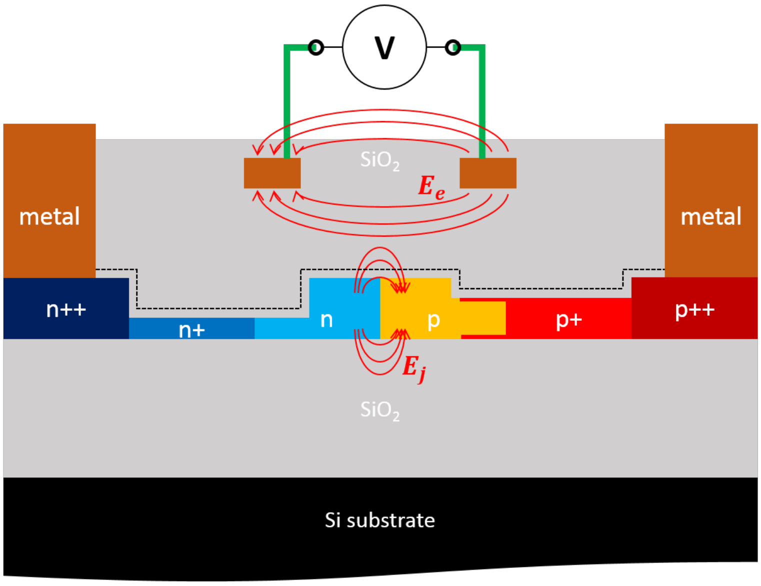

Figure 7.2: Suggestions to improve the radiation-hardness in SiPh MZMs further. A deep etch could be employed on the n-doped side and a shallow etch on the p-doped side to increase the confinement of the optical mode and thus enhance the MZM's performance while still sustaining a high radiation hardness. The edges in the thick slab could also be p+-doped to delay the pinch-off effect. In addition, the top oxide could be grown only a few nm thick (black dashed line) to limit the number of deep traps that could capture holes. Alternatively, two metal electrodes could be placed in the top oxide. By applying a voltage to them, an electric field $\boldsymbol{E_e}$ could partially compensate for the electric field $\boldsymbol{E_j}$ of the pn-junction. This would decrease the yield of holes escaping prompt recombination.

compensate for the electric field created by the pn-junction. Consequently, the local yield of holes escaping prompt recombination as described in Eq. (3.3) would be lower and higher radiation levels were required to produce enough holes that can be trapped and cause a pinch-off.

Lastly, using special radiation-hardened oxides or avoiding excess hydrogen during fabrication could reduce the density of defects in the oxide of the MZMs. The density of deep traps that can capture a hole would then also be reduced and it would possibly be too low to allow for a pinch-off to be created.

The next steps towards testing an actual radiation-hard SiPh-based optical link would have to include the evaluation of the radiation hardness of GeSi photodiodes under neutron irradiation. Neutrons create displacement damage in photodiodes and they eventually stop working. They will be required, however, to withstand the same radiation levels as MZMs. Otherwise, they could not be used for the quadrature control in MZMs and it would not be possible to sustain the optimal working point when modulating the MZMs. If GeSi photodiodes can withstand high enough radiation levels, a SiPh Tx chip would then have to be designed and fabricated. This Tx chip should be connected to a radiation-hard MZM driver to test the dynamic performance of the full Tx under irradiation. Finally, what feed-laser to be used, how to interface it with the SiPh Tx chip and how to manage the polarization in the system would need to be addressed. The last point is particularly important since laser diodes typically emit TE-polarized light while SiPh waveguides can support modes with TE- or TM-polarization. Light with incorrect polarization coupled to a grating coupler on a SiPh Tx chip can cause additional penalties in the optical power budget and thus would need either to be avoided or managed properly.

7.3 Conclusion

The findings from this thesis demonstrate that radiation-hard optical links based on SiPh could withstand higher levels of radiation than optical links based on VCSELs. At the same time they could deliver a similar performance. The MZMs with improved radiation hardness show great potential for installation in the harshest radiation environments in future HEP experiments, e. g. in the Future Circular Collider (FCC) [231] or the Compact Linear Collider (CLIC) [232].

In addition to using radiation-hard SiPh-based optical links to read-out the innermost particle sensors of future HEP experiments, such links could also be employed in the accelerator tunnels where sensors to monitor the particle beams are installed in a radiation environment. The amount of measurement data produced by these sensors can be up to 100 Gb/s. As these data needs to be sent over transmission distances of up to 2 km, this application would especially benefit from the single-mode operation and the possible high bit rates of SiPh.

Silicon photonics is a very promising technology for applications in radiation environments. With the possibility for a very high radiation hardness and the potential for highly-integrated detector read-out modules, it would open up the door for higher resolution physics measurements in future HEP experiments.

Bibliography

[1] M. M. de Abril, J. L. D. R. Melo, C. G. Larrea, J. Hammer, C. Hartl, and C. Lazaridis, "The architecture of the CMS Level-1 Trigger Control and Monitoring System using UML," *Journal of Physics: Conference Series*, vol. 331, no. 2, p. 22020, 2011.

[2] P. Vagata and K. Wilfong, "Scaling the Facebook data warehouse to 300 PB." https://code.facebook.com/posts/229861827208629/scaling-the-facebook-data-warehouse-to-300-pb/, 2014.

[3] CERN, "About CERN." https://test-lhcathome.web.cern.ch/about.

[4] CERN, "CMS detector design." http://cms.web.cern.ch/news/cms-detector-design.

[5] F. Alessio, "Trigger-less readout architecture for the upgrade of the LHCb experiment at CERN," *Journal of Instrumentation*, vol. 8, no. 12, pp. C12019–C12019, 2013.

[6] F. Berghmans, B. Brichard, A. Fernandez, A. Gusarov, M. Uffelen, and S. Girard, "An Introduction to Radiation Effects on Optical Components and Fiber Optic Sensors," in *Optical Waveguide Sensing and Imaging*, pp. 127–165, 2008.

[7] D. Gong, C. Liu, T. Liu, T. Huffman, A. Prosser, J. Troska, F. Vasey, A. Weidberg, A. Xiang, J. Ye, and L. Zhu, "Link model simulation and power penalty specification of the versatile link systems," *Journal of Instrumentation*, vol. 6, no. 01, pp. C01088–C01088, 2011.

[8] A. Xiang, D. Gong, S. Hou, T. Huffman, S. Kwan, K. Liu, T. Liu, A. Prosser, C. Soos, D. Su, P. Teng, J. Troska, F. Vasey, T. Weidberg, and J. Ye, "A Versatile Link for High-Speed, Radiation Resistant Optical Transmission in LHC Upgrades," *Physics Procedia*, vol. 37, pp. 1750–1758, 2012.

[9] L. Olantera, S. Detraz, C. Sigaud, C. Soos, J. Troska, F. Vasey, and M. Zeiler, "Versatile transceiver production and quality assurance," *Journal of Instrumentation*, vol. 12, 2017.

[10] F. Vasey, "The Versatile Link Application Note v2.6." https://espace.cern.ch/project-versatile-link/public/Versatile Link Public Documents/Application Note/Versatile Link Application Note v2.6.pdf, 2015.

[11] E. Guillermain, K. Aikawa, J. Kuhnhenn, D. Ricci, and U. Weinand, "Large-Scale Procurement of Radiation Resistant Single-Mode Optical Fibers for CERN," *Journal of Lightwave Technology*, vol. 33, no. 23, pp. 4878–4884, 2015.

[12] CERN, "The HL-LHC project." http://hilumilhc.web.cern.ch/about/hl-lhc-project.

[13] CMS Collaboration, "FLUKA particle flux maps for CMS Detector." http://cds.cern.ch/record/1612355, oct 2013.

[14] J. Troska, "Versatile Link Technical Specification, Revision No.: 2.1." https://edms.cern.ch/file/1140665/1/VTRx_Spec_v2.1.pdf, 2013.

[15] CMS-Collaboration, "Technical Proposal For The Upgrade Of The CMS Detector Through 2020." https://cds.cern.ch/record/1355706?ln=en, 2011.

[16] F. Vasey, J. Troska, D. Ricci, S. Machado, A. Prosser, T. Huffman, W. Tony, J. Ye, and P. Gui, "The Versatile Link PLUS Project." https://espace.cern.ch/project-Versatile-Link-Plus/Shared Documents/Versatile Link PLUS Project V2.3.pdf, 2015.

[17] C. Soos, S. Detraz, C. Sigaud, J. Troska, F. Vasey, and M. Zeiler, "Versatile Link PLUS Transceiver Development," *Journal of Instrumentation*, vol. 12, no. C03068, 2017.

[18] J. Troska, S. Detraz, S. Seif El Nasr-Storey, P. Stejskal, C. Sigaud, C. Soos, and F. Vasey, "Radiation Damage Studies of Lasers and Photodiodes for Use in Multi-Gb/s Optical Data Links," *IEEE Transactions on*

Nuclear Science, vol. 58, pp. 3103–3110, dec 2011.

[19] S. Seif El Nasr-Storey, S. Detraz, L. Olantera, G. Pezzullo, C. Sigaud, C. Soos, J. Troska, F. Vasey, and M. Zeiler, "Neutron and X-ray Irradiation of Silicon Based Mach-Zehnder Modulators," *Journal of Instrumentation*, vol. 10, 2015.

[20] V. Chiochia and M. Swartz, "Simulation of heavily irradiated silicon pixel sensors and comparison with test beam measurements," *IEEE Transactions on Nuclear Science*, vol. 52, no. 4, pp. 1067–1075, 2005.

[21] J. Zhang, E. Fretwurst, R. Klanner, I. Pintilie, J. Schwandt, and M. Turcato, "Investigation of X-ray induced radiation damage at the Si-SiO2 interface of silicon sensors for the European XFEL," *Journal of Instrumentation*, vol. 7, no. 12, pp. C12012–C12012, 2012.

[22] C. D. Vià, M. Borri, G. D. Betta, I. Haughton, J. Hasi, C. Kenney, M. Povoli, and R. Mendicino, "3D silicon sensors with variable electrode depth for radiation hard high resolution particle tracking," *Journal of Instrumentation*, vol. 10, no. 04, p. C04020, 2015.

[23] N. Savic, L. Bergbreiter, J. Breuer, A. La Rosa, A. Macchiolo, R. Nisius, and S. Terzo, "Thin n-in-p planar pixel modules for the ATLAS upgrade at HL-LHC," *Nuclear Instruments and Methods in Physics Research Section A: Accelerators, Spectrometers, Detectors and Associated Equipment*, 2016.

[24] S. Viel, S. Banerjee, G. Brandt, R. Carney, M. Garcia-Sciveres, A. S. Hard, L. S. Kaplan, L. Kashif, A. Pranko, J. Rieger, J. Wolf, S. L. Wu, and H. Yang, "Performance of silicon pixel detectors at small track incidence angles for the ATLAS Inner Tracker upgrade," *Nuclear Instruments and Methods in Physics Research Section A: Accelerators, Spectrometers, Detectors and Associated Equipment*, vol. 831, pp. 254–259, 2016.

[25] C. Kopp, S. Bernabé, B. B. Bakir, J.-M. Fédéli, R. Orobtchouk, F. Schrank, H. Porte, L. Zimmermann, and T. Tekin, "Silicon photonic circuits: On-CMOS integration, fiber optical coupling, and packaging," *IEEE Journal on Selected Topics in Quantum Electronics*, vol. 17, pp. 498–509, 2011.

[26] J. Ding, H. Chen, L. Yang, and L. Zhang, "Low-voltage, high-extinction-ratio, Mach-Zehnder silicon optical modulator for CMOS compatible integration," in *Conference on Lasers and Electro-Optics*, (San Jose, CA), 2012.

[27] D. A. B. Miller, "Device requirements for optical interconnects to silicon chips," *Proceedings of the IEEE*, vol. 97, pp. 1166–1185, 2009.

[28] A. Biberman and K. Bergman, "Optical interconnection networks for high-performance computing systems.," *Reports on progress in physics. Physical Society (Great Britain)*, vol. 75, p. 046402, 2012.

[29] P. P. Absil, P. Verheyen, P. De Heyn, M. Pantouvaki, G. Lepage, J. De Coster, and J. Van Campenhout, "Silicon photonics integrated circuits: a manufacturing platform for high density, low power optical I/O's.," *Optics express*, vol. 23, no. 7, pp. 9369–78, 2015.

[30] A. Hayakawa, H. Ebe, Y. Chen, and T. Mori, "Silicon Photonics Optical Transceiver for Interconnect," *Fujitsu Scientific & Technical Journal*, vol. 52, no. 1, pp. 19–26, 2016.

[31] D. Thomson, A. Zilkie, J. E. Bowers, T. Komljenovic, G. T. Reed, L. Vivien, D. Marris-Morini, E. Cassan, L. Virot, J.-M. Fédéli, J.-M. Hartmann, J. H. Schmid, D.-X. Xu, F. Boeuf, P. O'Brien, G. Z. Mashanovich, and M. Nedeljkovic, "Roadmap on silicon photonics," *Journal of Optics*, vol. 18, no. 7, p. 073003, 2016.

[32] M. Ahmed et al., "Developments for radiation hard silicon detectors by defect engineering results by the CERN RD48 (ROSE)," *Nuclear Instruments and Methods in Physics Research A*, vol. 465, no. September 2000, pp. 60–69, 2001.

[33] G. Lindström et al., "Radiation hard silicon detectors developments by the RD48 (ROSE) collaboration," *Nuclear Instruments and Methods in Physics Research A*, vol. 466, pp. 308–326, jul 2001.

[34] G. Kramberger, V. Cindro, I. Mandi, V. Cindro, A. Dierlamm, L. Eklund, A. Affolder, M. Havranek, G. Stewart, and R. Bates, "Charge collection studies on custom silicon detectors irradiated up to 1.6E17 neq/cm-2," *Journal of Instrumentation*, vol. 8, 2013.

[35] Z. Li, S. Terzo, L. Andricek, S. Zulaikah, R. Azzahro, M. A. S. Bhuiyan, and M. B. I. Reaz, "Radiation hardness studies of neutron irradiated CMOS sensors fabricated in the ams H18 high voltage process," *Journal of Instrumentation*, vol. 11, 2016.

[36] L. Liao, A. Liu, D. Rubin, J. Basak, and Y. Chetrit, "40 Gbit/s silicon optical modulator for high-speed applications," *Electronics Letters*, vol. 43, no. 22, 2007.

[37] F. Y. Gardes and D. J. Thomson, “40 Gb/s silicon photonics modulator for TE and TM polarisations,” *Optics Express*, vol. 19, pp. 11804–11814, jun 2011.

[38] D. J. Thomson, F. Y. Gardes, J.-M. Fédéli, S. Zlatanovic, Y. Hu, B. Ping, P. Kuo, E. Myslivets, N. Alic, S. Radic, G. Z. Mashanovich, and G. T. Reed, “50-Gb/s silicon optical modulator,” *IEEE Photonics Technology Letters*, vol. 24, no. 4, pp. 234–236, 2012.

[39] J. F. Buckwalter, X. Zheng, G. Li, K. Raj, and A. V. Krishnamoorthy, “A monolithic 25-Gb/s transceiver with photonic ring modulators and ge detectors in a 130-nm CMOS SOI process,” *IEEE Journal of Solid-State Circuits*, vol. 47, no. 6, pp. 1309–1322, 2012.

[40] M. Streshinsky, R. Ding, Y. Liu, A. Novack, Y. Yang, Y. Ma, X. Tu, E. K. S. Chee, A. E.-J. Lim, P. G.-Q. Lo, T. Baehr-Jones, and M. Hochberg, “Low power 50 Gb/s silicon traveling wave Mach-Zehnder modulator near 1300 nm,” *Optics Express*, vol. 21, pp. 30350–30357, dec 2013.

[41] T. Baba and S. Akiyama, “Low-$\alpha V\pi L$ 25-Gb/s silicon modulator based on forward-biased pin diodes,” in *11th International Conference on Group IV Photonics (GFP)*, vol. 3, pp. 30–31, 2014.

[42] D. M. Gill, J. E. Proesel, C. Xiong, J. S. Orcutt, J. C. Rosenberg, M. H. Khater, T. Barwicz, S. Assefa, S. M. Shank, C. Reinholm, J. Ellis-Monaghan, E. Kiewra, S. Kamlapurkar, C. M. Breslin, W. M. J. Green, W. Haensch, and Y. A. Vlasov, “Demonstration of a high extinction ratio monolithic CMOS integrated nanophotonic transmitter and 16 Gb/s optical link,” *IEEE Journal on Selected Topics in Quantum Electronics*, vol. 21, no. 4, 2015.

[43] C. Xiong, D. Gill, J. Proesel, J. Orcutt, W. Haensch, and W. M. J. Green, “A Monolithic 56 Gb / s CMOS Integrated Nanophotonic PAM-4 Transmitter,” in *IEEE Optical Interconnects Conference*, vol. 3, pp. 111–112, 2015.

[44] D. Mahgerefteh and C. Thompson, “Techno-economic Comparison of Silicon Photonics and Multimode VCSELs,” *Journal of Lightwave Technology*, vol. 34, no. 2, pp. 2014–2016, 2016.

[45] A. Boletti, D. Giacomuzzi, G. Parladori, P. Boffi, M. Ferrario, and M. Martinelli, “Performance comparison between electrical copper-based and optical fiber-based backplanes.,” *Optics express*, vol. 21, no. 16, pp. 19202–8, 2013.

[46] M. Rakowski, M. Pantouvaki, P. De Heyn, P. Verheyen, M. Ingels, H. Chen, J. De Coster, G. Lepage, B. Snyder, K. De Meyer, M. Steyaert, N. Pavarelli, J. Su Lee, P. O’Brien, P. Absil, and J. Van Campenhout, “A 4x20Gb/s WDM Ring-Based Hybrid CMOS Silicon Photonics Transceiver,” in *IEEE International Solid-State Circuits Conference*, pp. 408–410, 2015.

[47] P. Skwierawski, M. Schneider, D. Karnick, L. Eisenblätter, and M. Weber, “A silicon photonic wavelength division multiplex system for high-speed data transmission in detector instrumentation,” *Journal of Instrumentation*, vol. 11, 2016.

[48] D. Marris-Morini, L. Virot, C. Baudot, J.-M. Fédéli, G. Rasigade, D. Perez-Galacho, J.-M. Hartmann, S. Olivier, P. Brindel, P. Crozat, F. Bœuf, and L. Vivien, “A 40 Gbit/s optical link on a 300-mm silicon platform,” *Optics Express*, vol. 22, p. 6674, mar 2014.

[49] S. Seif El Nasr-Storey, S. Detraz, L. Olantera, C. Sigaud, C. Soos, J. Troska, and F. Vasey, “Irradiation of new optoelectronic components for HL-LHC data transmission links,” *Journal of Instrumentation*, vol. 8, dec 2013.

[50] S. Seif El Nasr-Storey, F. Boeuf, C. Baudot, S. Detraz, J. M. Fedeli, D. Marris-Morini, L. Olantera, G. Pezzullo, C. Sigaud, C. Soos, J. Troska, F. Vasey, L. Vivien, M. Zeiler, and M. Ziebell, “Silicon Photonics for High Energy Physics Data Transmission Applications,” in *IEEE 11th International Conference on Group IV Photonics (GFP)*, (Paris), pp. 1–2, 2014.

[51] S. Seif El Nasr-Storey, F. Boeuf, C. Baudot, S. Detraz, J. M. Fedeli, D. Marris-Morini, L. Olantera, G. Pezzullo, C. Sigaud, C. Soos, J. Troska, F. Vasey, L. Vivien, M. Zeiler, and M. Ziebell, “Effect of radiation on a Mach-Zehnder interferometer silicon modulator for HL-LHC data transmission applications,” *IEEE Transactions on Nuclear Science*, vol. 62, no. 1, pp. 329–335, 2015.

[52] S. Seif El Nasr-Storey, *Radiation-hard Optoelectronics for LHC detector upgrades.* PhD thesis, Bristol University, 2016.

[53] D. J. Thomson, F. Y. Gardes, and Y. Hu, “High contrast 40Gbit/s optical modulation in silicon,” *Optics Express*, vol. 19, no. 12, pp. 11507–11516, 2011.

[54] Y. Zhang, A. Hosseini, and J. Ahn, “Silicon based double-layer 1x12 multimode interference coupler for

three-dimensional photonic integration," in *Optical Interconnects Conference*, vol. 4, (Santa Fe, NM), 2012.

[55] M. Aamer, D. J. Thomson, A. Gutiérrez, A. Brimont, F. Y. Gardes, G. T. Reed, J.-M. Fédéli, A. Hakansson, and P. Sanchis, "10Gbit/s error-free DPSK modulation using a push-pull dual-drive silicon modulator," *Optics Communications*, vol. 304, pp. 107–110, sep 2013.

[56] B. Milivojevic, J. Whiteaway, S. Wiese, C. Raabe, A. Shastri, M. Webster, P. Metz, S. Sunder, B. Chattin, S. P. Anderson, B. Dama, K. Shastri, and C. Muzio, "Design challenges of next generation coherent systems using Silicon photonics high-speed modulator," in *11th International Conference on Group IV Photonics (GFP)*, vol. 6, pp. 11–12, IEEE, aug 2014.

[57] D. Petousi, L. Zimmermann, A. Gajda, M. Kroh, K. Voigt, G. Winzer, B. Tillack, and K. Petermann, "Analysis of optical and electrical tradeoffs of traveling-wave depletion-type Si Mach-Zehnder modulators for high-speed operation," *IEEE Journal on Selected Topics in Quantum Electronics*, vol. 21, no. 4, 2015.

[58] A. Liu, L. Liao, D. Rubin, and H. Nguyen, "High-speed optical modulation based on carrier depletion in a silicon waveguide," *Optics Express*, vol. 15, no. 2, pp. 660–668, 2007.

[59] C. Gunn, "Fully integrated VLSI CMOS and photonics," *Digest of Technical Papers - Symposium on VLSI Technology*, vol. 3, pp. 6–9, 2007.

[60] G. Masini, S. Sahni, G. Capellini, J. Witzens, and C. Gunn, "High-speed near infrared optical receivers based on Ge waveguide photodetectors integrated in a CMOS process," *Advances in Optical Technologies*, vol. 2008, 2008.

[61] D. M. Gill, W. M. Green, C. Xiong, J. E. Proesel, A. V. Rylyakov, C. L. Schow, J. Rosenberg, T. Barwicz, M. Khater, S. Assefa, S. Shank, C. Reinholm, E. Kiewra, S. Kamlapurkar, and Y. Vlasov, "Distributed Electrode Mach-Zehnder Modulator with Double-Pass Phase Shifters and Integrated Inductors," in *Conference on Lasers and Electro-Optics*, (Washington, D.C.), Osa, 2014.

[62] A. Shastri, C. Muzio, M. Webster, G. Jeans, P. Metz, S. Sunder, B. Chattin, B. Dama, and K. Shastri, "Ultra-low-power single-polarization QAM-16 generation without DAC using a CMOS photonics based segmented modulator," *Journal of Lightwave Technology*, vol. 33, no. 6, pp. 1255–1260, 2015.

[63] F. Boeuf, S. Cremer, E. Temporiti, M. Fere, M. Shaw, N. Vulliet, B. Orlando, D. Ristoiu, A. Farcy, A. Mekis, G. Masini, P. Sun, Y. Chi, H. Petiton, S. Jan, J.-R. Manouvrier, C. Baudot, P. Le Maitre, J.-F. Carpentier, L. Salager, M. Traldi, L. Maggi, D. Rigamonti, C. Zaccherini, and C. Elemi, "Recent Progress in Silicon Photonics R&D and Manufacturing on 300mm Wafer Platform," *Optical Fiber Communication Conference*, vol. 34, no. 2, pp. 4–6, 2015.

[64] M. R. Lee and P. M. Fauchet, "Two-dimensional silicon photonic crystal based biosensing platform for protein detection.," *Optics express*, vol. 15, no. 8, pp. 4530–4535, 2007.

[65] Y. Sun and X. Fan, "Optical ring resonators for biochemical and chemical sensing," *Analytical and Bioanalytical Chemistry*, vol. 399, no. 1, pp. 205–211, 2011.

[66] I. A. Estrada, R. W. Burlingame, A. P. Wang, K. Chawla, T. Grove, J. Wang, S. O. Southern, M. Iqbal, L. C. Gunn, and M. A. Gleeson, "Multiplex detection of pathogen biomarkers in human blood, serum, and saliva using silicon photonic microring resonators," *Proc. SPIE: Advances in Global Health through Sensing Technologies*, vol. 9490, pp. 94900E–94900E–14, 2015.

[67] A. L. Washburn, W. W. Shia, K. A. Lenkeit, S.-H. Lee, and R. C. Bailey, "Multiplexed cancer biomarker detection using chip-integrated silicon photonic sensor arrays," *Analyst*, vol. 141, no. 18, pp. 5358–5365, 2016.

[68] A. Densmore, D. X. Xu, P. Waldron, S. Janz, P. Cheben, J. Lapointe, A. Delâge, B. Lamontagne, J. H. Schmid, and E. Post, "A silicon-on-insulator photonic wire based evanescent field sensor," *IEEE Photonics Technology Letters*, vol. 18, no. 23, pp. 2520–2522, 2006.

[69] C. Lee and J. Thillaigovindan, "Optical nanomechanical sensor using a silicon photonic crystal cantilever embedded with a nanocavity resonator.," *Applied optics*, vol. 48, no. 10, pp. 1797–1803, 2009.

[70] G. T. Reed and A. P. Knights, *Silicon Photonics: An Introduction.* John Wiley & Sons, 2004.

[71] B. E. A. Saleh and M. C. Teich, *Fundamentals of Photonics.* Wiley Series in Pure and Applied Optics, Wiley, 2007.

[72] A. Liu, F. Gardes, L. Liao, R. Schaevitz, G. Reed, and M. Paniccia, "Silicon High-Speed Modulators," in *Broadband Optical Modulators*, pp. 257–280, CRC Press, nov 2011.

[73] M. Deen and P. Basu, *Silicon Photonics: Fundamentals and Devices.* Wiley, 2012.

[74] L. Pavesi and L. Vivien, *Handbook of Silicon Photonics.* CRC Press, 2013.

[75] Y. Vlasov and S. McNab, "Losses in single-mode silicon-on-insulator strip waveguides and bends.," *Optics express*, vol. 12, no. 8, pp. 1622–1631, 2004.

[76] I. Kiyat and A. Aydinli, "High-Q silicon-on-insulator optical rib waveguide racetrack resonators," *Optics Express*, vol. 13, no. 6, pp. 1900–5, 2005.

[77] K. Yamada, "Silicon Photonic Wire Waveguides: Fundamentals and Applications," in *Silicon Photonics II: Components and Integration* (D. J. Lockwood and L. Pavesi, eds.), pp. 1–29, Springer, 2011.

[78] G. Ghosh, *Handbook of Optical Constants of Solids: Handbook of Thermo-Optic Coefficients of Optical Materials with Applications.* Handbook of optical constants of solids, Elsevier Science, 1998.

[79] G. Cocorullo, F. G. D. Corte, and I. Rendina, "Temperature dependence of the thermo-optic coefficient in crystalline silicon between room temperature and 550 K at the wavelength of 1523 nm," *Applied Physics Letters*, vol. 74, no. 22, pp. 3338–3340, 1999.

[80] C. T. DeRose, M. R. Watts, R. W. Young, D. C. Trotter, G. N. Nielson, W. A. Zortman, and R. D. Kekatpure, "Low power and broadband 2x2 silicon thermo-optic switch," *2011 Optical Fiber Communication Conference and Exposition and the National Fiber Optic Engineers Conference*, pp. 1–3, 2011.

[81] A. Masood, M. Pantouvaki, D. Goossens, G. Lepage, P. Verheyen, J. Van Campenhout, P. Absil, D. Van Thourhout, and W. Bogaerts, "Fabrication and characterization of CMOS-compatible integrated tungsten heaters for thermo-optic tuning in silicon photonics devices," *Optical Materials Express*, vol. 4, no. 7, p. 1383, 2014.

[82] G. Li, X. Zheng, J. Yao, H. Thacker, I. Shubin, Y. Luo, K. Raj, J. E. Cunningham, and A. V. Krishnamoorthy, "High-efficiency 25Gb/s CMOS ring modulator with integrated thermal tuning," in *IEEE International Conference on Group IV Photonics GFP*, pp. 8–10, 2011.

[83] K. Padmaraju and K. Bergman, "Resolving the thermal challenges for silicon microring resonator devices," *Nanophotonics*, vol. 3, no. 4-5, pp. 269–281, 2014.

[84] S. Lin, X. Zheng, P. Amberg, S. S. Djordjevic, J. H. Lee, I. Shubin, J. Yao, Y. Luo, J. Bovington, D. Y. Lee, H. D. Thacker, J. E. Cunningham, K. Raj, and A. V. Krishnamoorthy, "Wavelength Locked High-speed Microring Modulator Using an Integrated Balanced Homodyne CMOS Control Circuit," in *Optical Fiber Communication Conference*, Optical Society of America, 2016.

[85] R. Soref and B. Bennett, "Electrooptical effects in silicon," *IEEE Journal of Quantum Electronics*, vol. 23, pp. 123–129, jan 1987.

[86] J. Liu, D. Pan, S. Jongthammanurak, K. Wada, L. C. Kimerling, and J. Michel, "Design of monolithically integrated GeSi electro-absorption modulators and photodetectors on a SOI platform," *Optics Express*, vol. 15, no. 2, pp. 623–628, 2007.

[87] Y. M. Li, Z. Liu, C. L. Xue, C. B. Li, B. W. Cheng, and Q. M. Wang, "Design of an evanescent-coupled GeSi electro-absorption modulator based on Franz-Keldysh effect," *Acta Physica Sinica*, vol. 62, no. 11, p. 5, 2013.

[88] N. Abadía, T. Bernadin, P. Chaisakul, S. Olivier, D. Marris-Morini, R. Espiau de Lamaëstre, J. C. Weeber, and L. Vivien, "Low-Power consumption Franz-Keldysh effect plasmonic modulator," *Optics Express*, vol. 22, no. 9, p. 11236, 2014.

[89] N. Abadia and S. Olivier, "A CMOS-compatible Franz-Keldysh effect plasmonic modulator," in *11th International Conference on Group IV Photonics (GFP)*, vol. 12, pp. 63–64, 2014.

[90] R. Soref and B. Bennett, "Kramers-Kronig analysis of electro-optical switching in silicon," in *SPIE 0704, Integrated Optical Circuit Engineering IV*, (Cambridge, MA), 1987.

[91] K. Kusová, P. Hapala, J. Valenta, P. Jelínek, O. Cibulka, L. Ondič, and I. Pelant, "Direct Bandgap Silicon: Tensile Strained Silicon Nanocrystals," *Advanced Materials Interfaces*, vol. 1, no. 2, pp. 1300042—-n/a, 2014.

[92] B. Dutt, D. S. Sukhdeo, D. Nam, B. M. Vulovic, Z. Yuan, and K. C. Saraswat, "Roadmap to an Efficient Germanium-on-Silicon Laser: Strain vs. n-Type Doping," *IEEE Photonics Journal*, vol. 4, pp. 2002–2009, oct 2012.

[93] Z. Zhou, B. Yin, and J. Michel, “On-chip light sources for silicon photonics,” *Light: Science & Applications*, vol. 4, pp. 1–13, 2015.

[94] M. M. J. R. Heck, H.-W. Chen, A. A. W. Fang, B. R. B. Koch, D. Liang, H. Park, M. M. N. Sysak, and J. J. E. Bowers, “Hybrid Silicon Photonics for Optical Interconnects,” *Selected Topics in Quantum Electronics, IEEE Journal of*, vol. 17, no. 2, pp. 333 –346, 2011.

[95] S. Keyvaninia, G. Roelkens, D. V. Thourhout, C. Jany, M. Lamponi, A. L. Liepvre, F. Lelarge, D. Make, G.-H. Duan, D. Bordel, and J.-M. Fedeli, “Demonstration of a heterogeneously integrated III-V/SOI single wavelength tunable laser,” *Opt. Express*, vol. 21, pp. 3784–3792, feb 2013.

[96] Y. De Koninck, G. Roelkens, and R. Baets, “Electrically pumped 1550 nm single mode III-V-on-silicon laser with resonant grating cavity mirrors,” *Laser & Photonics Reviews*, vol. 9, no. 2, pp. L6 – L10, 2015.

[97] B. R. Koch, E. J. Norberg, B. Kim, J. Hutchinson, J. H. Shin, G. Fish, and A. Fang, “Integrated Silicon Photonic Laser Sources for Telecom and Datacom,” in *2013 Optical Fiber Communication Conference and Exposition and the National Fiber Optic Engineers Conference (OFC/NFOEC)*, pp. 1–3, mar 2013.

[98] T. Baehr-Jones, R. Ding, Y. Liu, and A. Ayazi, “Ultralow drive voltage silicon traveling-wave modulator,” *Optics Express*, vol. 20, no. 11, pp. 12014–12020, 2012.

[99] C. DeRose and D. Trotter, “High speed travelling wave carrier depletion silicon Mach-Zehnder modulator,” in *Optical Interconnects Conference*, (Santa Fe, NM), pp. 135–136, 2012.

[100] S. Manipatruni, Q. Xu, B. Schmidt, J. Shakya, and M. Lipson, “High Speed Carrier Injection 18 Gb/s Silicon Micro-ring Electro-optic Modulator,” *LEOS 2007 - IEEE Lasers and Electro-Optics Society Annual Meeting Conference Proceedings*, pp. 537–538, oct 2007.

[101] D. Perez-Galacho, D. Marris-Morini, C. Baudot, J.-M. Fédéli, N. Vulliet, A. Souhaité, S. Olivier, X. L. Roux, F. Boeuf, and L. Vivien, “40Gbit/s silicon ring resonator-based modulator fabricated on 300mm SOI wafers,” in *11th International Conference on Group IV Photonics (GFP)*, vol. 5, pp. 49–50, 2014.

[102] K. Bédard, A. D. Simard, B. Filion, Y. Painchaud, L. A. Rusch, and S. LaRochelle, “Dual phase-shift Bragg grating silicon photonic modulator operating up to 60 Gb/s,” *Opt. Express*, vol. 24, pp. 2413–2419, feb 2016.

[103] D. Feng, S. Liao, H. Liang, J. Fong, B. Bijlani, R. Shafiiha, B. J. Luff, Y. Luo, J. Cunningham, A. V. Krishnamoorthy, and M. Asghari, “High speed GeSi electro-absorption modulator at 1550 nm wavelength on SOI waveguide,” *Optics Express*, vol. 20, p. 22224, sep 2012.

[104] S. Gupta, S. A. Srinivasan, M. Pantouvaki, H. Chen, P. Verheyen, G. Lepage, and D. V. Thourhout, “50GHz Ge Waveguide Electro-Absorption Modulator Integrated in a 220nm SOI Photonics Platform,” in *Optical Fiber Communication Conference*, 2015.

[105] S. Papadopoulos, S. Seif El Nasr-Storey, J. Troska, I. Papakonstantinou, F. Vasey, and I. Darwazeh, “Component and system level studies of radiation damage impact on reflective electroabsorption modulators for use in HL-LHC Data transmission,” *IEEE Transactions on Nuclear Science*, vol. 60, no. 1, pp. 386–393, 2013.

[106] L. Soldano and E. Pennings, “Optical multi-mode interference devices based on self-imaging: principles and applications,” *Journal of Lightwave Technology*, vol. 13, pp. 615–627, apr 1995.

[107] H.-W. Chen and A. Poon, “Low-loss multimode-interference-based crossings for silicon wire waveguides,” *IEEE Photonics Technology Letters*, vol. 18, pp. 2260–2262, nov 2006.

[108] D. J. Thomson, Y. Hu, G. T. Reed, and J.-M. Fédéli, “Low Loss MMI Couplers for High Performance MZI Modulators,” *IEEE Photonics Technology Letters*, vol. 22, pp. 1485–1487, oct 2010.

[109] J. Basak, L. Liao, A. Liu, D. Rubin, Y. Chetrit, H. Nguyen, D. Samara-Rubio, R. Cohen, N. Izhaky, and M. Paniccia, “Developments in gigascale silicon optical modulators using free carrier dispersion mechanisms,” *Advances in Optical Technologies*, vol. 2008, 2008.

[110] G. Rasigade, D. Marris-Morini, M. Ziebell, E. Cassan, and L. Vivien, “Analytical model for depletion-based silicon modulator simulation,” *Optics Express*, vol. 19, pp. 3919–39124, feb 2011.

[111] J. Svarny, “Analysis of quadrature bias-point drift of Mach-Zehnder electro-optic modulator,” in *12th Biennial Electronics Conference (BEC)*, (Tallinn, Estonia), pp. 231–234, 2010.

[112] S. Akiyama, T. Baba, and M. Imai, “12.5-Gb/s operation with 0.29Vcm VπL using silicon Mach-Zehnder

modulator based-on forward-biased pin diode," *Optics Express*, vol. 20, no. 3, pp. 20876–20885, 2012.

[113] F. Lemeilleur, M. Glaser, E. Heijne, P. Jarron, and E. Occelli, "Neutron-induced radiation damage in silicon detectors," *IEEE Transactions on Nuclear Science*, vol. 39, no. 4, pp. 551–557, 1992.

[114] A. Liu, R. Jones, L. Liao, D. Samara-Rubio, D. Rubin, O. Cohen, R. Nicolaescu, and M. Paniccia, "A high-speed silicon optical modulator based on a metalâĂŞoxideâĂŞsemiconductor capacitor," *Nature*, vol. 427, pp. 615–618, feb 2004.

[115] M. Webster and P. Gothoskar, "An efficient MOS-capacitor based silicon modulator and CMOS drivers for optical transmitters," in *11th International Conference on Group IV Photonics (GFP)*, vol. 1, pp. 30–31, 2014.

[116] A. Liu, L. Liao, D. Rubin, J. Basak, Y. Chetrit, H. Nguyen, R. Cohen, N. Izhaky, and M. Paniccia, "Recent development in a high-speed silicon optical modulator based on reverse-biased pn diode in a silicon waveguide," *Semiconductor Science and Technology*, vol. 23, p. 064001, jun 2008.

[117] H. Yu, M. Pantouvaki, J. Van Campenhout, D. Korn, K. Komorowska, P. Dumon, Y. Li, P. Verheyen, P. Absil, L. Alloatti, D. Hillerkuss, J. Leuthold, R. Baets, and W. Bogaerts, "Performance tradeoff between lateral and interdigitated doping patterns for high speed carrier-depletion based silicon modulators.," *Optics Express*, vol. 20, pp. 12926–38, jun 2012.

[118] M. Ziebell, D. Marris-Morini, G. Rasigade, J.-M. Fédéli, P. Crozat, E. Cassan, D. Bouville, and L. Vivien, "40 Gbit/s low-loss silicon optical modulator based on a pipin diode," *Optics Express*, vol. 20, pp. 10591–10596, may 2012.

[119] D. J. Thomson, F. Y. Gardes, and S. Liu, "High Performance Mach-Zehnder-Based Silicon Optical Modulators," *IEEE Journal of Selected Topics in Quantum Electronics*, vol. 19, no. 6, 2013.

[120] T. Cao, Y. Fei, L. Zhang, Y. Cao, and S. Chen, "Design of a silicon Mach-Zehnder modulator with a U-type PN junction," *Applied Optics*, vol. 52, no. 24, pp. 5941–5948, 2013.

[121] H. Yu, "Optimization of ion implantation condition for depletion-type silicon optical modulators," *IEEE Journal of Quantum Electronics*, vol. 46, no. 12, pp. 1763–1768, 2010.

[122] D. Patel, S. Ghosh, M. Chagnon, A. Samani, V. Veerasubramanian, M. Osman, and D. V. Plant, "Design, analysis, and transmission system performance of a 41 GHz silicon photonic modulator," *Optics Express*, vol. 23, no. 11, pp. 1789–1796, 2015.

[123] I. Goykhman, B. Desiatov, and S. Ben Ezra, "Optimization of efficiency-loss figure of merit in carrier-depletion silicon Mach-Zehnder optical modulator," *Optics Express*, vol. 21, no. 17, pp. 7994–7999, 2013.

[124] C. T. DeRose, D. C. Trotter, W. A. Zortman, A. L. Starbuck, M. Fisher, M. R. Watts, and P. S. Davids, "Ultra compact 45 GHz CMOS compatible Germanium waveguide photodiode with low dark current," *Opt. Express*, vol. 19, pp. 24897–24904, dec 2011.

[125] H. T. Chen, P. Verheyen, P. D. Heyn, G. Lepage, J. D. Coster, P. Absil, G. Roelkens, and J. V. Campenhout, "High-Responsivity Low-Voltage 28-Gb/s Ge p-i-n Photodetector With Silicon Contacts," *J. Lightwave Technol.*, vol. 33, pp. 820–824, feb 2015.

[126] L. Vivien, A. Polzer, D. Marris-Morini, J. Osmond, J. M. Hartmann, P. Crozat, E. Cassan, C. Kopp, H. Zimmermann, and J. M. Fédéli, "Zero-bias 40Gbit/s germanium waveguide photodetector on silicon," *Optics Express*, vol. 20, no. 2, p. 1096, 2012.

[127] E. Temporiti, G. Minoia, M. Repossi, D. Baldi, A. Ghilioni, and F. Svelto, "A 3D-integrated 25Gbps silicon photonics receiver in PIC25G and 65nm CMOS technologies," in *ESSCIRC 2014 - 40th European Solid State Circuits Conference (ESSCIRC)*, pp. 131–134, IEEE, sep 2014.

[128] L. Vivien, D. Marris-Morini, L. Virot, D. Perez-Galacho, G. Rasigade, J. M. Hartmann, E. Cassan, P. Crozat, S. Olivier, C. Baudot, F. Boeuf, and J.-M. Fedeli, "High speed silicon-based optoelectronic devices on 300mm platform," in *2014 16th International Conference on Transparent Optical Networks (ICTON)*, pp. 1–4, jul 2014.

[129] A. Ruzin, G. Casse, M. Glaser, A. Zanet, F. Lemeilleur, and S. Watts, "Comparison of radiation damage in silicon induced by proton and neutron irradiation," *IEEE Transactions on Nuclear Science*, vol. 46, no. 5, pp. 1310–1313, 1999.

[130] T. Oldham, K. Bennett, J. Beaucour, T. Carriere, C. Polvey, and P. Garnier, "Total dose failures in advanced electronics from single ions," *IEEE Transactions on Nuclear Science*, vol. 40, no. 6, pp. 1820–1830,

1993.

[131] G. Swift, D. Padgett, and A. Johnston, “A new class of single event hard errors [DRAM cells],” *IEEE Transactions on Nuclear Science*, vol. 41, pp. 2043–2048, dec 1994.

[132] P. Dodd, M. Shaneyfelt, J. Felix, and J. Schwank, “Production and propagation of single-event transients in high-speed digital logic ICs,” *IEEE Transactions on Nuclear Science*, vol. 51, pp. 3278–3284, dec 2004.

[133] F. B. McLean and T. R. Oldham, “Basic mechanisms of radiation effects in electronic materials and devices,” *Harry Diamond Lab. Tech. Rep.*, vol. HDL-TR, p. 2129, 1987.

[134] M. Moll, *Radiation Damage in Silicon Particle Detectors.* PhD thesis, Hamburg University, 1999.

[135] G. Lindström et al., “Radiation hardness of silicon detectors - a challenge from high-energy physics,” *Nuclear Instruments and Methods in Physics Research A*, vol. 426, pp. 1–15, apr 1999.

[136] C. Claeys and E. Simoen, *Radiation effects in advanced semiconductor materials and devices.* 2002.

[137] C. Nicklaw, *Multi-Level Modeling of Total Ionizing Dose in a-SiO2: First Principles to Circuits.* PhD thesis, 2003.

[138] H. J. Barnaby, “Total-ionizing-dose effects in modern CMOS technologies,” *IEEE Transactions on Nuclear Science*, vol. 53, no. 6, pp. 3103–3121, 2006.

[139] M. Bagatin and S. Gerardin, *Ionizing Radiation Effects in Electronics.* CRC Press, 2015.

[140] J. Srour, C. Marshall, and P. Marshall, “Review of displacement damage effects in silicon devices,” *IEEE Transactions on Nuclear Science*, vol. 50, no. 3, pp. 653–670, 2003.

[141] C. Poivey and G. Hopkinson, “Displacement Damage Mechanism and Effects.” http://space.epfl.ch/webdav/site/space/shared/industry_media/05 DD issue3.pdf, 2009.

[142] M. Huhtinen, “Simulation of non-ionising energy loss and defect formation in silicon,” *Nuclear Instruments and Methods in Physics Research, Section A: Accelerators, Spectrometers, Detectors and Associated Equipment*, vol. 491, no. 1-2, pp. 194–215, 2002.

[143] P. Fernández-Martínez, “Simulation of total ionising dose in MOS capacitors,” *Proceedings of the 8th Spanish Conference on Electron Devices, CDE'2011*, 2011.

[144] P. Paillet, J. L. Touron, J. L. Leray, C. Cirba, and I. Introduction, “Simulation of Multi-Level Radiation-Induced Charge Trapping and Thermally Activated Phenomena in SiO2,” *IEEE Transactions on Nuclear Science*, vol. 45, no. 3, pp. 1379–1384, 1998.

[145] E. J. Katz, Z. Zhang, H. L. Hughes, K. B. Chung, G. Lucovsky, and L. J. Brillson, “Nanoscale depth-resolved electronic properties of SiO2/SiO/iO2 for device-tolerant electronics,” *Journal of Vacuum Science & Technology B: Microelectronics and Nanometer Structures*, vol. 29, no. 1, 2011.

[146] H. Barnaby, M. McLain, I. Esqueda, and X. J. C. X. J. Chen, “Modeling Ionizing Radiation Effects in Solid State Materials and CMOS Devices,” *IEEE Transactions on Circuits and Systems I: Regular Papers*, vol. 56, no. 8, pp. 1870–1883, 2009.

[147] C. J. Nicklaw, Z. Y. Lu, D. M. Fleetwood, R. D. Schrimpf, and S. T. Pantelides, “The structure, properties, and dynamics of oxygen vacancies in amorphous SiO2,” *IEEE Transactions on Nuclear Science*, vol. 49 I, no. 6, pp. 2667–2673, 2002.

[148] D. M. Fleetwood, H. D. Xiong, S. Member, Z. Lu, C. J. Nicklaw, J. a. Felix, R. D. Schrimpf, and S. T. Pantelides, “Unified Model of Hole Trapping , 1/f Noise , and Thermally Stimulated Current in MOS Devices,” *IEEE Transactions on Nuclear Science*, vol. 49, no. 6, pp. 2674–2683, 2002.

[149] D. M. Fleetwood and J. H. Scofield, “Evidence that similar point defects cause 1/f noise and radiation-induced-hole trapping in metal-oxide-semiconductor transistors,” *Physical Review Letters*, vol. 64, no. 5, pp. 579–582, 1990.

[150] T. Uchida, M. Takahashi, and T. Yoko, “Model of a switching oxide trap in amorphous silicon dioxide,” *Physical Review B*, vol. 64, p. 081310, aug 2001.

[151] J. Schwandt, E. Fretwurst, R. Klanner, I. Pintilie, and J. Zhang, “Optimization of the radiation hardness of silicon pixel sensors for high x-ray doses using TCAD simulations,” *Journal of Instrumentation*, vol. 7,

no. 01, pp. C01006–C01006, 2012.

[152] E. Snow, A. Grove, and D. J. Fitzgerald, “Effects of Ionizing Radiation on Oxidized Silicon Surfaces and Planar Devices,” *Proceedings of the IEEE*, vol. 55, no. 7, pp. 1168–1185, 1967.

[153] J. Mitchell, “Radiation-induced space-charge buildup in MOS structures,” *IEEE Transactions on Electron Devices*, vol. 14, no. 11, 1967.

[154] J. Schwank, “Basic mechanisms of radiation effects in the natural space radiation environment,” tech. rep., 1994.

[155] F. B. McLean, “A Framework for Understanding Radiation-Induced Interface States in SiO2 MOS Structures,” *IEEE Transactions on Nuclear Science*, vol. 27, no. 6, pp. 1651–1657, 1980.

[156] P. Lenahan, J. Mele, J. Conley, J.F., R. Lowry, and D. Woodbury, “Predicting radiation response from process parameters: Verification of a physically based predictive model,” *IEEE Transactions on Nuclear Science*, vol. 46, no. 6, 1999.

[157] J. R. Schwank, M. R. Shaneyfelt, D. M. Fleetwood, J. A. Felix, P. E. Dodd, P. Paillet, and V. Ferlet-Cavrois, “Radiation effects in MOS oxides,” *IEEE Transactions on Nuclear Science*, vol. 55, no. 4, pp. 1833–1853, 2008.

[158] D. M. Fleetwood, “Total ionizing dose effects in MOS and low-dose-rate-sensitive linear-bipolar devices,” 2013.

[159] D. J. DiMaria, E. Cartier, and D. Arnold, “Impact ionization, trap creation, degradation, and breakdown in silicon dioxide films on silicon,” *Journal of Applied Physics*, vol. 73, no. 7, pp. 3367–3384, 1993.

[160] C. H. Seager, R. a. Anderson, and J. K. G. Panitz, “The diffusion of hydrogen in silicon and mechanisms for unintentional hydrogenation during ion beam processing,” *Journal of Materials Research*, vol. 2, no. 01, pp. 96–106, 1987.

[161] L.-A. Ragnarsson and P. Lundgren, “Electrical characterization of P_b centers in (100)Si-SiO2 structures: The influence of surface potential on passivation during post metallization anneal,” *Journal of Applied Physics*, vol. 88, no. 2, p. 938, 2000.

[162] P. M. Lenahan and P. Dressendorfer, “Effect of bias on radiation-induced paramagnetic defects at the silicon-silicon dioxide interface,” *Applied Physics Letters*, vol. 41, no. 6, pp. 542–544, 1982.

[163] N. M. Johnson, D. K. Biegelsen, M. D. Moyer, S. T. Chang, E. H. Poindexter, and P. J. Caplan, “Characteristic electronic defects at the Si-SiO2 interface,” *Applied Physics Letters*, vol. 43, no. 1983, pp. 563–565, 1983.

[164] C. T. Sah, J. Y. C. Sun, and J. J. T. Tzou, “Deactivation of the boron acceptor in silicon by hydrogen,” *Applied Physics Letters*, vol. 43, no. 2, pp. 204–206, 1983.

[165] C. T. Sah, J. Y. C. Sun, J. J. Tzou, and S. C. S. Pan, “Deactivation of group III acceptors in silicon during keV electron irradiation,” *Applied Physics Letters*, vol. 43, no. 10, pp. 962–964, 1983.

[166] N. M. Johnson and S. K. Hahn, “Hydrogen passivation of the oxygen-related thermal-donor defect in silicon,” *Applied Physics Letters*, vol. 48, no. 11, pp. 709–711, 1986.

[167] N. Fukata, S. Sato, H. Morihiro, K. Murakami, K. Ishioka, M. Kitajima, and S. Hishita, “Dopant dependence on passivation and reactivation of carrier after hydrogenation,” *Journal of Applied Physics*, vol. 101, no. 4, pp. 2005–2008, 2007.

[168] C. Y. P. Chao, M. S. C. Luo, S. C. S. Pan, and C. T. Sah, “Hydrogenation of boron acceptor in silicon during electron injection by Fowler-Nordheim tunneling,” *Applied Physics Letters*, vol. 50, no. 4, pp. 180–181, 1987.

[169] K. J. Chang and D. J. Chadi, “Theory of hydrogen passivation of shallow-level dopants in crystalline silicon,” *Physical Review Letters*, vol. 60, no. 14, pp. 1422–1425, 1988.

[170] N. M. Johnson, “Mechanism for hydrogen compensation of shallow-acceptor impurities in single-crystal silicon,” *Physical Review B*, vol. 31, no. 8, pp. 5525–5528, 1985.

[171] N. M. Johnson, C. Herring, and D. J. Chadi, “Interstitial Hydrogen and Neutralization of Shallow-Donor Impurities in Single-Crystal Silicon,” *Physical Review Letters*, vol. 56, no. 7, pp. 769–772, 1986.

[172] R. Rizk, P. D. Mierry, D. Ballutaud, M. Aucouturier, and D. Mathiot, "Hydrogen diffusion and passivation processes in p-and n-type crystalline silicon," *Physical review B*, vol. 44, no. 12, pp. 6141–6151, 1991.

[173] J. I. Pankove, R. O. Wance, and J. E. Berkeyheiser, "Neutralization of acceptors in silicon by atomic hydrogen," *Applied Physics Letters*, vol. 45, no. 10, pp. 1100–1102, 1984.

[174] K. Akarvardar, R. D. Schrimpf, D. M. Fleetwood, S. Cristoloveanu, P. Gentil, and B. J. Blalock, "Evidence of Radiation-Induced Dopant Neutralization in Partially-Depleted SOI NMOSFETs," *IEEE Transactions on Nuclear Science*, vol. 54, pp. 1920–1924, dec 2007.

[175] E. da Silva Jr., E. de Vasconcelos, and V. Freire, "Time evolution of SiO 2 / Si interface defects and dopant passivation in MOS capacitors," *Microelectronic Engineering*, vol. 51-52, pp. 567–574, 2000.

[176] S. T. Pantelides, "Effect of hydrogen on shallow dopants in crystalline silicon," *Applied Physics Letters*, vol. 50, no. 15, pp. 995–997, 1987.

[177] C.-C. Wei and T.-P. Ma, "Reduction of apparent dopant concentration in the surface space charge layer of oxidized silicon by ionizing radiation," *Applied Physics Letters*, vol. 45, no. 8, p. 900, 1984.

[178] A. Camplani, S. Shojaii, H. Shrimali, A. Stabile, and V. Liberali, "CMOS IC radiation hardening by design," *Facta universitatis - series: Electronics and Energetics*, vol. 27, no. 2, pp. 251–258, 2014.

[179] R. Trivedi and U. S. Mehta, "A survey of radiation hardening by design (rhbd) techniques for electronic systems for space application," *International Journal of Electronics and Communication Engineering & Technology (IJECET)*, vol. 7, no. 1, pp. 75–86, 2016.

[180] "imec." http://www.europractice-ic.com/SiPhotonics_technology_imec_ISIPP25G.php.

[181] "ePIXfab." http://www.epixfab.eu/.

[182] S. Seif El Nasr-Storey, F. Boeuf, C. Baudot, S. Detraz, J. M. Fedeli, D. Marris-Morini, L. Olantera, G. Pezzullo, C. Sigaud, C. Soos, J. Troska, F. Vasey, L. Vivien, M. Zeiler, and M. Ziebell, "Modeling TID Effects in Mach-Zehnder Interferometer Silicon Modulator for HL-LHC data Transmission Applications," *IEEE Transactions on Nuclear Science*, vol. 62, no. 6, pp. 2971 – 2978, 2015.

[183] Synopsys, "Sentaurus Device." https://www.synopsys.com/silicon/tcad/device-simulation/sentaurus-device.html.

[184] H. Xu, X. Xiao, X. Li, Y. Hu, Z. Li, T. Chu, Y. Yu, and J. Yu, "High speed silicon Mach-Zehnder modulator based on interleaved PN junctions," *Optics Express*, vol. 20, no. 14, pp. 15093–15099, 2012.

[185] L. Alloatti, D. Cheian, and R. J. Ram, "High-speed modulator with interleaved junctions in zero-change CMOS photonics," *Applied Physics A: Materials Science & Processing*, vol. 131101, pp. 1–7, 2016.

[186] S. M. Sze and K. K. Ng, *Physics of Semiconductor Devices.* Wiley, 3rd editio ed., 2006.

[187] J. F. Ziegler, "SRIM - The Stopping and Range of Ions in Matter." http://www.srim.org/.

[188] Brigham Young University, "Ion Implantation: Projected Range & Straggle Calculator." http://www.cleanroom.byu.edu/rangestraggle.phtml.

[189] PhoeniX, "OptoDesigner 5." http://www.phoenixbv.com/index.php.

[190] P. Dong, L. Chen, and Y.-k. Chen, "High-speed low-voltage single-drive push-pull silicon Mach-Zehnder modulators," *Optics Express*, vol. 20, no. 6, pp. 6163–6169, 2012.

[191] D. Marris-Morini, C. Baudot, J.-M. Fédéli, G. Rasigade, N. Vulliet, A. Souhaité, M. Ziebell, P. Rivallin, S. Olivier, P. Crozat, X. L. Roux, D. Bouville, S. Menezo, F. Bœuf, and L. Vivien, "Low loss 40 Gbit/s silicon modulator based on interleaved junctions and fabricated on 300 mm SOI wafers," *Optics Express*, vol. 21, no. 19, pp. 22471–22475, 2013.

[192] D. Marris-Morini, X. Le Roux, L. Vivien, E. Cassan, D. Pascal, M. Halbwax, S. Maine, S. Laval, J.-M. Fédéli, and J. F. Damlencourt, "Optical modulation by carrier depletion in a silicon PIN diode.," *Optics Express*, vol. 14, pp. 10838–10843, oct 2006.

[193] B. Snyder and P. O'Brien, "Packaging process for grating-coupled silicon photonic waveguides using angle-polished fibers," *IEEE Transactions on Components, Packaging and Manufacturing Technology*, vol. 3, no. 6, pp. 954–959, 2013.

[194] L. Caroll and P. O'Brien, "Design Rules for Silicon Photonic Packaging at Tyndall Institute." http://www.europractice-ic.com/docs/Design_Rules_for_Silicon_photonic_packaging_at_Tyndall_Institute_Jan_2015.pdf, 2015.

[195] K. Jinguji, M. Horiguchi, and T. Manabe, "Spectral loss measurement system for IR optical fibers," *Applied Optics*, vol. 21, no. 4, p. 571/572, 1982.

[196] B. W. Snyder and P. a. O'Brien, "Developments in packaging and integration for silicon photonics," *Proc. SPIE 8614, Reliability, Packaging, Testing, and Characterization of MOEMS/MEMS and Nanodevices XII*, vol. 8614, no. 0, p. 86140D, 2013.

[197] N. Pavarelli, J. S. Lee, and P. A. O'Brien, "Packaging challenges for integrated silicon photonic circuits," in *Silicon Photonics and Photonic Integrated Circuits IV*, 2014.

[198] D. K. Schroder, *Semiconductor Material and Device Characterization*. Wiley, 2006.

[199] PV Lighthouse, "Resistivity calculator." https://www.pvlighthouse.com.au/resistivity.

[200] Cascade Microtech, "LWP Multi-Configurable Optical Probe for Photonic Device Characterization." https://www.cascademicrotech.com/files/LWP_SS.pdf.

[201] CERN-PH-ESE, "The CERN-ESE-ME X-ray irradiation system for TID studies in microelectronics." http://proj-xraymic.web.cern.ch/proj-xraymic/Xraycalibration_files/CalibrationJune2013_noPassword.pdf, 2013.

[202] J. Osborn, R. Lacoe, D. Mayer, and G. Yabiku, "Total dose hardness of three commercial CMOS microelectronics foundries," in *Radiation Effects on Components and Systems (RADECS)*, pp. 265–270, IEEE, 1997.

[203] Tyndall National Institue, "Photonics Packaging." https://www.tyndall.ie/packaging.

[204] D. J. DiMaria and J. W. Stasiak, "Trap creation in silicon dioxide produced by hot electrons," *Journal of Applied Physics*, vol. 65, no. 6, pp. 2342–2356, 1989.

[205] T. Oldham and F. B. McLean, "Total Ionizing Dose Effects in MOS Oxides and Devices," 2003.

[206] H. J. Barnaby, B. Vermeire, and M. J. Campola, "Improved Model for Increased Surface Recombination Current in Irradiated Bipolar Junction Transistors," *Nuclear Science, IEEE Transactions on*, vol. 62, no. 4, pp. 1658–1664, 2015.

[207] R. C. Hughes, "Hole mobility and transport in thin SiO2 films," *Applied Physics Letters*, vol. 26, pp. 436–438, apr 1975.

[208] S. Witczak, R. Schrimpf, D. Fleetwood, K. Galloway, R. Lacoe, D. Mayer, J. Puhl, R. Pease, and J. Suehle, "Hardness assurance testing of bipolar junction transistors at elevated irradiation temperatures," *IEEE Transactions on Nuclear Science*, vol. 44, no. 6, pp. 1989–2000, 1997.

[209] S. C. Witczak, R. C. Lacoe, M. R. Shaneyfelt, D. C. Mayer, J. R. Schwank, and P. S. Winokur, "Implications of radiation-induced dopant deactivation for npn bipolar junction transistors," *IEEE Transactions on Nuclear Science*, vol. 47, no. 6 III, pp. 2281–2288, 2000.

[210] J. Troska, S. S. E. Nasr-Storey, S. Dêtraz, L. Olanterä, P. Stejskal, C. Sigaud, C. Soós, and F. Vasey, "Laser and photodiode environmental evaluation for the Versatile Link project," *Journal of Instrumentation*, vol. 8, feb 2013.

[211] R. J. Graves, C. R. Cirba, R. D. Schrimpf, S. Member, R. J. Milanowski, A. Michez, D. M. Fleetwood, S. C. Witczak, and F. Saigne, "Modeling Low-Dose-Rate Effects in Irradiated Bipolar-Base Oxides," *IEEE Transactions on Nuclear Science*, vol. 45, no. 6, pp. 2352–2360, 1998.

[212] A. Komarov, G. Zayats, F. Komarov, S. Miskiewicz, and V. Michailov, "Simulation of Radiation Effects in SiO2/Si Structures," *Proceedings of the International Conference Nanomaterials: Applications and Properties*, vol. 3, no. 1, 2014.

[213] D. Patel, V. Veerasubramanian, S. Ghosh, A. Samani, Q. Zhong, and D. V. Plant, "High-speed compact silicon photonic Michelson interferometric modulator.," *Optics express*, vol. 22, no. 22, pp. 26788–802, 2014.

[214] ANSYS, "Electronics Desktop: Electromagnetic Analysis." http://www.ansys.com/products/electronics/ansys-electronics-desktop.

[215] T. H. Lee, *The Design of CMOS Radio-Frequency Integrated Circuits.* Cambridge University Press, 2nd editio ed., 2004.

[216] S. Caniggia and F. Maradei, *Signal Integrity and Radiated Emission of High-Speed Digital Systems.* Wiley Online Library, 2008.

[217] G.-R. Zhou, M. W. Geis, S. J. Spector, F. Gan, M. E. Grein, R. T. Schulein, J. S. Orcutt, J. U. Yoon, D. M. Lennon, T. M. Lyszczarz, E. P. Ippen, and F. X. Käertner, "Effect of carrier lifetime on forward-biased silicon Mach-Zehnder modulators," *Optics Express*, vol. 16, no. 8, p. 5218, 2008.

[218] A. C. Turner-Foster, M. a. Foster, J. S. Levy, C. B. Poitras, R. Salem, A. L. Gaeta, and M. Lipson, "Ultra-short free-carrier lifetime in low-loss silicon nanowaveguides," *Optics Express*, vol. 18, no. 4, p. 3582, 2010.

[219] R. Häcker and A. Hangleiter, "Intrinsic upper limits of the carrier lifetime in silicon," *Journal of Applied Physics*, vol. 75, pp. 7570–7572, jun 1994.

[220] A. Noda, "Optical modulation device having bias reset means," 1996.

[221] Y. Nagakubo, S. Ibukuro, A. Hayashi, and T. Tsuda, "Light transmitter having an automatic bias control circuit," 1999.

[222] G. Roelkens, D. Van Thourhout, and R. Baets, "High efficiency Silicon-on-Insulator grating coupler based on a poly-Silicon overlay," *Optics Express*, vol. 14, no. 24, p. 11622, 2006.

[223] X. Chen, C. Li, C. K. Y. Fung, S. M. G. Lo, and H. K. Tsang, "Apodized Waveguide Grating Couplers for Efficient Coupling to Optical Fibers," *IEEE Photonics Technology Letters*, vol. 22, pp. 1156–1158, aug 2010.

[224] Zhen Sheng, Zhiqi Wang, Chao Qiu, Le Li, A. Pang, Aimin Wu, Xi Wang, Shichang Zou, and Fuwan Gan, "A Compact and Low-Loss MMI Coupler Fabricated With CMOS Technology," *IEEE Photonics Journal*, vol. 4, pp. 2272–2277, dec 2012.

[225] P. Dumon, W. Bogaerts, V. Wiaux, J. Wouters, S. Beckx, J. Van Campenhout, D. Taillaert, B. Luyssaert, P. Bienstman, D. Van Thourhout, and R. Baets, "Low-Loss SOI Photonic Wires and Ring Resonators Fabricated With Deep UV Lithography," *IEEE Photonics Technology Letters*, vol. 16, pp. 1328–1330, may 2004.

[226] S. Liu, D. J. Thomson, K. Li, P. Wilson, and G. T. Reed, "N-over-N cascode push-pull modulator driver in 130 nm CMOS enabling 20 Gbit/s optical interconnection with Mach-Zehnder modulator," *Electronics Letters*, vol. 51, no. 23, pp. 1900–1902, 2015.

[227] N. C. Harris, Y. Ma, J. Mower, T. Baehr-Jones, D. Englund, M. Hochberg, and C. Galland, "Efficient, compact and low loss thermo-optic phase shifter in silicon," *Optics Express*, vol. 22, no. 9, pp. 83–85, 2014.

[228] P. Amberg, E. Chang, F. Liu, J. Lexau, X. Zheng, G. Li, I. Shubin, J. E. Cunningham, A. V. Krishnamoorthy, and R. Ho, "A sub-400 fJ/bit thermal tuner for optical resonant ring modulators in 40 nm CMOS," in *2012 IEEE Asian Solid State Circuits Conference (A-SSCC)*, pp. 29–32, IEEE, dec 2012.

[229] M. Cignoli, G. Minoia, M. Repossi, D. Baldi, A. Ghilioni, E. Temporiti, and F. Svelto, "A 1310nm 3D-integrated silicon photonics Mach-Zehnder-based transmitter with 275mW multistage CMOS driver achieving 6dB extinction ratio at 25Gb/s," in *Digest of Technical Papers - IEEE International Solid-State Circuits Conference*, vol. 58, pp. 416–417, 2015.

[230] S. Zhou, H. Wu, K. Sadeghipour, C. Scarcella, C. Eason, M. Rensing, M. Power, C. Antony, P. O'Brien, P. Townsend, and P. Ossieur, "Optimization of PAM-4 transmitters based on lumped silicon photonic MZMs for high-speed short-reach optical links," *Optics express*, vol. 25, no. 4, pp. 4312–4325, 2017.

[231] "Future Circular Collider Study." https://fcc.web.cern.ch/Pages/default.aspx.

[232] "Compact Linear Collider." http://clic-study.web.cern.ch/.

Acknowledgement

I would like to thank everybody who directly supported or otherwise helped me during the research for this thesis. These are first and foremost all current and past members of the (EP-ESE-BE) Opto-Team at CERN: Andrea Kraxner, Carmelo Scarcella, Christophe Sigaud, Csaba Soos, Francois Vasey, Giuseppe Pezzullo, Jan Troska, Lauri Olantera, Sarah Seif El Nasr-Storey and Stephane Detraz. My special gratitude goes to Jan and Francois for being excellent supervisors. I owe many of my achievements while carrying out this research to your guidance and encouragement over the years and especially to your support during my time abroad. I am also indebted to Liam Barry for giving me the opportunity to pursue my PhD studies outside his group at DCU. Your supervision and constant feedback were always very valuable and helped me in completing this thesis. I am grateful to Bob Herrick, Haisheng Rong, Juthika Basak and Michael Geva for hosting and advising me during my time at Intel. Last but not least I would like to thank my family and friends. I would not have been able to do this without you.